

**Assessing Molecular Biomarkers in Living Mice Using
Fluorescence Microendoscopy and Spectroscopy**

by

Sakib F. Elahi

A dissertation submitted in partial fulfillment
of the requirements for the degree of
Doctor of Philosophy
(Biomedical Engineering)
in The University of Michigan
2014

Doctoral Committee:

Professor Mary-Ann Mycek, Chair
Associate Professor Xudong Fan
Professor Stephen E. Feinberg
Professor Emerita Cynthia L. Marcelo

Dedication

This dissertation is dedicated to my loving parents,
Rita and Yousuf Elahi,
who have always been dedicated to me.

Acknowledgements

I am forever grateful to my wonderful advisor, Dr. Mary-Ann Mycek. She gave me the opportunity to join her lab to further my graduate studies. She mentored me to become an independent scientist by giving me ownership of my projects and holding high expectations. She searched for and encouraged me to pursue opportunities that would benefit my development as a scientist and an educator. She made my best interests her own priority for mentorship. Mary-Ann demonstrated to me what it means to be a great professor, setting an example that I will strive to follow throughout my career.

I also thank my three committee members: Dr. Stephen Feinberg, our collaborator in Oral Surgery, who provided valuable advice from both a clinical and a research perspective; Dr. Cynthia Marcelo, who could teach me more about keratinocyte biology in a 30 minute conversation than I could learn in a full day of literature review; and Dr. Xudong (Sherman) Fan, whom I had the pleasure of assisting to teach Bioinstrumentation, which was greatly influential in my decision to pursue a teaching-focused academic career.

Dr. Gary Luker and Dr. Kathy Luker were great research mentors who had the patience to teach molecular biology to a mechanical engineer. I thank Dr. Albert Shih for encouraging me to attend graduate school and for believing in me. I also thank my first advisor, Dr. Thomas Wang, for taking me in his lab and surrounding me with incredible resources to do cutting-edge research.

I want to specially thank Dr. Sharon Miller, who was a post-doc in the Wang Lab and is now a professor at Aurora University, for being the greatest influence in my development as a scientist. Her example of creative thinking, strong work ethic, professionalism, and passion for science and education is one that I will always strive to follow but probably never fully realize.

I was lucky to have great colleagues in both of my labs. In the Wang Lab: Dr. Zhongyao Liu, Dr. Bishnu Joshi, Dr. Zhen Qiu, Dr. Supang Khondee, and Chris Komarck. In the Mycek Lab: Dr. Robert Wilson, Dr. Bill Lloyd, Leng-Chun Chen, and Seung Yup (Paul) Lee. Other very helpful collaborators were: Dr. Hyungjin Myra Kim, Dr. Shiuhyang Kuo, Dr. Robert Kennedy, Ying Zhou, and Toby Donajkowski.

Teaching was a huge part of my graduate education. In addition to Dr. Fan, I thank Dr. Susan Montgomery, Dr. Dennis Claflin, Dr. Aileen Huang-Saad, and Dr. Rachael Schmedlen for providing excellent mentorship to develop my teaching skills and to help me seek teaching careers. Working with bright students was one of the most gratifying experiences that I had in graduate school.

The most important thanks are for my loved ones:

Amma & Abba – You are my strongest supporters. You made me a man. You have allowed me to pursue my own life path, while also giving me wise advice. You trust in me and you trust in God. I couldn't have achieved anything without your love.

Kelley – You are my love, my best friend, and my biggest fan. Thank you for believing in me, even when I didn't believe in myself. Thank you for sharing in my successes and my failures, supporting me through the very difficult times, and for giving me space and grace when I needed it. Thank you for always challenging me to be a better man.

Eshrak & Tasnia – Mostly, thanks for staying out of my way while I pursued this crazy endeavor. Just kidding. I love you guys and I know you love me too. Thanks for always being there.

Twelve years at the University is a very, very long time.

Funding Acknowledgements

Chapter 1

This work was funded by NIH grants U54 CA136429, P50 CA 93990, and R01 CA142750.

Chapter 2

Research was supported by NIH grants R01 CA136553, R01 CA136829, R01 CA 142750, P50 CA 93990, and U54 CA 136429. We thank Gordon Mills, MD Anderson Cancer Center, for providing the HeyA8 ovarian cancer cells.

Chapter 3

Research was supported in part by NIH grants P30 DK034993, P50 CA93990, and R01 CA142750. The bench top confocal microscopy work was performed in the Microscopy & Image Analysis Laboratory (MIL) at the University of Michigan.

Chapters 4 and 5

Research was supported in part by an NIH grant (R01-DE-019431, to Mary-Ann Mycek and Stephen E. Feinberg) and the U.S. Department of Education (GAANN Fellowship to Sakib F. Elahi).

Table of Contents

Dedication	ii
Acknowledgements	iii
Funding Acknowledgements	v
List of Figures	x
Abstract	xv
Chapter 1. Introduction	1
1.1 Importance of Using Small Animal Models for Biomedical Research	2
1.2 Need for Intravital Assessment of Molecular Biomarkers	3
1.2.1 Intravital Imaging of Tissue Epithelium for Colon Cancer	3
1.2.2 Intravital Spectroscopy of Engineered Tissues	4
1.3 Overview of Intravital Fluorescence Imaging and Spectroscopy Techniques	5
1.3.1 Challenge for Miniaturizing Intravital Microscopes	5
1.3.2 High Resolution Fluorescence Microendoscopy	5
1.3.3 Confocal Endomicroscopy	6
1.3.4 Fiber-Optic Probe-Based Fluorescence Lifetime Spectroscopy	6
1.4 Fluorescent Molecular Biomarkers	7
1.4.1 Genetically Encoded Fluorescent Proteins for Basic Biomedical Research	8
1.4.2 Endogenous Fluorophores for Label-Free Optical Assessment	8
1.4.3 Exogenous Molecular Probes for Targeting of Cancer Biomarkers	9
1.5 Dissertation Objectives	12
1.6 Dissertation Overview	15
References	16
Chapter 2. Longitudinal Imaging of Mice using a LED-Based Microendoscope	20
2.1 Introduction	20
2.2 Methods	21

2.2.1	System design of LED-based fluorescence microendoscope	21
2.2.2	Optical model to optimize coupling efficiency of LED source into fiber bundle	22
2.2.3	Transduction and <i>in vitro</i> imaging of GFP-expressing ovarian cancer cells	23
2.2.4	Longitudinal <i>in vivo</i> imaging of tumor xenografts in mice	24
2.3	Results	25
2.3.1	Microendoscope characterization	25
2.3.2	Optical model prediction of fiber bundle output light intensity	25
2.3.3	<i>In vitro</i> validation of fluorescence imaging using microendoscope	27
2.3.4	Longitudinal <i>in vivo</i> imaging of tumor xenografts in mice	28
2.4	Discussion	29
	References	31
	Chapter 3. Targeted Imaging of Colorectal Dysplasia in Living Mice using Fluorescence Microendoscopy	34
3.1	Introduction	34
3.2	Methods	35
3.2.1	Design of fluorescence microendoscope for small animal colonoscopy	35
3.2.2	Animal models	36
3.2.3	<i>In vivo</i> microendoscopy	37
3.2.4	<i>Ex vivo</i> confocal microscopy	38
3.2.5	Data analysis	38
3.3	Results	39
3.3.1	System design	39
3.3.2	<i>In vivo</i> microendoscopy	39
3.3.3	Comparison of <i>in vivo</i> microendoscopy to <i>ex vivo</i> confocal microscopy	41
3.4	Discussion	41
	References	42
	Chapter 4. Noninvasive Optical Assessment of Implanted Engineered Tissues Correlates with Pre-Implantation Cytokine Secretion	44
4.1	Introduction	44
4.2	Methods	46

4.2.1	Manufacturing of EVPOME Human Keratinocyte-Based Tissue Engineered Constructs	46
4.2.2	Pre-Implantation Assessment of Construct Health by Biochemical Assay and Histology	47
4.2.3	Experimental Study Design	48
4.2.4	Construct Implantation Protocol	51
4.2.5	Fluorescence Lifetime Spectroscopy Instrumentation	51
4.2.6	Fluorescence Lifetime Spectroscopy Measurement Protocol	53
4.2.7	Fluorescence Lifetime Spectroscopy Data Analysis	53
4.2.8	Statistical Analysis	56
4.3	Results	56
4.3.1	Characterization of <i>In Vivo</i> Fluorescence Lifetime Spectroscopy Measurements	56
4.3.2	Correlation between <i>In Vivo</i> Optical Parameters and <i>In Vitro</i> Cytokine Secretion	58
4.4	Discussion	59
	References	62
	Chapter 5. Design and Construction of an Intravital Depth-Resolved Fluorescence Lifetime Spectrometer	67
5.1	Introduction	67
5.2	Methods	68
5.2.1	Overall Design Concept	68
5.2.2	Galilean Beam Expander for Single Mode Fiber Coupling	70
5.2.3	Theoretical Calculation of Axial Resolution	72
5.2.4	Theoretical Temporal Resolution and Sensitivity	75
5.2.5	Filters and Dichroic Mirrors	75
5.2.6	Automated Motorized Control and Data Acquisition	76
5.3	Results	77
5.3.1	Single Mode Fiber Coupling	77
5.3.2	Construction of portable CFLS system	78
5.3.3	Reflectance Axial Resolution Testing	79
5.4	Discussion	79

References	81
Chapter 6. Conclusions and Future Directions	83
6.1 Major contributions of this dissertation	83
6.2 Future Directions	86
6.2.1 <i>In Vivo</i> Monitoring of Ovarian Cancer Cell Apoptosis Using a Dual-Color Flexible Fiber Microendoscope	86
6.2.2 Confocal Fiber Bundle Based Microendoscopy	86
6.2.3 Phantom for Simulating Epithelial Tissue Fluorescence	87
6.2.4 Characterization of Depth-Resolved Fluorescence Lifetime Spectrometer	87

List of Figures

- Fig. 1.1.** Carcinoma of the colon arises from a transformation of normal epithelium to dysplasia. Subtle molecular changes develop first in the crypts prior to morphological changes in the tissue. An intravital microscope placed on the luminal surface of the tissue can be used to study the molecular progression of this disease longitudinally in small animal models. 3
- Fig. 1.2.** Exogenous molecular probe platforms. Strengths and weaknesses of various probe platforms being developed for targeted imaging are presented [64]. 11
- Fig. 1.3.** Overview of dissertation projects. Chapters 2 and 3 use fluorescence imaging techniques for applications in cancer. Chapters 4 and 5 use fluorescence lifetime spectroscopy techniques for assessing tissue engineered construct health. 14
- Fig. 2.1.** LED-based microendoscope design schematic. Excitation from LED at 470 nm is collimated by an asphere, reflected by a dichroic beamsplitter, and focused into a 680 μm (O.D.) coherent fiber bundle. Fluorescence is transmitted to the CCD. The distal end of the fiber (inset) is placed into contact with the tissue. 22
- Fig. 2.2.** Longitudinal imaging approach. The distal tip of the microendoscope is introduced with an 18G needle into the peritoneum through a catheter to collect fluorescence (green) from implanted HeyA8 ovarian tumor. The mice survive without need for closure of the wound. 24
- Fig. 2.3.** Simulated fiber bundle power throughput. Dependence of the output intensity on L1' and L2 from our model is shown. Maximum power of 0.9 mW can be transmitted with L2 = 40 mm, but size constraints require L2 = 80 mm for maximum simulated power of 0.76 mW. 26
- Fig. 2.4.** *In vitro* imaging of cells. Fluorescence images of HeyA8-GFP cells in culture collected with an (a) epifluorescence microscope and the (b) microendoscope reveal similar GFP fluorescence patterns constitutively expressed by the cells. 27

Fig. 2.5. *In vivo* imaging after implantation of HeyA8-GFP cells. a) Single cells (week 1). b) Small cluster of cells (week 2). c) Bulk tumor mass (week 3). d) Neovasculature detected as branching, non-fluorescent structures within a GFP-positive tumor (week 4). 28

Fig. 3.1. Small animal fluorescence microendoscope design schematic. Excitation from the laser diode at 473 nm is collimated by an asphere (L1), reflected by a dichroic beamsplitter, and focused into a 680 μm (O.D.) coherent fiber bundle. Fluorescence is transmitted to the CCD. The bundle is sufficiently small in dimension to pass through the instrument channel of a small animal endoscope (inset). 36

Fig. 3.2. *In vivo* microendoscopy images of murine colonic tissue. QPIHPNNM applied to the surface of a) an adenoma (Media 1) and b) normal-appearing adjacent mucosa. GGGAGGGA (control peptide) applied to the surface of c) an adenoma and d) normal-appearing adjacent mucosa. e) QPIHPNNM applied to normal colonic mucosa in *Cre(-)* mice. f) Autofluorescence from adenoma in *Cre(+)* mice. g) QPIHPNNM applied to hyperplastic mucosa of *Kras* mouse. h) Autofluorescence signal from *Kras* mouse. Scale bar = 100 μm . 40

Fig. 3.3. Quantification of average fluorescence intensities. (a) Boxplot of T/B of peptides from adenomas to adjacent normal mucosa. T/B of QPIHPNNM is significantly higher than that of GGGAGGGA. Lower, middle, and top lines of boxes indicate lower quartile, median, and upper quartile, respectively. Whiskers indicate minima and maxima, and crosshairs indicate means. (b) Mean fluorescence intensity of QPIHPNNM, after autofluorescence subtraction. Fluorescence signal from dysplasia is at least five-fold greater than from all other tissues. 40

Fig. 3.4. Confocal microscopy images of excised colonic adenomas. (a) QPIHPNNM shows binding to single epithelial cells (arrow). (b) Minimal binding was revealed on using the GGGAGGGA peptide. (c) Histology confirms dysplastic crypts in adenoma biopsy specimens. Scale bar = 20 μm . 41

Fig. 4.1. Study design for each patient. Cells from one patient were seeded on AlloDerm® (Day 0) in two cohorts, one to be implanted in mice for 1 week, the other for 3 weeks. The incubation temperature of stressed constructs (red) was increased to 43°C, while control constructs (blue) were maintained at 37°C (Day 9-10). At day 11 for each construct, three aliquots of spent culture medium were collected for ELISA, one-fifth of the construct was

cut for histology, and the remainder was implanted into a SCID mouse. Constructs were optically assessed by fluorescence lifetime spectroscopy (FLS) for both 1-week and 3-week post-implantation cohorts (Day 18 and 32). After optical assessment, the mice were sacrificed, and the construct processed for histology. Note that “Day 0” for 1-week and 3-week cohorts was staggered so that FLS measurements could be taken on the same day. 49

Fig. 4.2. Representative EVPOME histology. Control pre-implantation constructs developed three distinct layers: a top keratin layer (K), a middle living cell layer (LC), and a bottom dermal equivalent layer (DE). Stressed constructs did not develop a healthy cell layer pre-implantation. One week after implantation, cell layers in control constructs were thicker and more organized than those of stressed constructs. However, cell layers of both control and stressed groups were comparably healthy 3 weeks after implantation, consisting re-epithelialized cell layers and neovasculature (arrowheads). All scale bars are 50 μm . 50

Fig. 4.3. Schematic of fluorescence lifetime spectroscopy (FLS) system components. The distal end of the fiber probe is positioned at varying stand-off distances from the top of the tissue sample. The system acquires data in less than one second per measurement. The handheld probe is sufficiently small to be positioned at multiple sites on each construct. The angled probe design aids in localizing optical interrogation to the top living cell layer of the construct, and reduces collection of reflected excitation light. ND: neutral density filter. PD: photodiode. L1, L2, L3: lenses. LP: long pass filter. BP: band pass filter. APD: avalanche photodiode. 52

Fig. 4.4. Fluorescence lifetime spectroscopy (FLS) data analysis. A) Representative time-resolved fluorescence decays acquired from one mouse, at one stand-off. Fluorescence data acquired from the construct (On Site, diamonds) were fit to a bi-exponential decay (Simulation Fit, solid line), for extraction of fluorescence lifetime parameters τ_1 , τ_2 , A_1 , and A_2 . The residual difference between the data and the simulation fit is no more than 2% (gray line). Signals acquired from muscle tissue adjacent to the construct (Off Site, dashed line) and neighboring skin (dotted line) are significantly lower than signal from the construct. B) Box plots of peak fluorescence intensity, categorized by stand-off distance of probe from tissue sample. Peak fluorescence intensity from the constructs decreased consistently as the stand-off distance increased. C) However, the extracted fluorescence

lifetime parameter A_1/A_2 was consistent for all stand-off distances. Therefore, the fluorescence lifetime parameters from all stand-offs per construct may be combined for data analysis. Data for box plots is for week 1 control measurements (N = 9, 12, 12, 8, 7 for stand-offs 0.0 – 2.0 mm, respectively). 57

Fig. 4.5. Noninvasive optical sensing of implanted constructs. The fluorescence lifetime parameter A_1/A_2 varied across the 1-week implantation study population. This ratio correlated negatively with pre-implantation protein concentration levels for all three constitutively secreted proteins (linear mixed effects model, $p < 0.05$ for all three). Each data point represents the average value per construct, with standard error. 59

Fig. 5.1. Schematic of confocal fluorescence lifetime spectroscopy (CFLS) system components. Excitation is coupled to a single mode fiber for coherent delivery to the sample arm of the system. Emitted fluorescence signal from the sample is coupled to a multimode fiber, which acts as a confocal pinhole, for delivery to the detection arm of the system. FAD and NADH signals are separated and detected on two channels by photomultiplier tubes and a digitizing oscilloscope. L1-L7: Lenses. DM1 and DM2: Dichroic beamsplitters. LP1: Long pass filter. BP1 and BP2: Band pass filters. 68

Fig. 5.2. Coupling of laser excitation source to single mode fiber. A Galilean beam expander constructed by lenses L1 and L2 magnifies the laser beam, which has radius y_1 , to fill the back aperture y_3 of the focusing objective L3. The focal length f_3 of the objective lens must be determined to match the Gaussian mode of the fiber. 71

Fig. 5.3. Representative lateral point spread function at varying axial depths. This simulation of the spatial intensity of the detected fluorescence for varying pinhole diameters was used to optimize the numerical aperture and magnification of the optical system. 73

Fig. 5.4. Relationship of axial point spread function to pinhole radius. a) When magnification is fixed at 3, the axial resolution improves with increasing NA. Beyond an NA of 0.4, the axial resolution reaches a plateau even for very large pinhole radii. b) When NA is fixed at 0.4, the axial resolution improved with increasing magnification. 74

Fig. 5.5. Filtering design to preferentially detect NADH and FAD signal in CFLS. Solid lines show normalized emission spectra of NADH, FAD, and collagen. Dashed lines show transmission spectra of dichroic mirrors and band-pass filters. DM2 separates FAD signal

from NADH and collagen signal. BP1 further rejects leaked collagen and NADH signal transmitted towards Channel 1 to preferentially detect FAD. BP2 selects the spectral region dominated by NADH signal over collagen. 76

Fig. 5.6. Constructed Galilean beam expander for coupling laser excitation to single mode fiber. The maximum measured coupling efficiency was 98%. However, at this high energy density the fiber would become damaged. A neutral density filter of optical density at least 0.3 is necessary to prevent thermal damage of the fiber. 77

Fig. 5.7. Portable CFLS system. a) The whole system is mounted on a portable cart for clinical use. The lower shelf contains the CPU, oscilloscope, and motor control driver. The middle shelf contains the illumination optics, detection optics and electronics. The top shelf contains the sample arm and the animal stage for intravital assessment. b) The detection electronics are secured to the middle shelf. c) The sample arm is positioned over a titling stage that can hold the animal. The yellow fiber is the illumination single mode fiber. The orange fiber is the emission multimode fiber. 78

Fig. 5.8. Axial resolution knife edge experiment results. The reflected laser pulse intensity measured from a mirror translated axially across the focal volume has a FWHM of 78 μm , serving as an estimate of the axial resolution of the CFLS. 79

Abstract

Assessment of molecular biomarkers expressed in cells and tissues can inform scientists and clinicians of physiological and disease processes. Optical techniques can quantitatively and noninvasively assess molecular biomarkers in living tissues. This dramatically improves our ability to study detailed behavior of disease, perform earlier detection of disease, and assess functional cellular information. However, small animals, which play an important role in the study of molecular biomarkers, pose a challenge for intravital optical assessment. In this dissertation, we engineer and demonstrate methodologies for performing intravital optical assessments, in living mice, of fluorescent biomarkers that indicate molecular expressions of disease or viability.

First, we engineered a flexible fiber-optic microendoscope for longitudinal optical imaging studies in a mouse model of disseminated ovarian cancer. This microendoscope has an outer diameter of 680 μm and achieves a lateral resolution of 4 μm . The instrument repetitively monitored the growth of fluorescence-expressing ovarian cancer cells in mice for over 4 weeks, visualizing single cells, cell clusters, and tumor masses. By establishing longitudinal (non-terminal) studies, this technology allows each animal to be used as its own control, significantly reducing the number of animals needed for experimentation.

We then employed fluorescence microendoscopy to validate the specific binding activity of a fluorescence-labeled peptide to colorectal dysplasia in a genetically-engineered mouse model. The microendoscope was passed through the instrument channel of a small animal endoscope for simultaneous wide-field and microscopic imaging. More than two-fold greater fluorescence intensity was measured from dysplastic tissue compared to adjacent normal mucosa.

In the third part of this dissertation we developed a label-free methodology employing a handheld fluorescence lifetime spectroscopy probe to optically assess tissue

engineered constructs that were implanted in living mice. Clinical translation of tissue engineered constructs requires noninvasive methods for assessing their integration with host tissue after grafting. Our instrumentation noninvasively sensed endogenous fluorophores in the tissue constructs that correlate to *in vitro* measures of cellular viability. Finally, we report the design and construction of a depth-resolved fluorescence lifetime spectroscopy system, which could be used for assessing the viability of tissue-engineered constructs with greater specificity than the demonstrated probe.

Chapter 1. Introduction

By combining innovative molecular biology with high resolution, fiber-based optical instrumentation, researchers and clinicians can now directly assess cellular and molecular processes in living tissues. *In vivo* assessment of molecular biomarkers in small animals can provide unique insights into disease pathogenesis, drug development, and effects of therapy [1]. Methods of intravital microscopy and spectroscopy that are based on fluorescence enable the quantitative and noninvasive assessment of a wealth of fluorescent molecular biomarkers that report on functional cellular information. These biomarkers include exogenous contrast agents for detecting over-expressed cell surface targets, fluorescent proteins that are engineered to be constitutively-expressed by cells, and endogenous fluorophores that are native to the tissues and allow label-free optical assessment. Advancement in this field will make a substantial impact on both basic and translational medical research.

This dissertation contains four projects that contribute to the technological advancement of intravital microscopy and spectroscopy of small animals. Applications of the projects include single cell imaging of tumor development, early detection of colon cancer, and label-free assessment of tissue engineered construct viability. Assessment modalities include fluorescence intensity imaging by microendoscopy and fluorescence lifetime spectroscopy. All of the instruments were designed with the potential for clinical translation as a key objective. In this chapter, we will introduce the concepts necessary to understand the four projects in the dissertation. We also review some other intravital assessment instruments and molecular biomarkers so that the reader may place this work into the context of the field.

1.1 Importance of Using Small Animal Models for Biomedical Research

Small animal models play an important role in the study of cellular and molecular function and disease. Small animal models allow the assessment of biology in its intact and native physiological state, rather than in reductionist systems such as cells in culture dishes or on slides [2]. The mouse is one of the most commonly used animal model systems. Mice are small in size, can be relatively quickly and easily bred in captivity, have a lifespan of 3 years, and have extensive physiological and molecular similarities to humans. Xenograft models are those in which tumor tissue or cell lines from one species are propagated in immunodeficiency mice. Genetically engineered mice harbor genetic modifications, and are often used to engineer mice that will develop tumors that accurately mimic pathophysiological and molecular features of human malignancies [3].

Mouse models have been especially critical in cancer research. The best mouse models are able to accurately recapitulate many aspects of human tumor physiology such as angiogenesis, tumor-stromal interaction, and hormone dependency [4]. For example, intravital imaging of mouse models of cancer has made it possible to quantify the behavior and function of the cellular and molecular components of the immune system that control tumor growth. These studies indicated that the behavior of immune cells in tissues is dictated by local factors in the tumor microenvironment that often cannot be reproduced *in vitro* [5].

In Chapter 2 of this dissertation we employ a xenograft model of human ovarian carcinoma with extensive intraperitoneal dissemination [6]. This model provides a means to assess the ability of our intravital assessment tool to monitor tumor growth and metastasis. In Chapter 3 we employ a genetically engineered mouse model of colon cancer, the CPC;*Apc* mouse [7]. CPC;*Apc* mice spontaneously develop colonic polyps in the distal intestine, which are accessible by our intravital instruments. In Chapter 4 we employ a xenograft model in which a tissue engineered construct manufactured from human cells is implanted under the skin of a mouse [8]. This enables pre-clinical evaluation of the efficacy of the construct.

1.2 Need for Intravital Assessment of Molecular Biomarkers

Whole-body imaging modalities available for intravital optical assessment of molecular biomarkers in small animals include bioluminescence imaging (BLI) and whole body fluorescence imaging. Advantages of these macroscopic techniques include true noninvasive assessment and high sensitivity. However, the spatial resolution of these modalities ranges from 1-10 mm. In this dissertation, we will focus on intravital microscopy and spectroscopy modalities based on fiber-optics that enable single cell and sub-cellular level resolution. We refer the reader to Weissleder and Pittet [9], and Massoud and Gambhir [10], for excellent comprehensive reviews of many intravital imaging modalities. In this section, we will discuss the need for intravital assessment for two of the applications contained in this dissertation: early detection of colon cancer and noninvasive assessment of tissue engineered construct viability.

1.2.1 Intravital Imaging of Tissue Epithelium for Colon Cancer

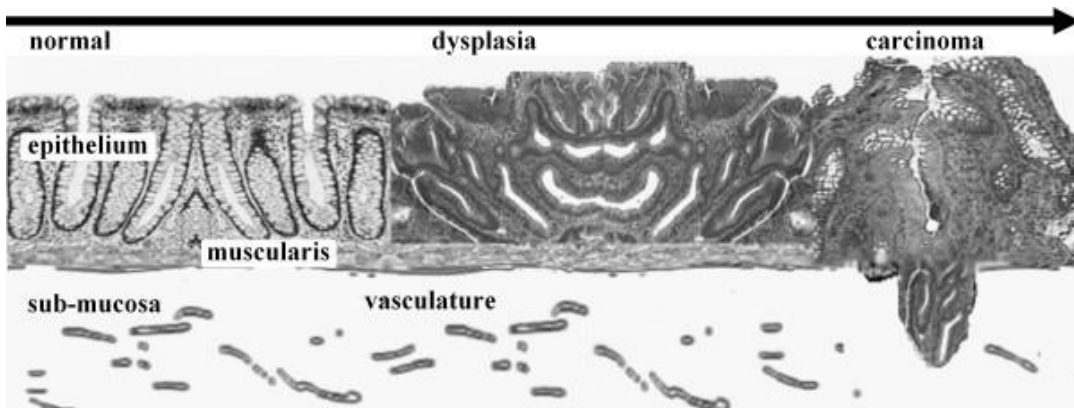


Fig. 1.1. Carcinoma of the colon arises from a transformation of normal epithelium to dysplasia. Subtle molecular changes develop first in the crypts prior to morphological changes in the tissue. An intravital microscope placed on the luminal surface of the tissue can be used to study the molecular progression of this disease longitudinally in small animal models.

Transformed cells that develop into colon cancer originate within the epithelium of the mucosa and ducts, as shown in **Fig. 1.1**. Normal colonic epithelium transforms into a pre-malignant condition (dysplasia) prior to evolving

into carcinoma [11]. Molecular changes develop well in advance of morphological changes. Intravital microscopy is a powerful tool for studying the molecular mechanisms of epithelial cancer biology *in vivo* because this technique can directly access this thin, superficial layer of tissue to provide the highest resolution possible in live animals [12-17]. A miniature fiber optic instrument can be placed in contact with the tissue surface to collect real time images with sub-cellular resolution. This technique can detect molecular changes in the study of the progression of colon cancer that cannot be observed by any other imaging modality. Additionally, intravital imaging allows for longitudinal (non-terminal) studies to be performed where each animal is used as its own control. This approach can significantly reduce the number of animals needed and can provide a more robust study design.

1.2.2 *Intravital Spectroscopy of Engineered Tissues*

The fields of tissue engineering and regenerative medicine (TERM) are at a stage where scientific advances are rapidly transitioning to clinical applications [18]. Compliance with regulatory oversight procedures established by government agencies is critical to ensure product safety and efficacy. Clinical translation in TERM requires evaluative tools to assess engineered tissue products and ensure manufacturing consistency (before implantation) and validate clinical efficacy (after implantation) [19].

Engineered tissues, like other drugs, can be validated for safety and efficacy using pre-clinical animal models. Intravital assessment of engineered tissues implanted in living mice can serve as an *in vivo* assay for testing safety and efficacy. Noninvasive optical assessments can characterize the specimens without interfering with their biochemical and physiological state. In particular, fluorescence spectroscopy (see Section 1.3.4) can quantitatively assess the metabolic state of the engineered tissues. Cell metabolism is critical to the health and integration of engineered tissues, and intravital spectroscopy allows quantitative characterization of metabolism in a noninvasive manner that is not possible with traditional punch biopsies [20, 21].

1.3 Overview of Intravital Fluorescence Imaging and Spectroscopy Techniques

1.3.1 Challenge for Miniaturizing Intravital Microscopes

One of the greatest challenges of performing high resolution (sub-cellular) optical assessments in live animal models is the ability to overcome motion artifact, including respiratory displacement, heart beating, and organ peristalsis. Conventional intravital microscopes use bulk optic objectives that are fixed to large, stationary platforms. As a result, motion will occur in live animals relative to the objective that appear exaggerated in the relatively small fields-of-view of intravital microscopes, typically on the order of several hundred microns. On the other hand, a miniaturized intravital microscope can have sufficiently small size and weight to move relative to the bodily motion of the animal during the imaging session, thus substantially reducing the motion artifact. Fiber coupling allows for the signal to be transmitted to the detector. Furthermore, the small size of these instruments provides much greater positioning accuracy onto target organs in the animal [22].

1.3.2 High Resolution Fluorescence Microendoscopy

High resolution fluorescence microendoscopy (HRME) involves optical probes that are typically less than 1 mm in outer diameter. HRMEs are based on coherent fiber-optic bundles that consist of up to ~100,000 individual step-index fibers. By placing all illumination and detection optics on the proximal end of the bundle, HRMEs are among the smallest diameter intravital microscopes available, some with outer diameter as small as 350 μm . However, this small diameter is only possible when using the HRME in a configuration without distal focusing optics, enabling only epifluorescence imaging of the sample surface (essentially, a working distance of zero). Thus, the size reduction comes with a sacrifice of functionality. Nonetheless, the HRME is a powerful, versatile modality that has been demonstrated for *in vivo* pre-clinical and even clinical use by several groups [23-30]. We use HRME instrumentation in Chapters 2 and 3.

1.3.3 Confocal Endomicroscopy

The use of light is a very powerful tool for measurement because this modality can achieve sub-cellular resolution in real time, a level of performance that cannot be matched by any other imaging modality. However, light is highly scattered by tissue, and sophisticated methods are needed to produce clear images. Confocal microscopy uses a pinhole placed in between the objective lens and the detector to allow only the light that originates from within a tiny volume below the tissue surface to be collected [31]. All other sources of scattered light do not have the correct path to be detected, and thus become spatially filtered. This process is known as optical sectioning and can produce a high resolution image from a thin slice of tissue below the surface.

In confocal endomicroscopy, the core of a single mode optical fiber acts as a spatial filter to reject scattered light that originates out of the focal plane [32]. Confocal endomicroscopy systems for real-time optical biopsies have been extensively developed since the first demonstration of a fiber-optic instrument in 1993 [33]. Two endoscope-compatible confocal systems are now commercially available. One is based on a miniaturized confocal microscope (Optiscan Pty. Ltd., Victoria, Australia) that is integrated into the distal tip of a videoendoscope (EC3870K, Pentax, Tokyo, Japan) [16]. The other (Mauna Kea Technologies, Paris, France) is based on a coherent fiber bundle that can be passed down the instrument channel of most standard medical endoscopes [15]. Several groups have demonstrated high resolution imaging in hollow organs throughout the body using these instruments [34-42].

1.3.4 Fiber-Optic Probe-Based Fluorescence Lifetime Spectroscopy

The modalities discussed thus far have all been examples of steady-state fluorescence intensity imaging. Fluorescence data can also be acquired as a function of wavelength, obtaining fluorescence spectra that reflect tissue morphology, optical absorption and scattering properties, and local biochemistry of the sample [43].

However, steady-state fluorescence spectroscopy neglects the dynamics of fluorescence decay, in the dimension of time. Fluorescence lifetime, the average time spent by a fluorophore in the excited state, is extremely sensitive to the local biochemical environment, and can therefore provide additional information about various biological parameters, such as pH, enzymatic activity, and redox state. Another advantage of fluorescence lifetime is that it can provide a contrast parameter for biological tissues that have overlapping emission spectra. Finally, fluorescence lifetime is especially beneficial for *in vivo* measurements, as it is independent of intensity variations, and can therefore provide robust quantitative results [43-45].

Acquisition of time-resolved spectra requires a pulsed laser excitation source with a pulse width on the order of 1 ns and high speed, highly sensitive detectors such as photomultiplier tubes, avalanche photodiodes, and streak cameras [46]. Fluorescence lifetime spectroscopy can be adapted for intravital applications by implementing fiber-optic probe configurations that enable remote light delivery and collection. Our group has previously described the design and development of a clinically-compatible, fiber-optic probe-based fluorescence lifetime spectroscopy system [47-49]. Utzinger and Richards-Kortum provide a comprehensive review of various fiber-optic probe designs that enable noninvasive, nondestructive, and repetitive spectral measurements [50].

1.4 Fluorescent Molecular Biomarkers

The clinical utility of the instruments described above can be greatly supplemented by integrating them with fluorescent molecular biomarkers that are highly specific for known targets. Intravital optical technologies allow for *in vivo* visualization and characterization of biological processes that occur on a cellular or sub-cellular scale based on protein expression [51]. These imaging agents are usually integrated with advanced endoscopic instruments that are sensitive to fluorescence. Targets for fluorescence assessment may be endogenous molecules that are intrinsic to the tissue (such as collagen or NADH), fluorescent proteins

(such as green fluorescent protein (GFP) or related molecules), or exogenous optical contrast agents with fluorescent molecules [1]. Applications include 1) basic research of studying signaling pathways and molecules by engineering fluorescent protein reporting mechanisms, 2) early cancer detection by imaging molecular changes that occur before gross morphological abnormalities; 3) personalized medicine by visualizing molecular targets specific to individual patients; 4) image guided therapy by localizing tumor margins and monitoring for recurrence [52], and 5) *in vivo* assays for testing of drugs and therapeutics.

1.4.1 Genetically Encoded Fluorescent Proteins for Basic Biomedical Research

The use of genetically encoded fluorescent proteins is widespread in basic biological sciences [9]. By imaging gene expression in small animal models, researchers can image cellular and molecular events. Constitutively-expressed fluorescent proteins could act as markers for localizing and tracking cells [4], such as for assessing tumor burden and metastasis as we did in Chapter 2. Or, cells could be engineered to express fluorescence to report on a specific biological process or pathway [10]. Other applications of fluorescent proteins in cancer research include the visualization of tumor cell invasion, metastatic seeding and colonization, angiogenesis, and the interaction between the tumor and its local environment. Since fluorescent proteins are genetically encoded, their use evades the need for systematic delivery of an imaging agent [2].

1.4.2 Endogenous Fluorophores for Label-Free Optical Assessment

Endogenous fluorophores naturally occur in living cells and tissues. The major advantage of assessing endogenous fluorescence (also called autofluorescence) is that the methodologies are label-free, and hence truly noninvasive. This is of great benefit to clinical translation, as it evades the need for regulatory approval of a drug that is administered to the patient, as is the case for exogenous contrast agents. Furthermore, label-free methods reduce the risk of compromising the sterility or integrity of the sample, when that is of concern, as in

the case of engineered tissue assessment in Chapters 3 and 4. A challenge for assessing autofluorescence is low quantum yield compared to exogenous agents, possibly necessitating longer exposures or more highly sensitive detectors to increase the signal-to-noise ratio.

Some endogenous fluorophores include NADH, flavins (e.g. FAD), tryptophan, and porphyrins [53]. Methodologies have been developed to optically assess cell redox ratios using autofluorescence measured from NADH and FAD [54, 55]. Highly relevant to intravital assessment methodologies is that the extracellular matrix (ECM) contains collagen and elastin, both of which are highly autofluorescent [43, 44, 53]. This is beneficial when the ECM is the target of interest, for example for the noninvasive evaluation of engineered articular cartilage [56, 57] and engineered bone constructs [58]. However, when the fluorescence target is epithelial cells or other targets surrounded by ECM, autofluorescence may reduce the target-to-background ratio.

1.4.3 Exogenous Molecular Probes for Targeting of Cancer Biomarkers

The best exogenous molecular probes are highly specific for their biological targets, active only in the presence of disease, and much more intense than the surrounding background. For clinical use, the ideal probe should have rapid binding kinetics (time scale of minutes), be easy to label with fluorescent agents in multiple colors, and have capability for low cost, large scale synthesis [59]. The two most common classes of probes being developed for clinical use include antibodies and peptides. Antibodies are highly specific for known targets, but have been difficult to translate into the clinic because of delivery challenges, long serum half-lives, and immunogenicity. Peptides are short chains of amino acids that have been successfully selected using phage display technologies that consist of high diversity, unbiased libraries. However, the process for selecting specific peptides and identifying their molecular targets can be challenging. While their binding affinity is not as high as that of antibodies, peptides are much smaller in size, easy to label with fluorescent dyes, have rapid binding kinetics, and minimal immunogenicity.

Molecular probe platforms include activatable, antibody/affibody, small molecule, peptide, and aptamer, as shown in **Fig. 1.2**. Activatable probes are designed to generate fluorescence only after coming into contact with the target. These "smart" probes are fluorescently quenched in their native state, and are activated when cleaved by tumor-associated proteases, such as cathepsin and matrix metalloproteinases which play an important role in cell proliferation, invasion, apoptosis, angiogenesis, and metastasis [60]. Antibodies are widely used Y-shaped gamma globulins (IgG) that bind specifically to antigenic targets. They can be labeled with a large selection of fluorescent dyes, and have been developed for several molecular targets that have great clinical relevance, including human epidermal growth factor receptor (HER2) and epidermal growth factor receptor (EGFR) [38]. Antibodies may elicit an immune reaction with repeated use, and are costly to produce in large quantities. Affibodies are small single domain proteins that are desirable because of their small size, leading to rapid tumor localization and fast clearance [61]. Their utility has been demonstrated for *in vivo* targeting and detection of tumors that over express HER2. "Small molecule" probes have been developed for imaging that are activated by a change in pH after entering a target cell and merging with lysosomes [62]. These probes require a targeting moiety such as HER2 antibody to attach to the cell. Since non-activated probes do not emit a signal, the target-to-background ratio is greatly improved. Aptamers are single-stranded, nuclease-resistant DNA or RNA molecules [63], and have recently been developed with high affinity and specificity for DLD-1 and HCT 116 colorectal cancer cell lines *in vitro*, but this has not yet been demonstrated *in vivo*.

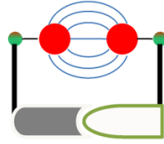
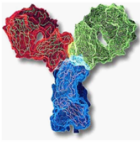
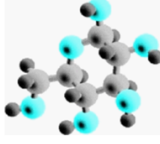

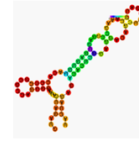
	Activatable	Antibody/ Affibody	Small Molecule	Peptide	Aptamer
Molecular Probe					
Strengths	amplification ↑ target/background known targets	↑ specificity ↑ diversity ↑ affinity known targets	↓ background reversible flexible labeling	↓ size ↑ diversity ↓ immunogenicity ↓ cost	↓ size ↑ diversity ↓ immunogenicity ↑ affinity
Weaknesses	↓ signal few probes ? toxicity	immunogenicity ↑ cost ↓ quantity	variable specificity ? toxicity	↓ affinity ↓ Possible degradation	↑ cost ↓ quantity ? toxicity

Fig. 1.2. Exogenous molecular probe platforms. Strengths and weaknesses of various probe platforms being developed for targeted imaging are presented [64].

Targets unique to disease can be over-expressed both on the cell-surface as well as within the cytoplasm. For purposes of imaging, the pharmacokinetics of molecular probes that bind to the cell surface are more predictable than those that are internalized and broken down by proteolytic enzymes. Epidermal growth factor receptor (EGFR), HER2/neu (ERBB2), and vascular endothelial growth factor (VEGF) receptor are over-expressed in several cancers, including esophageal, colorectal, breast, and ovarian. Somatostatin receptors (SSTR) are overexpressed in neuroendocrine tumors [65]. Over-expressed proteolytic enzymes activate “smart” probes such as cathepsin-B and matrix metalloproteinases (MMPs) [66, 67]. Apoptosis reporters frequently utilize effector caspases as targets [68].

Targeted molecular imaging has been demonstrated mostly in the colon thus far, using different types of probes on a variety of instrumentation platforms. A fluorescein-labeled monoclonal antibody against EGFR has been imaged using confocal laser endomicroscopy in a xenograft mouse model of colorectal cancer [38]. Image analysis indicated that fluorescence intensity was higher in tumors that have high EGFR expression than those with low EGFR expression. Clinical use of peptides was demonstrated for early detection of colorectal cancer using the FITC-labeled sequence VRPMLQ [39]. The peptide bound more specifically to dysplastic

colonocytes than to adjacent normal cells with 81% sensitivity and 82% specificity on confocal laser endomicroscopy. Molecular imaging has also been demonstrated for early detection of esophageal cancer. Li *et al.* recently identified the peptide SNFYMPL that preferentially binds to high-grade dysplasia in Barrett's esophagus on excised human specimens, and plans have been made to study this peptide in a Phase 1 clinical trial [69]. Another FITC-labeled peptide, ASYNYDA, has been selected to target dysplastic esophageal mucosa [52]. This peptide has recently been demonstrated to identify esophageal neoplasia over Barrett's esophagus and squamous epithelium with 75% sensitivity and 97% specificity in a clinical study using an intravital confocal endomicroscope [42].

1.5 Dissertation Objectives

The global aim for all projects in this dissertation is to develop intravital methodologies based on fluorescence for assessing molecular biomarkers in living mice, in real time. The four projects contained in this dissertation can be split into two categories: 1) Minimally-invasive fluorescence microendoscopy of exogenous fluorescent biomarkers for assessing molecular expressions of cancer, and 2) Noninvasive label-free fluorescence lifetime spectroscopy of endogenous fluorescent biomarkers for assessing integration of tissue engineered constructs.

Specific Aim 1: Engineer a flexible fiber-optic microendoscope for longitudinal optical imaging studies in a mouse model of disseminated ovarian cancer. Large dimensions of fiber bundle-based microendoscopes necessitate terminal procedures in mice. Longitudinal imaging allows observation of disease development and/or response to therapy over time, and use of each animal as its own control, significantly reducing the number of animals needed. Here, we repetitively monitored intraperitoneal growth of GFP-positive ovarian cancer tumors in mice for over 4 weeks. This project established technology for minimally-invasive, longitudinal imaging with single cell resolution, advancing future molecular imaging studies of ovarian cancer and other diseases.

Specific Aim 2: Validate specific binding of a targeted fluorescence-labeled peptide, *in vivo*, to murine colorectal dysplasia using fiber-bundle based fluorescence microendoscopy. Molecular changes in pre-malignant colorectal mucosa develop prior to morphological changes. Intravital imaging of targeted molecular probes on a sub-cellular level in small animals can be used to study molecular progression of cancer over time. Here, we used a microendoscope similar to that developed in Specific Aim 1 in combination with a wide-field small animal endoscope to perform targeted molecular imaging of colorectal dysplasia in living mice. This project demonstrated a rigorous methodology for multi-scale validation of a novel targeting agent being developed to localize disease that can be generalized to hollow organs.

Specific Aim 3: Assess post-implantation integration of tissue engineered constructs with native mouse tissue using label-free, quantitative, noninvasive fluorescence lifetime spectroscopy. Clinical translation of *ex vivo* tissue engineered constructs requires noninvasive methods to assess construct health and viability. Current practices for post-implantation assessment are either qualitative or destructive. Here, we employed a hand-held fluorescence lifetime spectroscopy probe to optically assess constructs that were implanted in living mice. Optical parameters measured from endogenous fluorophores correlated with *in vitro* measures of cellular viability. This project demonstrated feasibility of clinical optical diagnostic tools based on fluorescence lifetime sensing to non-invasively monitor post-implantation integration of engineered tissues, which is currently an unmet clinical need.

Specific Aim 4: Engineer a portable depth-resolved fluorescence lifetime spectrometer for preferential optical assessment of the living cell layer of tissue engineered constructs. Bulk fluorescence spectroscopy systems, such as that demonstrated in Specific Aim 3, have low spatial resolution. This creates a challenge for assessing epithelial tissue engineered constructs, because strong background fluorescence signal from the dermal and keratin layers interferes

with the fluorescence signal of interest, originating from the thin living cell layer. Here, we design and construct a depth-resolved fluorescence lifetime spectrometer that effectively suppresses the strong keratin and collagen fluorescence and extracts the epithelial fluorescence. The instrument is portable and designed for intravital assessment of living mice. This project is in progress, and plans to overcome design challenges are discussed.

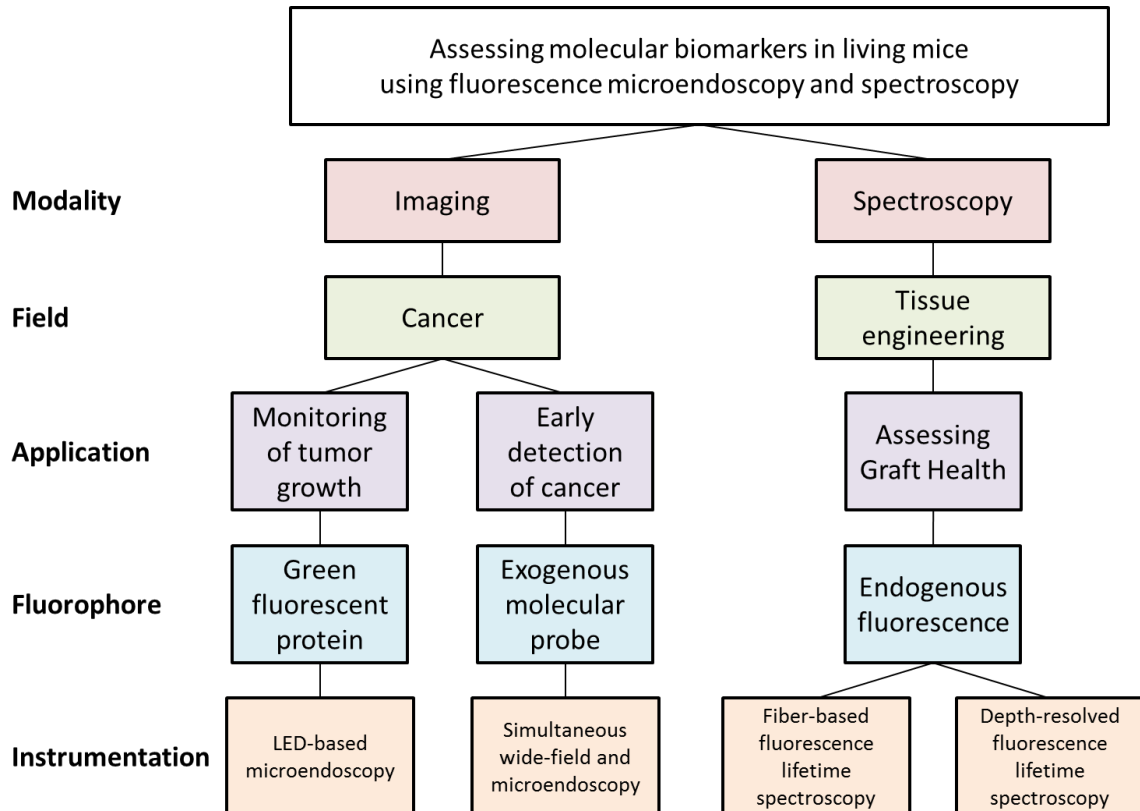


Fig. 1.3. Overview of dissertation projects. Chapters 2 and 3 use fluorescence imaging techniques for applications in cancer. Chapters 4 and 5 use fluorescence lifetime spectroscopy techniques for assessing tissue engineered construct health.

1.6 Dissertation Overview

Chapter 1 introduces background and motivation for fluorescence-based optical technologies for intravital assessment of molecular biomarkers. Portions of this chapter have been published in a review paper in the Journal of Biophotonics.

Elahi SF and Wang TD, "Future and advances in endoscopy," J Biophotonics 4(7-8): 471-481, 2011.

Chapter 2 corresponds to Specific Aim 1. We describe the development of a LED-based flexible fiber-optic microendoscope and demonstrate repetitive molecular imaging of disseminated ovarian cancer in living mice. This study represents a significant improvement over existing instruments, delivering high illumination power through a fiber bundle that is sufficiently small to allow repetitive imaging studies to monitor tumor growth deep within living animals over a longer time span than previously demonstrated. This chapter has been published in the journal Molecular Imaging and Biology.

Elahi SF, Liu Z, Luker KE, Kwon RS, Luker GD, Wang TD, "Longitudinal molecular imaging with single cell resolution of disseminated ovarian cancer in mice with a LED-based confocal microendoscope," Mol Imaging Biol 13(6): 1157-1162, 2011.

Chapter 3 corresponds to Specific Aim 2. We demonstrate a methodology for validation of selective binding of a fluorescence-labeled peptide to colonic dysplasia with sub-cellular resolution in living mice using a microendoscope. This methodology was the first demonstration of multi-scale, simultaneous wide-field fluorescence endoscopy and high resolution microendoscopy in living mice. This chapter has been published in the journal Biomedical Optics Express.

Elahi SF, Miller SJ, Joshi B, Wang TD, "Targeted imaging of colorectal dysplasia in living mice with fluorescence microendoscopy," Biomedical Optics Express 2(4): 981-986, 2011.

Chapter 4 corresponds to Specific Aim 3. We employ a hand-held fluorescence lifetime spectroscopy probe for quantitative, label-free noninvasive assessment

post-implantation tissue integration of tissue engineered constructs in mice. We develop quantitative data analysis methods and correlated optical parameters measured *in vivo* to *in vitro* measures of cellular viability. At the time of this writing, this chapter is in preparation to be submitted to the journal Tissue Engineering Part C: Methods.

Chapter 5 corresponds to Specific Aim 4. We describe the design and construction of an instrument capable of finer resolution depth-sectioning than the system presented in Chapter 4. This chapter includes detailed engineering analyses of the optical design of the instrument. Pitfalls and challenges are discussed. This chapter serves as a manual and guide for future researchers to progress this work and use the system to quantitatively assess cellular metabolic activity of the thin living cell layer of epithelial tissue engineered constructs.

Chapter 6 concludes the dissertation, emphasizing scientific contributions described in this dissertation and future work.

References

1. G. D. Luker and K. E. Luker, J. Nucl. Med. **49**, 1-4 (2008).
2. Rao, A. Dragulescu-Andrasi, and H. Yao, Curr. Opin. Biotechnol. **18**, 17-25 (2007).
3. K. K. Frese and D. A. Tuveson, Nat. Rev. Cancer. **7**, 645-658 (2007).
4. S. K. Lyons, J. Pathol. **205**, 194-205 (2005).
5. C. Sumen, T. R. Mempel, I. B. Mazo, and U. H. von Andrian, Immunity **21**, 315-329 (2004).
6. K. L. Molpus, D. Koelliker, L. Atkins, D. T. Kato, J. Buczek-Thomas, A. F. Fuller Jr, and T. Hasan, Int. J. Cancer **68**, 588-595 (1996).
7. T. Hinoi, A. Akyol, B. K. Theisen, D. O. Ferguson, J. K. Greenson, B. O. Williams, K. R. Cho, and E. R. Fearon, Cancer Res. **67**, 9721-9730 (2007).
8. K. Izumi, S. E. Feinberg, H. Terashi, and C. L. Marcelo, Tissue Eng. **9**, 163-174 (2003).
9. R. Weissleder and M. J. Pittet, Nature **452**, 580-589 (2008).
10. T. F. Massoud and S. S. Gambhir, Genes Dev. **17**, 545-580 (2003).
11. Robbins SL & Cotran RS (1979) *Pathologic basis of disease*, (Saunders,

12. P. M. Delaney, R. G. King, J. R. Lambert, and M. R. Harris, *J. Anat.* **184 (Pt 1)**, 157-160 (1994).
13. B. A. Flusberg, E. D. Cocker, W. Piyawattanametha, J. C. Jung, E. L. Cheung, and M. J. Schnitzer, *Nat. Methods* **2**, 941-950 (2005).
14. S. H. Yun, G. J. Tearney, B. J. Vakoc, M. Shishkov, W. Y. Oh, A. E. Desjardins, M. J. Suter, R. C. Chan, J. A. Evans, I. K. Jang, N. S. Nishioka, J. F. de Boer, and B. E. Bouma, *Nat. Med.* **12**, 1429-1433 (2006).
15. T. D. Wang, S. Friedland, P. Sahbaie, R. Soetikno, P. L. Hsiung, J. T. Liu, J. M. Crawford, and C. H. Contag, *Clin. Gastroenterol. Hepatol.* **5**, 1300-1305 (2007).
16. R. Kiesslich, J. Burg, M. Vieth, J. Gnaendiger, M. Enders, P. Delaney, A. Polglase, W. McLaren, D. Janell, S. Thomas, B. Nafe, P. R. Galle, and M. F. Neurath, *Gastroenterology* **127**, 706-713 (2004).
17. M. Goetz, C. Fottner, E. Schirmacher, P. Delaney, S. Gregor, C. Schneider, D. Strand, S. Kanzler, B. Memadathil, E. Weyand, M. Holtmann, R. Schirmacher, M. M. Weber, M. Anlauf, G. Kloppel, M. Vieth, P. R. Galle, P. Bartenstein, M. F. Neurath, and R. Kiesslich, *Endoscopy* **39**, 350-356 (2007).
18. M. B. Fisher and R. L. Mauck, *Tissue Eng. Part B. Rev.* **19**, 1-13 (2013).
19. M. H. Lee, J. A. Arcidiacono, A. M. Bilek, J. J. Wille, C. A. Hamill, K. M. Wonnacott, M. A. Wells, and S. S. Oh, *Tissue Eng. Part B. Rev.* **16**, 41-54 (2010).
20. I. Georgakoudi, W. L. Rice, M. Hronik-Tupaj, and D. L. Kaplan, *Tissue Eng. Part B. Rev.* **14**, 321-340 (2008).
21. I. Georgakoudi and K. P. Quinn, *Annu. Rev. Biomed. Eng.* **14**, 351-367 (2012).
22. C. S. Croix, W. R. Zipfel, and S. C. Watkins, *BioTechniques* **43**, 14-19 (2007).
23. S. F. Elahi, Z. Liu, K. E. Luker, R. S. Kwon, G. D. Luker, and T. D. Wang, *Mol. Imaging Biol.* (2010).
24. S. F. Elahi, S. J. Miller, B. Joshi, and T. D. Wang, *Biomed. Opt. Express* **2**, 981-986 (2011).
25. T. J. Muldoon, M. C. Pierce, D. L. Nida, M. D. Williams, A. Gillenwater, and R. Richards-Kortum, *Opt. Express* **15**, 16413-16423 (2007).
26. T. J. Muldoon, S. Anandasabapathy, D. Maru, and R. Richards-Kortum, *Gastrointest. Endosc.* **68**, 737-744 (2008).
27. T. J. Muldoon, N. Thekkek, D. Roblyer, D. Maru, N. Harpaz, J. Potack, S. Anandasabapathy, and R. Richards-Kortum, *J. Biomed. Opt.* **15**, 026027 (2010).
28. T. J. Muldoon, D. Roblyer, M. D. Williams, V. M. Stepanek, R. Richards-Kortum, and A. M. Gillenwater, *Head Neck* **34**, 305-312 (2012).
29. K. J. Rosbach, D. Shin, T. J. Muldoon, M. A. Quraishi, L. P. Middleton, K. K. Hunt, F. Meric-Bernstam, T. K. Yu, R. R. Richards-Kortum, and W. Yang, *Biomed. Opt. Express* **1**, 911-922 (2010).
30. W. Zhong, J. P. Celli, I. Rizvi, Z. Mai, B. Q. Spring, S. H. Yun, and T. Hasan, *Br. J. Cancer* **101**, 2015-2022 (2009).
31. Pawley JB (2006) *Handbook of Biological Confocal Microscopy*,
32. T. Dabbs and M. Glass, *Appl. Opt.* **31**, 3030-3035 (1992).
33. A. F. Gmitro and D. Aziz, *Opt. Lett.* **18**, 565 (1993).
34. A. L. Polglase, W. J. McLaren, S. A. Skinner, R. Kiesslich, M. F. Neurath, and P. M. Delaney, *Gastrointest. Endosc.* **62**, 686-695 (2005).

35. A. L. Polglase, W. J. McLaren, and P. M. Delaney, *Expert Rev. Med. Devices* **3**, 549-556 (2006).
36. R. Kiesslich, L. Gossner, M. Goetz, A. Dahlmann, M. Vieth, M. Stolte, A. Hoffman, M. Jung, B. Nafe, P. R. Galle, and M. F. Neurath, *Clin. Gastroenterol. Hepatol.* **4**, 979-987 (2006).
37. E. M. Bott, I. R. Young, G. Jenkin, and W. J. McLaren, *Am. J. Obstet. Gynecol.* **194**, 105-112 (2006).
38. M. Goetz, A. Ziebart, S. Foersch, M. Vieth, M. J. Waldner, P. Delaney, P. R. Galle, M. F. Neurath, and R. Kiesslich, *Gastroenterology* **138**, 435-446 (2010).
39. P. L. Hsiung, J. Hardy, S. Friedland, R. Soetikno, C. B. Du, A. P. Wu, P. Sahbaie, J. M. Crawford, A. W. Lowe, C. H. Contag, and T. D. Wang, *Nat. Med.* **14**, 454-458 (2008).
40. G. A. Sonn, K. E. Mach, K. Jensen, P. L. Hsiung, S. N. Jones, C. H. Contag, T. D. Wang, and J. C. Liao, *J. Endourol.* **23**, 197-201 (2009).
41. H. Pohl, T. Rosch, M. Vieth, M. Koch, V. Becker, M. Anders, A. C. Khalifa, and A. Meining, *Gut* **57**, 1648-1653 (2008).
42. M. B. Sturm, B. P. Joshi, S. Lu, C. Piraka, S. Khondee, B. J. Elmunzer, R. S. Kwon, D. G. Beer, H. D. Appelman, D. K. Turgeon, and T. D. Wang, *Sci. Transl. Med.* **5**, 184ra61 (2013).
43. Lakowicz JR (2006) *Principles of Fluorescence Spectroscopy*, (Springer, New York),
44. Mycek M- & Pogue BW (2003) *Handbook of Biomedical Fluorescence*, (Marcel Dekker, Inc., New York),
45. L. Marcu, *Ann. Biomed. Eng.* **40**, 304-331 (2012).
46. W. R. Lloyd, L. -. Chen and M. -. Mycek, in: Morgan SP, Rose FRAJ & Mather SJ (eds.), *Optical Techniques in Regenerative Medicine* (CRC Press, 2014) pp. 171-203.
47. J. D. Pitts and M. -. Mycek, *Review of Scientific Instruments* **72**, 3061-3072 (2001).
48. K. Vishwanath, B. Pogue, and M. A. Mycek, *Phys. Med. Biol.* **47**, 3387-3405 (2002).
49. M. Chandra, K. Vishwanath, G. D. Fichter, E. Liao, S. J. Hollister, and M. A. Mycek, *Opt. Express* **14**, 6157-6171 (2006).
50. U. Utzinger and R. R. Richards-Kortum, *J. Biomed. Opt.* **8**, 121-147 (2003).
51. R. Weissleder, *Science* **312**, 1168 (2006).
52. M. Goetz and T. D. Wang, *Gastroenterology* **138**, 828-33.e1 (2010).
53. Prasad PN (2004) *Introduction to biophotonics*, (John Wiley & Sons,
54. M. C. Skala, K. M. Riching, A. Gendron-Fitzpatrick, J. Eickhoff, K. W. Eliceiri, J. G. White, and N. Ramanujam, *Proc. Natl. Acad. Sci. U. S. A.* **104**, 19494-19499 (2007).
55. M. Skala and N. Ramanujam, *Methods Mol. Biol.* **594**, 155-162 (2010).
56. T. Kutsuna, M. Sato, M. Ishihara, K. S. Furukawa, T. Nagai, M. Kikuchi, T. Ushida, and J. Mochida, *Tissue Eng. Part C. Methods* **16**, 365-373 (2010).
57. Y. Sun, D. Responde, H. Xie, J. Liu, H. Fatakdawala, J. Hu, K. A. Athanasiou, and L. Marcu, *Tissue Eng. Part C. Methods* **18**, 215-226 (2012).

58. P. Ashjian, A. Elbarbary, P. Zuk, D. A. DeUgarte, P. Benhaim, L. Marcu, and M. H. Hedrick, *Tissue Eng.* **10**, 411-420 (2004).
59. M. Li and T. D. Wang, *Gastrointest. Endosc. Clin. N. Am.* **19**, 283-298 (2009).
60. U. Mahmood, *Molecular Cancer Therapeutics* **2**, 489 (2003).
61. V. Tolmachev, A. Orlova, F. Y. Nilsson, J. Feldwisch, A. Wennborg, and L. Abrahmsen, *Expert Opin. Biol. Ther.* **7**, 555-568 (2007).
62. Y. Urano, D. Asanuma, Y. Hama, Y. Koyama, T. Barrett, M. Kamiya, T. Nagano, T. Watanabe, A. Hasegawa, P. L. Choyke, and H. Kobayashi, *Nat. Med.* **15**, 104-109 (2009).
63. K. Sefah, L. Meng, D. Lopez-Colon, E. Jimenez, C. Liu, and W. Tan, *PLoS One* **5**, e14269 (2010).
64. S. F. Elahi and T. D. Wang, *J. Biophotonics* **4**, 471-481 (2011).
65. K. E. Oberg, J. C. Reubi, D. J. Kweskeboom, and E. P. Krenning, *Gastroenterology* **139**, 742-53, 753.e1 (2010).
66. A. Faust, B. Waschkau, J. Waldeck, C. Holtke, H. J. Breyholz, S. Wagner, K. Kopka, W. Heindel, M. Schafers, and C. Bremer, *Bioconjug. Chem.* **19**, 1001-1008 (2008).
67. C. Bremer, S. Bredow, U. Mahmood, R. Weissleder, and C. H. Tung, *Radiology* **221**, 523-529 (2001).
68. K. E. Bullok, D. Maxwell, A. H. Kesarwala, S. Gammon, J. L. Prior, M. Snow, S. Stanley, and D. Piwnica-Worms, *Biochemistry* **46**, 4055-4065 (2007).
69. M. Li, C. P. Anastassiades, B. Joshi, C. M. Komarck, C. Piraka, B. J. Elmunzer, D. K. Turgeon, T. D. Johnson, H. Appelman, D. G. Beer, and T. D. Wang, *Gastroenterology* **139**, 1472-1480 (2010).

Chapter 2. **Longitudinal Imaging of Mice using a LED-Based Microendoscope**

2.1 Introduction

Intravital microscopes are extremely powerful tools for performing *in vivo* cellular and molecular imaging in small animal models [1]. Unlike whole body imaging techniques that detect light remotely [2], intravital microscopy allows monitoring of signal transduction and cell functions at single cell or even sub-cellular resolution. Microscopic imaging can be performed repetitively in mice to observe disease development and/or response to therapy over time if instruments are sufficiently small in dimension. A key benefit of longitudinal imaging is that each animal can be used as its own control, thus significantly reducing the numbers needed to achieve statistical validity [3].

Although repetitive intravital imaging has been performed using surgically-implanted optical windows, this approach is highly invasive and is limited to imaging superficial structures [4]. Furthermore, objectives on conventional microscopes used for intravital imaging are bulky and require wide exposure, often necessitating terminal procedures rather than serial studies [5,6]. Thus, a miniature intravital microscope that can access regions deep within the body to perform longitudinal (survival) studies with sub-cellular resolution represents a significant advance in the field of molecular imaging.

The development of flexible optical fibers has led to important advances in the miniaturization of these instruments for high resolution *in vivo* imaging in the clinic [7-9] as well as in small animals [10-12]. In general, these systems use a laser

source and a scanning mechanism to create the image. However, these components can increase the cost and size of the instrument. Recently, inexpensive but powerful LEDs have become available in a wide range of colors, providing a Lambertian radiation pattern that delivers a relatively uniform beam to individual fibers over the face of a bundle and eliminates the need for a scanning mechanism. This simple approach has been demonstrated previously to achieve a robust, low-cost system using charge-coupled device (CCD) imaging [13,14]. A longitudinal study using this type of instrument to monitor tumor response to therapy in two imaging sessions over a span of 5 days was recently demonstrated, albeit using a more expensive electron-multiplying CCD (EMCCD) camera [15].

In this study, we developed an optical model to improve the system design parameters to maximize light throughput, allowing for use of smaller caliber optical bundles with more output power. This model is needed because light emerges from the source with a large divergence angle and renders efficient coupling into the bundle to be a challenge. This new system provides greater sensitivity for fluorescence detection using a lower-cost CCD camera, while minimizing trauma to the animal. To test this instrument for *in vivo* imaging, we established ovarian cancer cells stably transduced with green fluorescent protein (GFP) and used these cells in a mouse model of disseminated, intraperitoneal ovarian cancer. The smaller size of the microendoscope allowed for repetitive imaging studies to monitor tumor growth deep within living animals over a longer time span than previously demonstrated.

2.2 Methods

2.2.1 System design of LED-based fluorescence microendoscope

A schematic of the imaging system is shown in **Fig. 2.1**. A LED light source (Luxeon K2, Philips Lumileds, San Jose, CA) produces emission centered at 470 nm with a spectral bandwidth of 25 nm at full-width-half-max (FWHM) with a power of 21 lumens [16]. A 488 nm short pass filter (SPF, Semrock FF01-518/SP-25) is used

to limit the excitation bandwidth. An aspheric lens collimates the beam onto the back aperture of an infinity-corrected objective lens (Olympus UIS2 PLN 20X, Tokyo, Japan) after reflection by a 495 nm dichroic beamsplitter (Semrock FF495-Di02-25x36). The flexible optical fiber bundle (Sumitomo IGN-06/17, Osaka, Japan) has $\sim 17,000$ individual fibers with $NA = 0.35$, a core diameter of $2.4 \mu\text{m}$, and core-to-core spacing of $\sim 4 \mu\text{m}$. The outer diameter is $680 \mu\text{m}$, the diameter of the active optical area is $540 \mu\text{m}$, and the length is 2.1 m. The fluorescence image is transferred back through the bundle through the objective and dichroic and focused by a condenser onto a CCD camera (Photometrics CoolSnapEZ, Tucson, AZ). A 500 nm long-pass filter (LPF, Semrock BLP01-488R-25) blocks the reflected excitation light. The distal face of the fiber bundle (**Fig. 2.1**, inset) is polished using 5-, 3-, and 1- μm grit paper using a custom chuck that keeps the bundle flat.

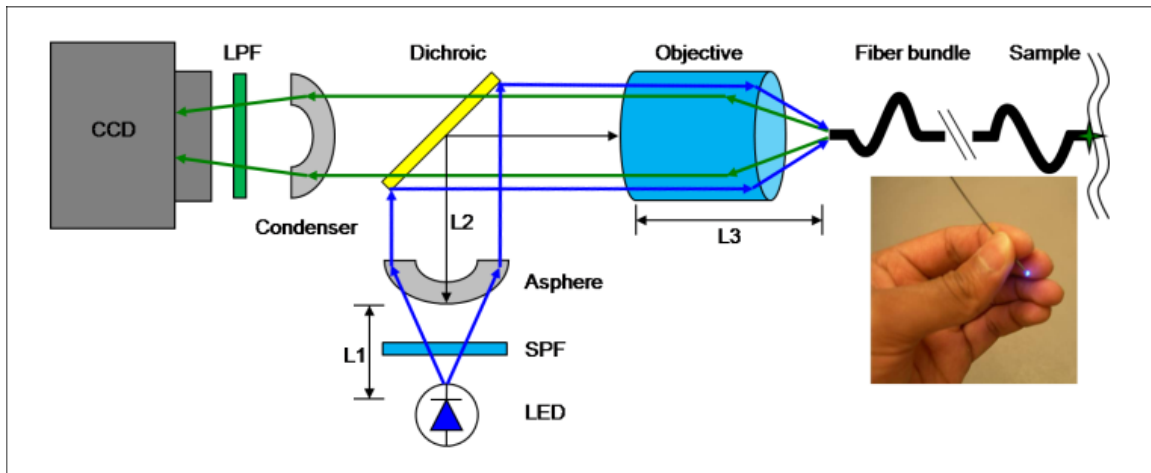


Fig. 2.1. LED-based microendoscope design schematic. Excitation from LED at 470 nm is collimated by an asphere, reflected by a dichroic beamsplitter, and focused into a $680 \mu\text{m}$ (O.D.) coherent fiber bundle. Fluorescence is transmitted to the CCD. The distal end of the fiber (inset) is placed into contact with the tissue.

2.2.2 Optical model to optimize coupling efficiency of LED source into fiber bundle

We developed an optical model to optimize the system parameters for coupling the LED source into the fiber bundle. We used a 20X objective lens ($NA = 0.4$, $f = 9 \text{ mm}$) to closely match the NA of the fiber bundle. The condenser contains the image of the active area on the proximal face of the fiber bundle within the

surface area of the CCD detector. In order to achieve this requirement, the relay magnification must meet the condition $M \leq W_{\text{CCD}}/D_{\text{fb}}$, where W_{CCD} is the dimension of the CCD and D_{fb} is the active diameter of the fiber bundle. The CCD array has dimensions of 8.98 x 6.71 mm, and $D_{\text{fb}} = 540 \mu\text{m}$, so $M_{\text{max}} = 12.4$. In order to optimally fill the CCD, we chose an off-the-shelf condenser lens with $f = 100 \text{ mm}$, providing a relay magnification $M = 11.1$. The CCD pixels are square with a dimension of $6.45 \mu\text{m}$, and with magnification, the core spacing of the image of the bundle face on the CCD is $\sim 44 \mu\text{m}$. Thus, the system resolution is limited by the core spacing of fibers in the bundle rather than by the pixels of the CCD detector.

Light from the LED is produced by a square die with dimensions of 1 mm x 1 mm and is emitted with a FWHM angle of $\sim 150 \text{ deg}$ [16]. We designed a telescopic lens system to effectively couple light that emerges with this high divergence angle into the fiber bundle. An asphere provides a larger effective aperture than a comparable spherical lens. We developed an optical model in Zemax® to simulate the intensity after the fiber bundle to optimize the parameters L1, L2, and L3. The transmission of light through the various components of the system is addressed by this model in four areas: 1) Only rays incident within the clear aperture of the asphere are collected; 2) Light transmitted by the objective is determined by the dimension of the back aperture; 3) Light captured by the bundle is determined by the NA of the individual fibers; and 4) Excitation collected by the bundle is determined by the area of the LED die imaged onto the proximal face.

2.2.3 Transduction and in vitro imaging of GFP-expressing ovarian cancer cells

We used a lentiviral vector to stably transduce human HeyA8 ovarian cancer cells with GFP [17,18]. Cells were cultured in DMEM with 10% FBS. The distal end of the optical fiber bundle was positioned in direct contact with the cells. We also collected fluorescence images using a standard epifluorescence microscope (Nikon Eclipse TE2000-U). The target-background ratio was determined by dividing the mean intensity of a 10x10 pixel array from the cytoplasm of 5 cells by the average value of a 10x10 pixel array from 5 regions in between cells. The signal-to-noise

ratio (SNR) was evaluated by dividing the mean intensity of a 10x10 pixel array in the cytoplasm by the standard deviation of the array, using 5 cells. All images were analyzed using NIH Image J® software.

2.2.4 Longitudinal *in vivo* imaging of tumor xenografts in mice

All animal experiments were approved by the University of Michigan Committee for Use and Care of Animals (UCUCA). We implanted 10^6 HeyA8-GFP cells into the peritoneal cavity of $n = 10$ adult female nude mice (Taconic, NCRNU-M-FHomozygousCrTac:NCr-Foxn1nu). Imaging started 1 week later and continued at weekly intervals. Mice were placed supine and administered 0.1 mg/kg buprenorphine s.c. for analgesia and 2% isoflurane via nose cone for anesthesia. The abdomen was prepared in sterile fashion. An 18G needle was passed percutaneously into the peritoneum to introduce a 16G angiocatheter. The needle was removed and the fiber-optic bundle was passed through the catheter and manipulated through the peritoneal cavity as shown in **Fig. 2.2**. Images were acquired with an exposure of 100 ms. Each imaging study lasted 5 to 10 minutes. Control images were obtained from the capsule of the liver and from the liver of a mouse not injected with tumor cells, and autofluorescence intensity was measured using NIH Image J® software. Imaging was repeated on the same cohort of mice for up to 4 weeks or until mice were euthanized due to tumor burden.

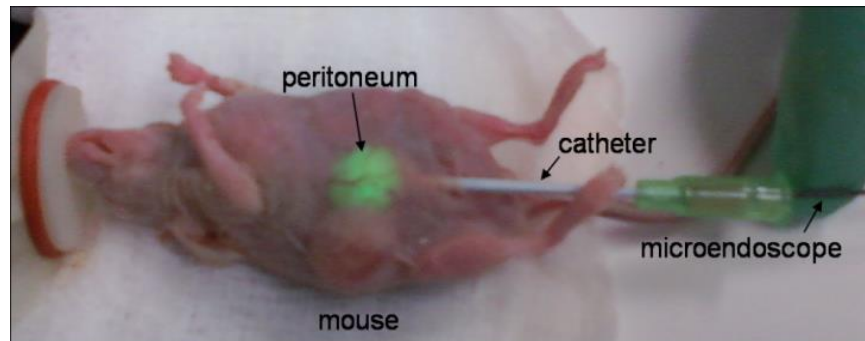


Fig. 2.2. Longitudinal imaging approach. The distal tip of the microendoscope is introduced with an 18G needle into the peritoneum through a catheter to collect fluorescence (green) from implanted HeyA8 ovarian tumor. The mice survive without need for closure of the wound.

2.3 Results

2.3.1 Microendoscope characterization

We measured a field of view of 540 μm and a lateral resolution of 3.9 μm using a standard resolution target (USAF). This result is consistent with the average spacing in between the cores of the individual fibers. We measured a power of 0.70 mW of excitation light at the distal end of the fiber bundle. Since there is no lens at the distal end of the bundle, the working distance is zero.

2.3.2 Optical model prediction of fiber bundle output light intensity

Based on our analysis and simulated results, we selected an asphere with $f_{\text{asp}} = 18$ mm. The results of our model reveal that the excitation intensity increases with $L1' = f_{\text{asp}} - L1$, as the LED is moved away from aspheric lens along the optical axis, to a maximum value at $L1' = -3.0$ mm. In order to get more accurate measurements and to compare our results directly with previously developed LED-based microendoscope systems, we used the Sumitomo IGN-08/30 fiber bundle (outer diameter 950 μm , active diameter 790 μm) that has $\sim 30,000$ individual fibers. The maximum power at the distal end of this fiber bundle was measured to be 1.7 mW at $L1' = -3.0$ mm.

We also used our model to predict the output intensity of the smaller fiber bundle (O.D. 680 μm) as a function of the parameters $L1'$ and $L2$, resulting in the family of curves shown in **Fig. 2.3**. Each curve represents the simulated output as a function of $L1'$, given a fixed distance $L2$ between the asphere and the objective. The results are shown for values of $L2$ that range between 20 and 80 mm in increments of 10 mm. The model predicts that a maximum power of 0.9 mW can be transmitted to the distal end of the fiber bundle with $L2 = 40$ mm. However, due to the size of the dichroic mirror located in between the aspheric and objective lenses, the minimum distance in our system is $L2 = 80$ mm. From the simulation we found that a maximum power of 0.76 mW can be delivered with this parameter. We experimentally measured a value of 0.70 mW. The small difference between this

result and our model can be explained by the presence of aberrations in the optical train.

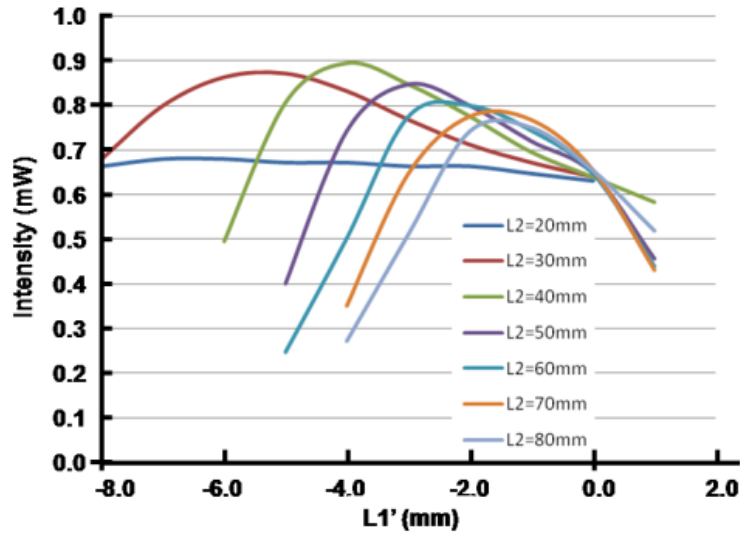


Fig. 2.3. Simulated fiber bundle power throughput. Dependence of the output intensity on $L1'$ and $L2$ from our model is shown. Maximum power of 0.9 mW can be transmitted with $L2 = 40$ mm, but size constraints require $L2 = 80$ mm for maximum simulated power of 0.76 mW.

2.3.3 *In vitro* validation of fluorescence imaging using microendoscope

Images of HeyA8-GFP cells in culture collected with a bench-top epifluorescence microscope and with the microendoscope are shown in **Fig. 2.4a** and **b**, respectively, and demonstrate that the morphology of the single cells imaged is similar. The average target-to-background ratios for the images collected with the epifluorescence microscope and the microendoscope were found to be 6.1 ± 2.4 and 6.9 ± 1.7 , respectively. The average SNR were found to be 41.8 ± 14.7 and 5.9 ± 1.0 , respectively. As the image of the fiber bundle face on the CCD array after relay magnification is $44 \mu\text{m}$, and the CCD pixels are square with a dimension of $6.45 \mu\text{m}$, the SNR of the microendoscope can be increased by binning image pixels 2×2 without loss of resolution.

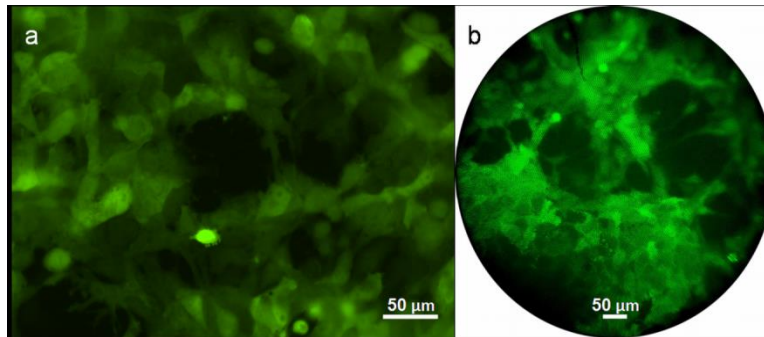


Fig. 2.4. *In vitro* imaging of cells. Fluorescence images of HeyA8-GFP cells in culture collected with an (a) epifluorescence microscope and the (b) microendoscope reveal similar GFP fluorescence patterns constitutively expressed by the cells.

2.3.4 Longitudinal *in vivo* imaging of tumor xenografts in mice

No external signs of the tumor could be seen or palpated at 1 week after implantation, and single cells (arrow) could be visualized on imaging (**Fig. 2.5a**). Small masses (1 to 3 mm) were externally visible and palpable at 2 weeks, and small clusters of cells could be visualized (**Fig. 2.5b**). The mice exhibited large (>4 mm) tumors and showed evidence of weight loss at 3 weeks, and single cells could be resolved on the surface of the bulk tumor masses (**Fig. 2.5c**). Small clusters of cells were still detectable 4 weeks after implantation. Also, by inserting the microendoscope through the needle into a tumor, single cells within the mass could be visualized. Microvasculature (arrow) could also be visualized below the surface of the tumors at week 4 (**Fig. 2.5d**). After the third week, 3 of the 10 mice were euthanized due to tumor burden. The remaining 7 mice were imaged again at 4 weeks, and did not reveal additional changes in tumor morphology or distribution. All mice were euthanized after the final imaging session in week 4 due to tumor burden. Images from control mice showed minimal autofluorescence intensity, with a ratio of images in which the entire field-of-view is coated with tumor (such as the vasculature image in **Fig. 2.5d**) to control images of 4.1 ± 1.2 (data not shown).

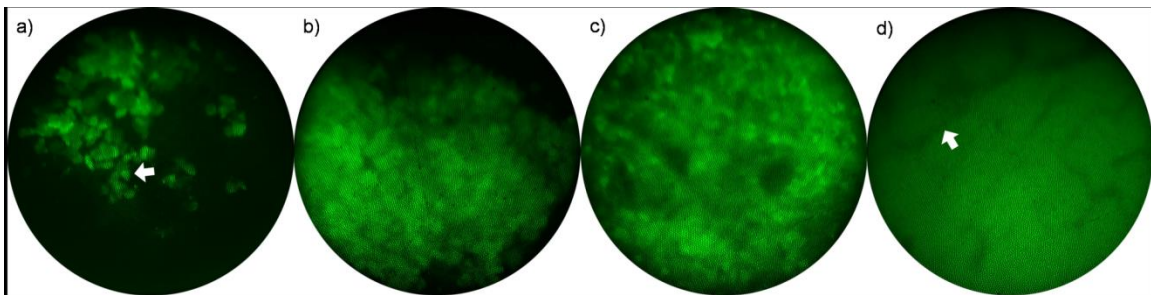


Fig. 2.5. *In vivo* imaging after implantation of HeyA8-GFP cells. a) Single cells (week 1). b) Small cluster of cells (week 2). c) Bulk tumor mass (week 3). d) Neovasculature detected as branching, non-fluorescent structures within a GFP-positive tumor (week 4).

2.4 Discussion

Here, we demonstrate a miniature fluorescence microscope that uses a LED source to collect images with sub-cellular resolution in real-time. The large divergence angle of the light source allows for all of the individual fibers of the bundle to be illuminated simultaneously, thus eliminating the need for a scanner. Not only is this system relatively inexpensive and easy to implement, the small size and fast frame rate that can be achieved are well-suited for high resolution imaging in small animals. The small size of the instrument allowed for repeated insertion into the peritoneum of living mice to study the progression of ovarian cancer cells over a period of 4 weeks. At that time, co-morbidities from the tumor rather than from the procedure resulted in termination of the study. Over this time course, we observed the following progression: 1) individual and small clusters of sporadic cells, 2) development of masses, and 3) emergence of tumor vasculature. The microendoscope could be inserted into the peritoneum and then removed without requiring sutures or clips to close the entry site.

Muldoon *et al.* demonstrated an LED-based microendoscope that used a fiber bundle with an outer diameter of 1.0 mm, and inserted it subcutaneously in mice in a terminal study [13]. The excitation power through this bundle was 1.0 mW. Zhong *et al.* built a system which delivered only 0.035 mW through a 1.0 mm outer diameter fiber bundle, necessitating use of a highly sensitive EMCCD to have sufficient sensitivity to detect fluorescence *in vivo* [15]. By comparison, our optical model helped us to achieve an output power of 1.7 mW through a bundle of comparable size, and allowed us to build an even smaller microendoscope with 0.680 mm diameter and output power 0.7 mW that can pass harmlessly into the peritoneum, while using a low-cost CCD camera. Once the microendoscope is inserted into this cavity, it can be moved freely by hand to any location within this space. We also achieved high SNR at a fast frame rate of 10 Hz. This image acquisition speed is critical to minimize motion artifact, which is exaggerated in

small animals due to their higher respiratory rate and larger relative lung displacement.

Although the system presented here was demonstrated in small animals, the same instrument can also be applied in the clinic. Colon, esophagus, and lung have been imaged extensively using commercialized fibered confocal endoscopes, however deep tissues inaccessible to endoscopes have not been studied. A fibered micro-laparoscope has been recently developed and used to image human ovaries [19,20], but the procedure is invasive compared to endoscopy. Our microendoscope can enter the cannula of a 19G needle and could potentially enter deep tissues in humans with less invasiveness than laparoscopy, potentially leading to molecular analysis of human cancers *in situ*.

In order to reduce trauma to the animals for *in vivo* imaging, we minimized the outer diameter of the instrument by not adding an objective lens to the distal end of the fiber bundle. In our application, the absence of an objective lens does not limit our ability to image deep tissue structures throughout the peritoneum. However, this design does result in a sacrifice in both lateral and axial resolution compared to that of commercial systems. Additionally, without a lens to protect the fiber bundle, the distal fiber face must be polished frequently to remove scratches. Finally, a limitation of all fiber bundle instruments is the appearance of pixilation artifact from the bundle geometry, which can be minimized by image processing techniques [11].

While imaging the same group of cells on serial sessions would be difficult, longitudinal studies can be performed by collecting representative images and drawing conclusions using statistical arguments, tracking measures such as mean fluorescence intensity or the average number of cells within the field-of-view. Moreover, histologic confirmation can be performed after euthanasia of the animal. The ability to conduct longitudinal imaging studies at the cellular level in small animals has important implications for translational research. Molecular changes are expressed in transformed cells well in advance of morphological differences, and

produce targets that reveal biological function. While we used cells engineered to express GFP constitutively to demonstrate the proof-of-concept, resolution of this system is sufficient to detect changes in sub-cellular localization or expression of fluorescent reporter proteins. Since functions of many signaling molecules in ovarian cancer and other malignancies are regulated by changes in subcellular compartmentalization, this imaging technology will enable single cell analysis of signal transduction and inhibition with chemotherapeutic agents. Molecular targets in ovarian cancer or other diseases also can be detected with imaging probes, including monoclonal antibodies, peptides, and small molecules [21-24]. The small size of this instrument allows for minimally-invasive detection of molecular changes in progression of cancer and intercellular variations in signal transduction that may regulate susceptibility versus resistance to therapy. Moreover, the imaging bundle can accommodate a wide variety of LED sources, ranging in color from blue ($\lambda = 455$ nm) to red ($\lambda = 630$ nm). The flexibility to accommodate different colors of LED sources opens the opportunity to perform multi-spectral imaging of multiple molecular targets in real time *in vivo*.

In conclusion, we have developed a miniature confocal microendoscope based on a LED source and a flexible fiber to collect fluorescence images with sub-cellular resolution and perform longitudinal studies of tumor progression in living mice.

References

1. Luker, G.D.; Luker, K.E. Optical imaging: current applications and future directions. *J. Nucl. Med.* 49: 1-4, 2008.
2. Choy G.; Choyke P.; Libutti, S.K. Current advances in molecular imaging: noninvasive *in vivo* bioluminescent and fluorescent optical imaging in cancer research. *Mol. Imaging.* 2: 303-312, 2003.
3. Lu, S.; Lowe, A.W.; Triadafilopoulos, G.; Hsiung, P.L.; Hao, Y.; Crawford, J.M.; Wang, T.D. Endoscopic evaluation of esophago-gastro-jejunostomy in rat model of Barrett's esophagus. *Dis. Esophagus* 22: 323-330, 2009.
4. Skala, M.C.; Fontanella, A.; Lan, L.; Izatt, J.A.; Dewhirst, M.W. Longitudinal optical imaging of tumor metabolism and hemodynamics. *J. Biomed. Opt.* 15: 011112, 2010.

5. Sumen, C.; Mempel, T.R.; Mazo, I.B.; von Andrian, U.H. Intravital microscopy: visualizing immunity in context. *Immunity* 21: 315-329, 2004.
6. Cahalan, M.D.; Parker, I. Choreography of cell motility and interaction dynamics imaged by two-photon microscopy in lymphoid organs. *Annu. Rev. Immunol.* 26: 585-626, 2008.
7. R. Kiesslich, J. Burg, M. Vieth, J. Gnaendiger, M. Enders, P. Delaney, A. Polglase, W. McLaren, D. Janell, S. Thomas, B. Nafe, P.R. Galle, M.F. Neurath, "Confocal Laser Endoscopy for Diagnosing Intraepithelial Neoplasias and Colorectal Cancer *In Vivo*," *Gastroenterology*, 127, 706-713 (2004).
8. T.D. Wang, S. Friedland, P. Sahbaie, R. Soetikno, P.L. Hsiung, J.T.C. Liu, J.M. Crawford, C.H. Contag, "Functional imaging of colonic mucosa with a fibered confocal microscope for real-time *in vivo* pathology," *Clin. Gastroent. and Hep.*, 5, 1300-1305 (2007).
9. L. Thiberville, S. Moreno-Swirc, T. Vercauteren, E. Peltier, C. Cavé, G.B. Heckly, "*In vivo* imaging of the bronchial wall microstructure using fibered confocal fluorescence microscopy," *American Journal of Respiratory and Critical Care Medicine*, 175, 22-31 (2007).
10. M. Goetz, C. Fottner, E. Schirmacher, P. Delaney, S. Gregor, C. Schneider, D. Strand, S. Kanzler, B. Memadathil, E. Weyand, M. Holtmann, R. Schirmacher, M.M. Weber, M. Anlauf, G. Kloppel, M. Vieth, P.R. Galle, P. Bartenstein, M.F. Neurath, R. Kiesslich, "In-vivo confocal real-time mini-microscopy in animal models of human inflammatory and neoplastic diseases," *Endoscopy* 39, 350-356, (2007).
11. E. Laemmel, M. Genet, G. Le Goualher, A. Perchant, J.F. Le Gargasson, E. Vicaut, "Fibered Confocal Fluorescence Microscopy (Cell-viZio™) Facilitates Extended Imaging in the Field of Microcirculation," *Journal of Vascular Research*, 41, 400-11, (2004).
12. M.A. D'Hallewin, S. El Khatib, A. Leroux, L. Bezdetsnaya, F. Guillemin, "Endoscopic confocal Fluorescence Microscopy of Normal and Tumor Bearing Rat Bladder," *J of Urology*, 174, 736-740, (2005).
13. Muldoon, T.J.; Pierce, M.C.; Nida, D.L.; Williams, M.D.; Gillenwater, A.; Richards-Kortum, R. Subcellular-resolution molecular imaging within living tissue by fiber microendoscopy. *Optics Express* 15: 16413-16423, 2007.
14. Muldoon, T.J.; Anandasabapathy, S.; Maru, D.; Richards-Kortum, R. High-resolution imaging in Barrett's esophagus: a novel, low-cost endoscopic microscope. *Gastrointestinal Endoscopy* 68: 737-744, 2008.
15. Zhong, W.; Celli, J.P.; Rizvi, I.; et al. *In vivo* high-resolution fluorescence microendoscopy for ovarian cancer detection and treatment monitoring. *Br. J. Cancer* 101: 2015-2022, 2009.
16. Philips Lumileds Lighting Company. Technical Datasheet DS51. <http://www.philipslumileds.com>.
17. Lois, C.; Hong, E.J.; Pease, S.; Brown, E.J.; Baltimore, D. Germline transmission and tissue-specific expression of transgenes delivered by lentiviral vectors. *Science* 295: 868-872, 2002.

18. Dittgen, T.; Nimmerjahn, A; Komai, S.; et al. Lentivirus-based genetic manipulations of cortical neurons and their optical and electrophysiological monitoring *in vivo*. Proc. Natl. Acad. Sci. U.S.A. 101:18206-18211, 2004.
19. A. Tanbakuchi, A. Rouse, J. Udovich, K. Hatch, A. Gmitro, "Clinical confocal microlaparoscope for real-time *in vivo* optical biopsies," Journal of Biomedical Optics, 14(4), 044030, (2009).
20. A. Tanbakuchi, J. Udovich, A. Rouse, K. Hatch, A. Gmitro, "*In vivo* imaging of ovarian tissue using a novel confocal microlaparoscope," Am J Obstet Gynecol, 202(90), e1-e9, (2010).
21. Goetz, M; Ziebart, A.; Foersch, S.; et al. *In vivo* molecular imaging of colorectal cancer with confocal endomicroscopy by targeting epidermal growth factor receptor. Gastroenterology 138: 435-446, 2010.
22. Hsiung, P.L.; Hardy, J.; Friedland, S.; et al. Detection of colonic dysplasia *in vivo* using a targeted heptapeptide and confocal microendoscopy. Nature Med. 14: 454-458, 2008.
23. Urano, Y.; Asanuma, D.; Hama, Y.; et al. Selective molecular imaging of viable cancer cells with pH-activatable fluorescence probes. Nature Med. 15: 104-109, 2009.
24. Goetz, M.; Wang, T.D.; Molecular imaging in gastrointestinal endoscopy. Gastroenterology 138: 828-33, 2010.

Chapter 3.

Targeted Imaging of Colorectal Dysplasia in Living Mice using Fluorescence Microendoscopy

3.1 Introduction

Although use of colonoscopy for early detection of colorectal cancer has led to a decreased incidence over the past two decades, this disease is still one of the most common cancers in the U.S. [1]. Traditional white-light endoscopy relies on gross architectural changes and is not sensitive to molecular changes that develop as normal colonic epithelium transforms into a pre-malignant condition (dysplasia) prior to evolving into adenocarcinoma [2]. Furthermore, white-light endoscopy cannot distinguish between dysplasia and hyperplasia, a benign epithelial proliferation. Intravital microscopes can be used to validate the unique expression pattern of molecular targets in diseased tissues with use of highly specific exogenous probes [3-4]. Additionally, these probes can be used to guide therapy [5], stratify risk, and localize margins, aiding the clinician's decision-making ability on a patient-to-patient basis [6].

Genetically engineered small animal models can be used to study the molecular progression of cancer that develops spontaneously over time [7]. While non-invasive techniques such as PET, bioluminescence, and MRI can serially image an animal, they cannot provide cellular detail in real time due to limitations in spatial resolution [8]. On the other hand, conventional intravital microscopes can achieve sub-cellular resolution, but their large dimensions in general require either an invasive incision or use of optical windows, limiting serial studies or working distance, respectively [9]. We have recently demonstrated a miniature microendoscope that can directly and repetitively image the epithelium of deep tissues with sub-cellular resolution in living mice [10].

Our laboratory has previously discovered a fluorescent peptide probe that specifically binds to murine colorectal dysplasia. This peptide (QPIHPNNM) was FITC-tagged and used to localize colonic dysplasia *in vivo* on wide-field fluorescence endoscopy [11]. Here, we aim to demonstrate the use of microendoscopy to validate selective binding by this peptide on a sub-cellular scale. This microendoscope is sufficiently small to pass through the instrument channel of the endoscope for direct placement onto the mucosal surface. Its fast frame rate can overcome motion artifact from the live animal introduced by organ peristalsis, heart beating, and breathing. We use this instrument to validate specific binding activity of QPIHPNNM to dysplasia in comparison to adjacent normal mucosa and to hyperplasia. Additionally, we validate the *in vivo* images with conventional confocal images collected with a bench top instrument. This study demonstrates a rigorous methodology for the validation of novel molecular probes being developed as a targeting agent for disease in hollow organs.

3.2 Methods

3.2.1 Design of fluorescence microendoscope for small animal colonoscopy

A schematic of the imaging system is shown in **Fig. 3.1**. A diode pumped solid state laser (CNI MBL-III-473, Changchun, China) produces emission centered at 473 nm. The power is adjusted to achieve 1 mW at the distal end of the microendoscope. The beam is collimated by an aspheric lens (L1, $f = 18$ mm), reflected by a 495 nm dichroic beamsplitter (Semrock FF495-Di02-25x36), and focused into a coherent fiber bundle (Sumitomo IGN-06/17, Osaka, Japan) by an infinity corrected objective lens (Olympus UIS2 PLN 20X, Tokyo, Japan). The bundle has $\sim 17,000$ fibers with core-to-core spacing of ~ 4 μm . The fluorescence image is magnified by the objective, passes through the dichroic, and is focused by a condenser lens (L2, $f = 100$ mm) onto a CCD camera (Hamamatsu Orca R2, Hamamatsu City, Japan). A 500 nm long-pass filter (LPF, Semrock BLP01-488R-25) blocks the reflected excitation light.

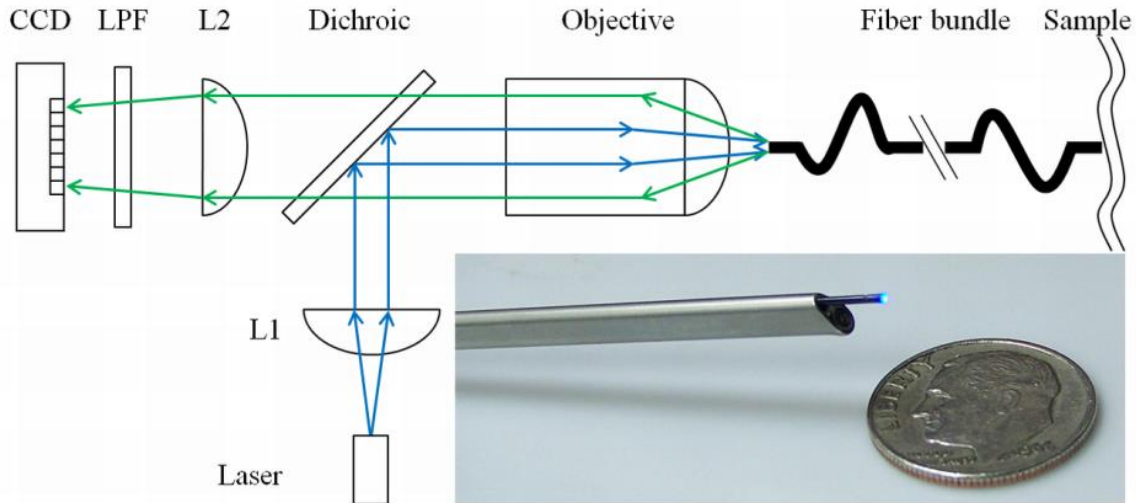


Fig. 3.1. Small animal fluorescence microendoscope design schematic. Excitation from the laser diode at 473 nm is collimated by an asphere (L1), reflected by a dichroic beamsplitter, and focused into a 680 μm (O.D.) coherent fiber bundle. Fluorescence is transmitted to the CCD. The bundle is sufficiently small in dimension to pass through the instrument channel of a small animal endoscope (inset).

The 680 μm outer diameter fiber bundle is sufficiently small to pass through the 3 Fr (~ 1 mm diameter) instrument channel of the rigid endoscope (Karl Storz, Tuttlingen, Germany) (**Fig. 3.1**, inset). This endoscope has outer dimensions of 2.7 mm x 3.5 mm, and is used to localize the adenomas with white light illumination [12]. The instrument channel is also used to administer the peptides and to provide insufflation to distend the lumen of the colon for imaging.

3.2.2 Animal models

All animal experiments were approved by the University of Michigan Committee for Use and Care of Animals (UCUCA). We used the CPC;*Apc* mouse model of spontaneous colorectal dysplasia, developed by Hinoi et al [13], to validate the peptide probe. *APC* is a tumor suppressor gene that is mutated in over 75% in human colorectal tumors [14]. In this mouse, the *Apc* gene locus is deleted by a *Cre* recombinase, resulting in the development of adenomas in the distal colon and rectum beginning at 10 weeks of age. *Cre*(+) mice develop adenomas; *Cre*(-) mice

and the *Kras* mouse model of colorectal hyperplasia are used as controls [15]. The CPC;Apc mice ranged in age from 5 to 6 months, and the *Kras* mice from 1 to 2 months.

3.2.3 *In vivo* microendoscopy

The target (QPIHPNNM) and control (GGGAGGGA) peptides were synthesized with Fmoc chemistry, conjugated with 5'-fluorescein isothiocyanate (FITC) via amino hexanoic acid linker, and purified with HPLC, as previously described [11]. These peptides were diluted to 100 μ M in 1X phosphate buffered saline (PBS). Mice were placed prone and anesthetized with isoflurane. After rinsing the colon with water to remove debris and mucous, approximately 1 mL of the peptide solution was administered intra-luminally to the mucosa. The peptide was allowed to incubate for 5 minutes, and subsequently, the unbound peptide was rinsed 3X with water. The endoscope was used to localize adenomas with white light illumination. The microendoscope was then passed through the instrument channel, and the distal end was positioned for complete contact with the mucosal surface. The white light source was turned off, and fluorescence images were collected with an exposure of 100 ms (frame rate of 10 Hz). All microendoscopy images are presented as single frames extracted from video recordings.

The target and control peptides are individually applied to the mucosa of *Cre*(+) mice (n = 6 and n = 4, respectively). Microendoscopic images were acquired from the surface of the one adenoma and the adjacent normal-appearing mucosa in each mouse. The specificity of QPIHPNNM for dysplasia was further validated by applying the peptide to normal mucosa of *Cre*(-) mice (n = 1) that do not develop adenomas, and to hyperplastic mucosa of *Kras* mice (n = 2). Autofluorescence images were taken from *Cre*(+) mice (n = 1) and *Kras* mice (n = 2) for purposes of comparison.

3.2.4 *Ex vivo confocal microscopy*

To validate the *in vivo* images collected with the microendoscope, we collected fluorescence images from freshly excised tissues with a bench top confocal microscope (Olympus FluoView 500, Tokyo, Japan). The mice were euthanized, and a pair of adenomas were excised (n = 3 mice, n = 5 adenoma pairs) from each mouse. Adenomas were incubated in 100 μ M solution of either QPIHPNNM or GGGAGGGA for 5 minutes, and then rinsed 3X with PBS. The adenomas were then placed with the mucosal surface facing the objective lens and imaged using 488 nm excitation.

3.2.5 *Data analysis*

Microendoscopic images were collected at 12-bit resolution (0 – 4095 AU). All images were acquired as videos of 2 second duration, and contained 21 frames. Criteria for frame selection include: 1) entire image being in focus (flat contact of microendoscope with the mucosal surface), and 2) no saturated pixels. The mean fluorescence intensity \pm one standard deviation error was then determined for each image. Those mean intensities were then averaged for all adenomas and normal tissues from each mouse. Additionally, we measured autofluorescence from the adenomas and hyperplastic mucosa. Statistical significance was determined by 2-sample t-test, $\alpha < 0.05$ (Minitab 16, State College, PA, USA).

The target-to-background ratios (T/B) of peptide binding to adenomas versus normal-appearing adjacent mucosa for each peptide were calculated by dividing the average mean intensity from adenomas by that from normal mucosa for each mouse. The results from all mice were then averaged to determine the overall T/B for each peptide.

3.3 Results

3.3.1 System design

The microendoscope achieves a field-of-view with a diameter of 540 μm and has a lateral resolution of 4 μm , verified by a standard (USAF) resolution target.

3.3.2 In vivo microendoscopy

The microendoscopy images revealed that the target peptide QPIHPNNM demonstrates greater binding to adenomas than to the normal-appearing surrounding mucosa, as demonstrated by the greater fluorescence intensity (**Fig. 3.2a-b**). In addition, the binding pattern reflects cellular features specific to the mucosal surface. In contrast, the control peptide (GGGAGGGA) shows minimal fluorescence and does not reveal cellular features for either dysplastic or normal mucosa (**Fig. 3.2c-d**). Furthermore, QPIHPNNM shows minimal fluorescence signal from the normal mucosa, demonstrating little non-specific binding (**Fig. 3.2e**). The autofluorescence signal from adenomas is also minimal (**Fig. 3.2f**). Fluorescence intensity from QPIHPNNM applied to the hyperplastic mucosa of the *Kras* mouse model (**Fig. 3.2g**) is comparable to the autofluorescence signal from the same tissue (**Fig. 3.2h**).

The mean fluorescence intensity from adenomas averaged across all mice, 773 ± 99 , is significantly higher than that from the normal-appearing surrounding mucosa, 384 ± 93 , ($p < 0.001$). The T/B of QPIHPNNM from adenomas to the adjacent normal mucosa, 2.11 ± 0.61 , is significantly higher than that of the control peptide GGGAGGGA, 1.16 ± 0.10 ($p = 0.016$) (**Fig. 3.3a**). The autofluorescence, measured from adenomas on the *Cre(+)* mice and hyperplasia on the *Kras* mice, are 297 ± 48 and 471 ± 36 , respectively. After subtraction of autofluorescence, the mean intensity from QPIHPNNM applied to adenomas, normal-surrounding mucosa of *Cre(+)* mice, hyperplasia, and normal mucosa of *Cre(-)* mice are 476 ± 110 , 87 ± 105 , 46 ± 64 , and 81 ± 62 , respectively (**Fig. 3b**), resulting in a T/B for dysplasia to normal (*Cre+*), hyperplasia, and normal (*Cre-*) of 5.5, 10.3, and 5.9, respectively.

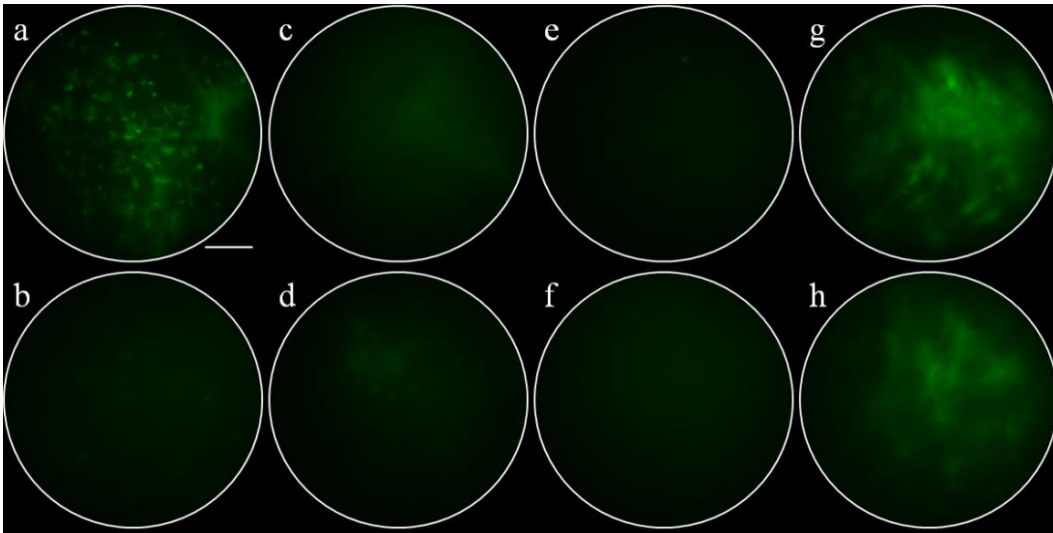


Fig. 3.2. *In vivo* microendoscopy images of murine colonic tissue. QPIHPNNM applied to the surface of a) an adenoma (Media 1) and b) normal-appearing adjacent mucosa. GGGAGGGA (control peptide) applied to the surface of c) an adenoma and d) normal-appearing adjacent mucosa. e) QPIHPNNM applied to normal colonic mucosa in *Cre(-)* mice. f) Autofluorescence from adenoma in *Cre(+)* mice. g) QPIHPNNM applied to hyperplastic mucosa of *Kras* mouse. h) Autofluorescence signal from *Kras* mouse. Scale bar = 100 μm .

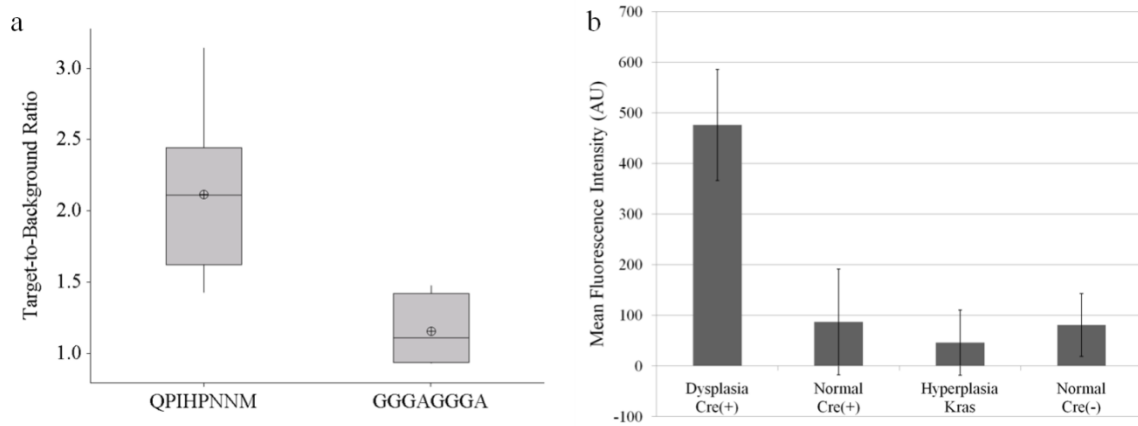


Fig. 3.3. Quantification of average fluorescence intensities. (a) Boxplot of T/B of peptides from adenomas to adjacent normal mucosa. T/B of QPIHPNNM is significantly higher than that of GGGAGGGA. Lower, middle, and top lines of boxes indicate lower quartile, median, and upper quartile, respectively. Whiskers indicate minima and maxima, and crosshairs indicate means. (b) Mean fluorescence intensity of QPIHPNNM, after autofluorescence subtraction. Fluorescence signal from dysplasia is at least five-fold greater than from all other tissues.

3.3.3 Comparison of *in vivo* microendoscopy to *ex vivo* confocal microscopy

Fluorescence images of freshly excised adenomas incubated with QPIHPNNM and GGGAGGGA collected with a bench top confocal microscope are shown in **Fig. 3.4**. The image of QPIHPNNM (**Fig. 4a**) demonstrates binding pattern of the target peptide to single epithelial cells, representing similar morphological features to that seen on microendoscopy. Comparatively, the *ex vivo* confocal microscopy (**Fig. 4b**) image shows minimal fluorescence signal and no resolvable cellular features using the GGGAGGGA (control) peptide. Hematoxylin and eosin stained biopsy specimens of adenomas reveal enlarged nuclei and distorted crypts characteristic of dysplasia (**Fig. 4c**), as previously shown [11].

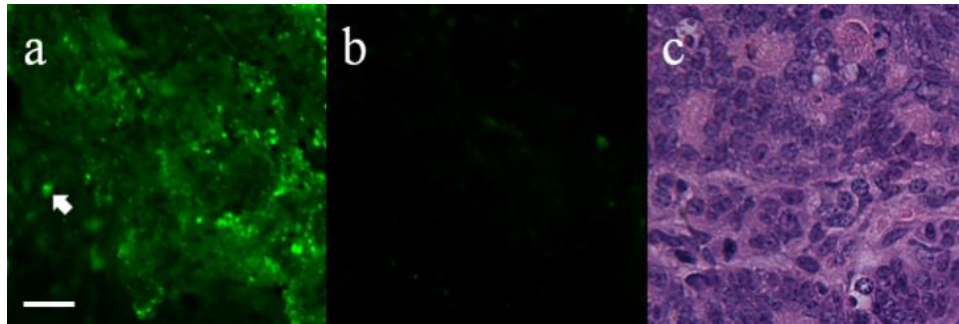


Fig. 3.4. Confocal microscopy images of excised colonic adenomas. (a) QPIHPNNM shows binding to single epithelial cells (arrow). (b) Minimal binding was revealed on using the GGGAGGGA peptide. (c) Histology confirms dysplastic crypts in adenoma biopsy specimens. Scale bar = 20 μm .

3.4 Discussion

Here, we demonstrate a methodology for validation of selective binding of a fluorescence-labeled peptide to colonic dysplasia with sub-cellular resolution in living mice using a microendoscope. The experiments confirm specific binding activity of the target peptide (QPIHPNNM) to dysplasia in comparison to hyperplastic and normal colonic mucosa and to the control peptide (GGGAGGGA) on a microscopic scale. The T/B of both the target and control peptides for adenomas and to adjacent normal mucosa on microendoscopy, shown in Fig. 3a, are consistent with those found for the same peptides on wide-field fluorescence endoscopy [11].

This result is expected because the microendoscope images the mucosal surface, as does the wide-field fluorescence endoscope. Moreover, The T/B of the target peptide improves with subtraction of mucosal autofluorescence. This integrated strategy combines the use of a wide-area endoscope to guide placement of the microendoscope to achieve both a large field of view for localization and sub-cellular resolution for validation in real time.

In addition, a comparison of the microendoscope to bench top confocal images of peptide binding to adenomas reveals similar spatial patterns. This result demonstrates the ability of the microendoscope to acquire sub-cellular images in living mice, in real time, allowing for the study of molecular expression patterns of pre-malignant epithelial cells *in vivo*, using each animal as its own control. This enabling technology can greatly reduce the number, hence cost, of animals needed to perform validation studies with robust statistics. In addition, the process of euthanizing animals and excising tissue may introduce artifacts in the data. Given the time needed to dissect the animal, resect the specimen, and bring the tissue to the microscope, the fluorescent probes may undergo enzymatic degradation or photobleaching, and the cells may undergo apoptosis or desiccation. Moreover, surgical incisions may introduce trauma, hypoxia, and bleeding that can alter the molecular expression patterns.

These results demonstrate a rigorous methodology for multi-scale validation of a novel targeting agent being developed to localize disease that can be generalized to hollow organs.

References

1. American Cancer Society, "Cancer Facts & Figures 2010," (American Cancer Society, Atlanta, Ga., 2010).
2. R.S. Cotran, Robbins and Cotran Pathologic Basis of Disease, 7th ed., V. Kumar, A.K. Abbas, N. Fausto, ed. (Saunders, Philadelphia, Pa., 2005).
3. M. Goetz, A. Ziebart, S. Foersch, M. Vieth, M.J. Waldner, P. Delaney, P.R. Galle, M.F. Neurath, R. Kiesslich, "In Vivo Molecular Imaging of Colorectal Cancer with Confocal Microendoscopy by Targeting Epidermal Growth Factor Receptor," *Gastroenterology* 138, 435-446 (2010).

4. P.L. Hsiung, J. Hardy, S. Friedland, R. Soetikno, C.B. Du, A.P. Wu, P. Sahbaie, J.M. Crawford, A.W. Lowe, C.H. Contag, T.D. Wang, "Detection of colonic dysplasia *in vivo* using a targeted heptapeptide and confocal microendoscopy," *Nat. Med.* 14, 454-458 (2008).
5. F. Ciardiello and G. Tortora, "EGFR Antagonists in Cancer Treatment," *New Engl. J. Med.* 358, 1160-1174 (2008).
6. W. De Roock, B. Biesmans, J.D. Schutter, S. Tejpar, "Clinical Biomarkers in Oncology: Focus on Colorectal Cancer," *Mol. Diag. Ther.* 13, 103-114 (2009).
7. N.E. Sharpless and R.A. DePinho, "Model organisms: The mighty mouse: genetically engineered mouse models in cancer drug development," *Nat. Rev. Drug Discov.* 5, 741-754 (2006).
8. G.S. Sandhu, L. Solorio, A.-M. Broome, N. Salem, J. Kolthammer, T. Shah, C. Flask, J.L. Duerk, "Whole animal imaging," *Wiley Interdisciplinary Reviews: Systems Biol. and Med.* 2, 398-421 (2010).
9. M. Goetz, C. Fottner, E. Schirmacher, P. Delaney, S. Gregor, C. Schneider, D. Strand, S. Kanzler, B. Memadathil, E. Weyand, M. Holtmann, R. Schirmacher, M.M. Weber, M. Anlauf, G. Klöppel, M. Vieth, P.R. Galle, P. Bartenstein, M.F. Neurath, R. Kiesslich, "In-vivo confocal real-time mini-microscopy in animal models of human inflammatory and neoplastic diseases," *Endoscopy* 39, 350-356 (2007).
10. S.F. Elahi, Z. Liu, K.E. Luker, R.S. Kwon, G.D. Luker, T.D. Wang, "Longitudinal Molecular Imaging with Single Cell Resolution of Disseminated Ovarian Cancer in Mice with a LED-based Confocal Microendoscope," *Mol. Imaging Biol.*, DOI: 10.1007/s11307-010-0455-1.
11. S.J. Miller, B. Joshi, A. Gaustad, E.R. Fearon, T.D. Wang, "*In vivo* Fluorescence-Based Endoscopic Detection of Colon Dysplasia in the Mouse using a Novel Peptide Probe," *PLoS ONE* 6, e17384 (2011).
12. C. Becker, M.C. Fantini, M.F. Neurath, "High resolution colonoscopy in live mice," *Nature Protoc.* 1, 2900-2904 (2006).
13. T. Hinoi, A. Akyol, B.K. Theisen, D.O. Ferguson, J.K. Greenson, B.O. Williams, K.R. Cho, E.R. Fearon, "Mouse Model of Colonic Adenoma-Carcinoma Progression Based on Somatic Apc Inactivation," *Cancer Res.* 67, 9721-9730 (2007).
14. C.N. Arnold, A. Goel, H.E. Blum, C.R. Boland, "Molecular pathogenesis of colorectal cancer," *Cancer* 104, 2035-2047 (2005).
15. P. Trobridge, S. Knoblauch, M.K. Washington, N.M. Munoz, K.D. Tsuchiya, A. Rojas, X. Song, C.M. Ulrich, T. Sasazuki, S. Shirasawa, W.M. Grady, "TGF- β Receptor Inactivation and Mutant Kras Induce Intestinal Neoplasms in Mice via a β -Catenin Independent Pathway," *Gastroenterology* 136, 1680-1688 (2009).

Chapter 4.

Noninvasive Optical Assessment of Implanted Engineered Tissues Correlates with Pre-Implantation Cytokine Secretion

4.1 Introduction

The fields of tissue engineering and regenerative medicine (TERM) are at a stage where scientific advances are rapidly transitioning to clinical applications [1]. Compliance with regulatory oversight procedures established by government agencies is critical to ensure product safety and efficacy. The U.S. Food and Drug Administration (FDA) specifically noted that a key hurdle to translation of TERM products is the difficulty in characterizing the product to enable development of meaningful quality controls [2]. Further, a 2012 survey of investment organizations found that the top two perceived barriers to investing in TERM technologies are regulatory pathway clarity and clinical validation [3]. Therefore, clinical translation in TERM requires evaluative tools to assess engineered tissue products and ensure manufacturing consistency (before implantation) and validate clinical efficacy (after implantation) [4]. Here, we focus on combination tissue-engineered constructs comprised of an acellular dermal extracellular matrix and an engineered cultured living epithelial cell layer, commonly used for skin [5,6] and oral mucosa [7] applications.

The evaluative tools must assess tissue construct viability quantitatively and noninvasively. This is achievable for pre-implantation assessment by measuring the release of constitutively produced cytokines in the spent culture medium. Certain growth factors and cytokines regulate wound healing [8,9]. A mechanism by which tissue engineered constructs promote integration is to supply these cytokines to the surrounding native tissue [10]. The cytokine release level measured during the construct manufacturing process correlates to the number of viable functional cells

in the living cell layer [11], which therefore assists in predicting *in vivo* tissue integration [12]. However, current practices for post-implantation assessment are either qualitative (visual assessment) or destructive (histology). There is an unmet clinical need for a quantitative and noninvasive methodology for evaluating the integration of engineered tissue with native tissue.

Optical techniques including fluorescence spectroscopy [13-15], optical coherence tomography [16,17], laser speckle imaging [18], and Raman spectroscopy [19] offer the potential to quantitatively and noninvasively assess engineered tissues in real time during the *in vivo* tissue integration process [20]. Of these, fluorescence spectroscopy can sense endogenous reporters of cellular metabolism, enabling label-free assessment of construct viability [21,22]. Using multiphoton microscopy, our group has recently demonstrated that fluorescence lifetime parameters—time-resolved spectral measurements [23-26]—can indicate local cellular viability of tissue-engineered constructs *in vitro* [27]. That study motivated us to implement fluorescence lifetime spectroscopy (FLS) *in vivo* to interrogate tissue-engineered constructs implanted in a murine model. Here, we employed handheld, fiber-optic based fluorescence lifetime spectroscopy (FLS) instrumentation. Fiber-optic FLS has been previously demonstrated as a quantitative approach for noninvasive optical characterization of biological tissues [28-31], including by our group [32-34].

Our model system is *Ex Vivo* Produced Oral Mucosa Equivalent (EVPOME), a cell-based device manufactured from primary human oral keratinocytes [35-41]. The instrumentation was designed to be suitable for intravital measurements: rapid data acquisition, portability, precise maneuverability, and localization at multiple sites per construct. Quantitative data analysis methods were developed to assess the health of the implanted constructs *in vivo*. We found that optical parameters measured *in vivo* 1 week after implantation correlated with concentrations of cytokines secreted by the constructs prior to implantation, and that this correlation was not present at 3 weeks after implantation, when histology showed that

constructs had integrated with the native tissue. This study demonstrates that clinical optical diagnostic tools based on fluorescence lifetime sensing are promising to monitor the integration of tissue-engineered constructs, an unmet clinical need.

4.2 Methods

4.2.1 Manufacturing of EVPOME Human Keratinocyte-Based Tissue Engineered Constructs

The clinical study protocol was approved by the University of Michigan (UM) Medical School Institutional Review Board. Discarded, surgically-resected oral mucosa samples were obtained from patients undergoing minor oral surgical procedures. All study practices were in accordance with the Declarations of Helsinki Guidelines.

The detailed protocols for culturing human oral keratinocytes and manufacturing EVPOME have been previously published [35,36]. Briefly, primary human oral keratinocytes were enzymatically dissociated from the tissue samples. Isolated cell cultures were established in a chemically-defined, serum-free culture medium (EpiLife and EDGS, Invitrogen/Life Sciences) containing 0.06 mM calcium, 25 µg/mL gentamicin, and 0.375 µg/mL fungizone (Sigma). After harvesting, cells were cryopreserved until needed for EVPOME manufacturing. Prior to EVPOME manufacturing, the frozen keratinocytes were thawed and passaged up to two times. 2×10^5 cells were seeded onto a 1 cm² acellular cadaver dermis (AlloDerm®, LifeCell), hereafter referred to as the dermal equivalent, pre-coated with type IV collagen (Sigma) to promote cell attachment. The seeded EVPOME was immersed for 4 days in a culture medium containing 1.2 mM calcium to promote cell proliferation. The EVPOME was then raised to an air-liquid interface for an additional 7 days to enhance stratification of the epithelial layer. This 11 day culture protocol was chosen because EVPOMEs cultured at an air-liquid interface for 7 days are at the optimal stage of development for *in vivo* grafting [37].

To create a range of pre-implantation health states, half of the EVPOMEs were manufactured according to standard protocol (control) and the other half was thermally stressed to reduce cell viability and proliferation capabilities (stressed). Control EVPOMEs were incubated at 37°C with 5% CO₂ for all culture days. The incubation temperature of the stressed EVPOMEs was increased to 43°C on Day 9 for 24 hours and then returned to 37°C [19,27].

4.2.2 *Pre-Implantation Assessment of Construct Health by Biochemical Assay and Histology*

To quantitatively assess the pre-implantation health of the constructs, cytokine concentrations in the culture medium were measured by biochemical assay on the day of implantation (Day 11). The three cytokines of interest were interleukin-8 (IL-8), human β -defensin 1 (hBD-1), and vascular endothelial growth factor (VEGF). These were selected because they are constitutively secreted by oral keratinocytes and play an important role in tissue integration (IL-8 and VEGF) and function (hBD-1). IL-8 enhances wound healing by promoting re-epithelialization by inducing host keratinocyte migration and proliferation [42-44]. The antimicrobial peptide hBD-1 promotes differentiation by protecting keratinocytes from apoptosis [45-47]. VEGF induces angiogenesis *in vivo*, a critical factor in tissue integration [11,48].

Cytokine concentrations were measured by the microfluidic enzyme-linked immunosorbent assay (ELISA) kit Optimiser™ (Siloam Biosciences) according to the manufacturer's instructions. IL-8 and VEGF antibody pairs were obtained from LifeTechnologies and hBD-1 antibody pairs were obtained from Peprotech. IL-8 and hBD-8 samples needed to be 1:3 diluted by Optiblock™ buffer to reduce the concentration to the linear range of the calibration curve. To decrease the blank signal without compromising sensitivity, 10 μ L of wash and block buffer was used instead of 5 μ L. Since the VEGF assay was not sensitive enough to be detected by this procedure, 100 μ L of sample needed to be added to the plate in increments of 5 μ L, as suggested in the user manual.

Histological sections were also collected on Day 11 to directly observe the pre-implantation health of the constructs. Approximately one-fifth of the construct was cut, fixed in 10% formalin, washed with phosphate buffered saline, and stored in a 70% ethanol solution. Specimens were stained with hematoxylin and eosin, cut into 5 μ m sections, and preserved for future analysis.

4.2.3 *Experimental Study Design*

Primary human cells from 4 distinct patients were used in this study. **Fig. 4.1** depicts the experimental study design per patient. Harvested cells from each patient were used to manufacture EVPOMEs in two implantation cohorts. The two timelines correspond to the two cohorts: EVPOMEs to be implanted for 1 week or 3 weeks. Note that although the two timelines are depicted as aligned at Day 0, in fact, the cell seeding was staggered by two weeks so that *in vivo* measurements could be performed on the same day for both cohorts.

EVPOMEs in each cohort were split into stressed and control groups at Day 9 of the manufacturing protocol, each group containing duplicates. Therefore, 8 EVPOMEs were manufactured from each patient (2 cohorts per patient x 2 groups per cohort x 2 EVPOMEs per group = 8 EVPOMEs per patient). One exception was the 1-week cohort of patient #1, which contained triplicates instead of duplicates.

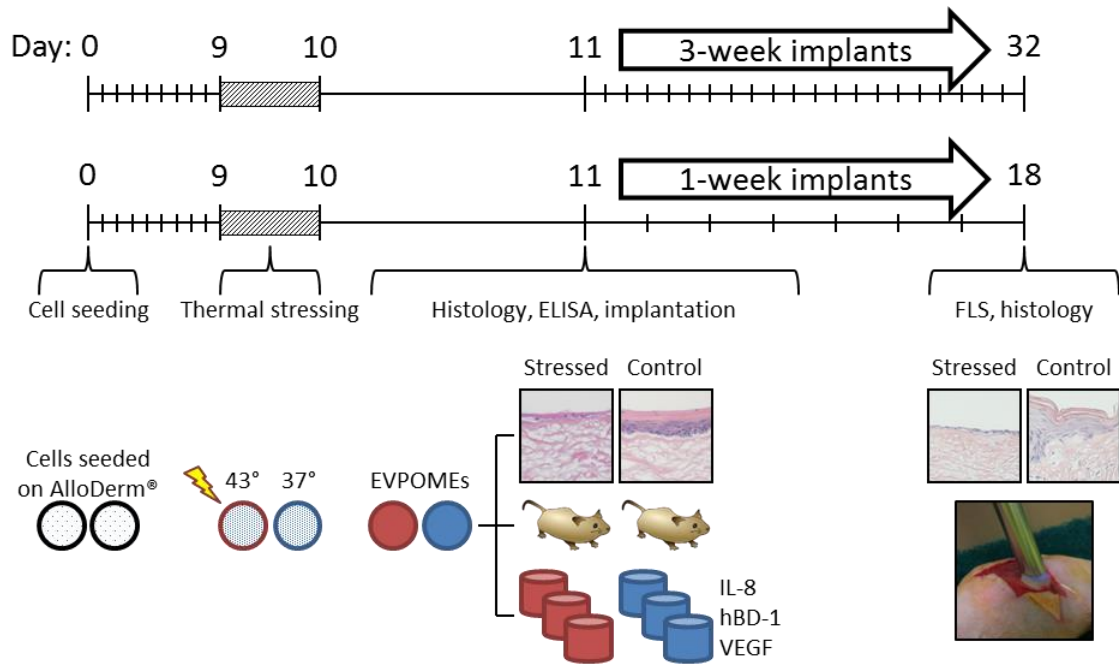


Fig. 4.1. Study design for each patient. Cells from one patient were seeded on AlloDerm® (Day 0) in two cohorts, one to be implanted in mice for 1 week, the other for 3 weeks. The incubation temperature of stressed constructs (red) was increased to 43°C, while control constructs (blue) were maintained at 37°C (Day 9-10). At day 11 for each construct, three aliquots of spent culture medium were collected for ELISA, one-fifth of the construct was cut for histology, and the remainder was implanted into a SCID mouse. Constructs were optically assessed by fluorescence lifetime spectroscopy (FLS) for both 1-week and 3-week post-implantation cohorts (Day 18 and 32). After optical assessment, the mice were sacrificed, and the construct processed for histology. Note that “Day 0” for 1-week and 3-week cohorts was staggered so that FLS measurements could be taken on the same day.

Two assessments were performed on Day 11 to characterize pre-implantation construct viability as described above: ELISA to measure cytokine secretion levels and histology to directly observe construct morphology. The EVPOME was then implanted into a mouse. Representative pre-implantation construct histology is shown in the left-most column of **Fig. 4.2**. Control constructs developed three characteristic layers: a top keratin layer, a middle living cell layer and a bottom dermal equivalent layer. Stressed constructs typically did not develop healthy cell layers.

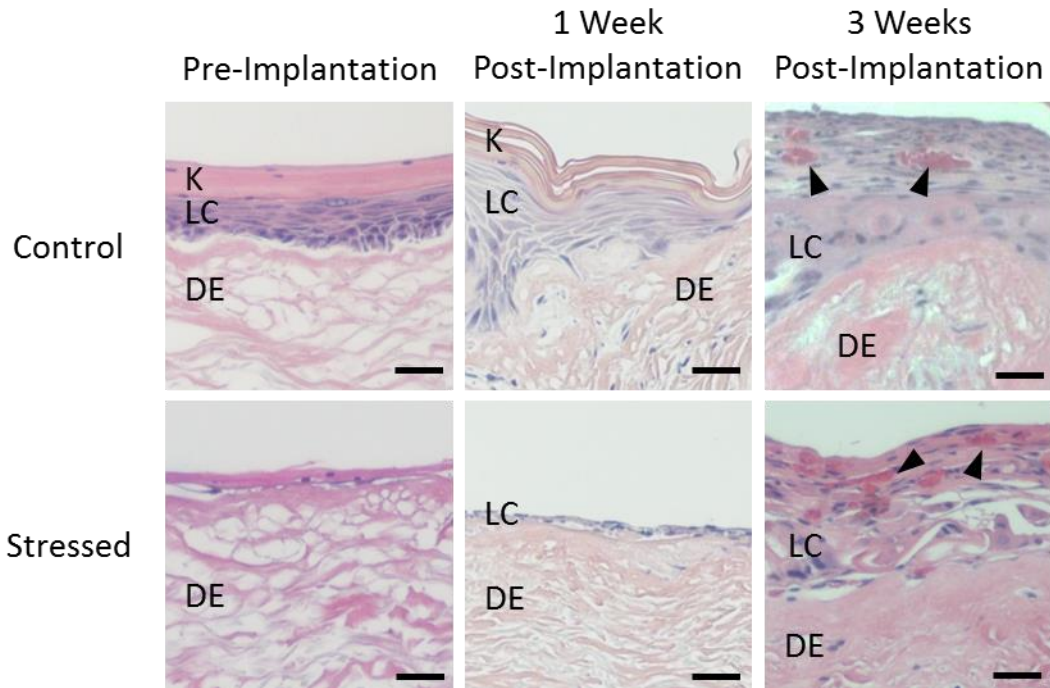


Fig. 4.2. Representative EVPOME histology. Control pre-implantation constructs developed three distinct layers: a top keratin layer (K), a middle living cell layer (LC), and a bottom dermal equivalent layer (DE). Stressed constructs did not develop a healthy cell layer pre-implantation. One week after implantation, cell layers in control constructs were thicker and more organized than those of stressed constructs. However, cell layers of both control and stressed groups were comparably healthy 3 weeks after implantation, consisting re-epithelialized cell layers and neovasculation (arrowheads). All scale bars are 50 μm .

The implanted EVPOMEs were noninvasively assessed by fluorescence lifetime spectroscopy (FLS) either 1 week or 3 weeks after implantation (Day 18 or Day 32 post-seeding for 1-week and 3-week cohorts, respectively). After *in vivo* optical assessment, mice were euthanized and EVPOMEs sectioned and processed for histological assessment of tissue integration. The post-implantation histology protocol was the same as the pre-implantation protocol described above. Representative post-implantation construct histology is shown in the right-most column of **Fig. 4.2**. After 3 weeks, both control and stressed constructs consisted of re-epithelialized cell layers and neovasculation originating from the mouse.

4.2.4 Construct Implantation Protocol

All animal experiments were approved by the University of Michigan Committee on Use and Care of Animals. After procedures for pre-implantation assessments were completed on Day 11, constructs were implanted in dorsal subcutaneous pouches of 7- to 8-week old female severe combined immunodeficiency (SCID) mice as previously described [37]. Briefly, mice were administered isoflurane via nose cone for anesthesia. The dorsal skin was disinfected with betadine (Purdue Products L.P.). A full-thickness curvilinear incision was made down to the panniculus carnosus to create a skin pouch approximately twice the size of the construct ($\sim 2 \text{ cm}^2$). The construct was oriented such that the dermal equivalent was in contact with the muscular fascia. A thin silastic sheet ($\sim 130 \text{ }\mu\text{m}$ thick, $\sim 2 \text{ cm}^2$) was placed over the construct to prevent adhesion with the skin. The skin pouch was secured using removable surgical staples (Autoclip™, Becton Dickinson).

4.2.5 Fluorescence Lifetime Spectroscopy Instrumentation

Time-resolved fluorescence decays were acquired *in situ* from the implanted constructs by employing clinically-compatible prototype fluorescence lifetime spectroscopy (FLS) instrumentation [32-34], shown in **Fig. 4.3**. A pulsed 355 nm laser (1 kHz repetition rate; 500 ps pulse width) excited endogenous fluorophores in the constructs. The 355 nm wavelength was selected to maximize excitation of the endogenous fluorophore nicotinamide adenine dinucleotide (phosphate) (NAD(P)H), an indicator of cellular metabolism [27,49]. Excitation light was directed to the constructs by a central optical fiber of 200 μm core diameter that was surrounded by six 200 μm core diameter optical fibers (R200-ANGLE-UV, Ocean Optics). This optical fiber probe has a 30° angled window tip. The angled probe was selected for two reasons. First, angling the probe increases the optical interrogation volume of the superficial tissue layers relative to the underlying native mouse tissue [50-52]. Second, the angle reduces collection of reflected excitation light from the tissue surface.

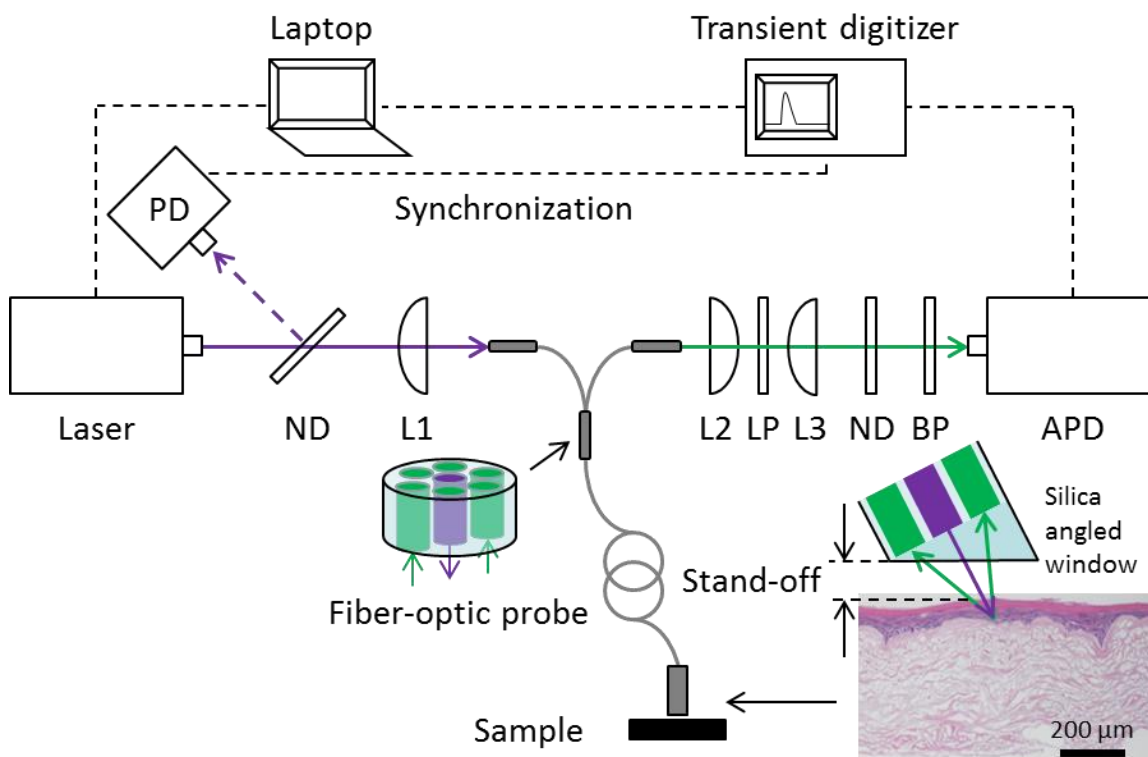


Fig. 4.3. Schematic of fluorescence lifetime spectroscopy (FLS) system components. The distal end of the fiber probe is positioned at varying stand-off distances from the top of the tissue sample. The system acquires data in less than one second per measurement. The handheld probe is sufficiently small to be positioned at multiple sites on each construct. The angled probe design aids in localizing optical interrogation to the top living cell layer of the construct, and reduces collection of reflected excitation light. ND: neutral density filter. PD: photodiode. L1, L2, L3: lenses. LP: long pass filter. BP: band pass filter. APD: avalanche photodiode.

The emitted fluorescence signal was focused onto an avalanche photodiode (APD, C5658, Hamamatsu) by a series of lenses (L2, L3). A 387 nm long pass filter (LP) blocked reflected excitation light. An additional band-pass filter (centered at 540 ± 20 nm) was employed to increase sensitivity of NAD(P)H fluorescence sensing relative to collagen (peak fluorescence emission wavelength 460 nm) [34]. The time-resolved fluorescence intensity detected by the APD was digitized by a 4 MHz oscilloscope (TDS 784A, Tektronix). A small portion of the laser excitation pulse was reflected to a photodiode (PD) by a neutral density filter (ND) to synchronize the oscilloscope data acquisition to the excitation. Instrument response functions (IRFs) were recorded for the APD by placing a cuvette of 0.54 μm diameter silica

microspheres suspended in de-ionized water (1.7%) at the distal end of the probe and removing the LP filter from the light path. The excitation laser pulse was diffusely reflected off the microspheres and passed to the APDs for characterization of the IRF.

4.2.6 *Fluorescence Lifetime Spectroscopy Measurement Protocol*

Implanted constructs were assessed *in situ* by noninvasive fluorescence lifetime spectroscopy either 1 week or 3 weeks post-implantation. Mice were placed prone and anesthetized using isoflurane administered via nose cone. A curvilinear incision was made in the area where constructs were implanted, and the silastic sheet was removed to expose the implanted constructs for measurement. Mice were placed on a stage equipped with a heating pad set to 100°F to maintain body temperature. The stage could be tilted to align the construct perpendicularly to the optical axis of the FLS probe. Measurements were acquired from 2 randomly selected sites on the implanted constructs at 5 stand-off distances from the tissue surface (0 to 2 mm in increments of 0.5 mm). A computer-controlled, micrometer-guided 3-axis linear translation stage precisely (~10 μm resolution) located the FLS probe to carefully select measurement sites and set stand-off distances. Control measurements were acquired from exposed muscle tissue adjacent to the construct and from neighboring bare skin. The duration of each FLS measurement was ~500 msec.

4.2.7 *Fluorescence Lifetime Spectroscopy Data Analysis*

The protocol for analyzing fluorescence decays acquired by the FLS has been previously reported^{32,34}. Briefly, time-resolved fluorescence measurements acquired from the mice were interpreted as a convolution of the intrinsic fluorescence decay from the animal and the instrument response function (IRF). Extraction of quantitative fluorescence parameters of biological interest from these measurements consists of two main steps: 1) deconvolution of the IRF from the intrinsic fluorescence decay, and 2) fitting of the intrinsic fluorescence decay to a

simulated exponential model. The data was well-fitted to a double-exponential model:

$$f(t) = A_1 e^{-t/\tau_1} + A_2 e^{-t/\tau_2} \quad (\text{Eq. 1})$$

Here, τ_1 and τ_2 represent fluorescence lifetimes of long-lived and short-lived component fluorophores within the sample, respectively. A_1 and A_2 are amplitudes that represent the weighted contribution of these components.

Only measurements that met certain criteria were included for data analysis. First, the peak fluorescence intensity of the measurement, I_{peak} , must have been greater than the threshold defined by **Eq. 2**:

$$I_{peak} > \mu_{I,peak} - \sigma_{I,peak} \quad (\text{Eq. 2})$$

where $\mu_{I,peak}$ and $\sigma_{I,peak}$ are the average and standard deviation, respectively, of the peak signal intensities for all measurements. The thresholds were set independently per cohort.

The second criteria for measurements to be included was that the Pearson's cumulative chi-squared test statistic, χ^2 , of the simulation model fit (described below) was less than 0.1, indicating that the least-squares algorithm and IRF selected produced an excellent fit to the data, ensuring that the extracted optical parameters are valid. Finally, the fluorescence decay must not have contained saturated signal. The number of measurements that met these three inclusion criteria for each experimental group within each cohort is listed in **Table 4.1**.

Table 4.1. Table of Measurements. Optical measurements were acquired from 2 sites per construct, and from 5 stand-offs per site. Included measurements met criteria for raw signal strength and quality of model fit.

1 Week Post-Implantation					
Condition	Patients	Constructs	Sites	Meas. Acquired	Meas. Included
Control	4	7	14	70	48
Stressed	4	9	18	90	80
Total:		16	32	160	128

3 Weeks Post-Implantation					
Condition	Patients	Constructs	Sites	Meas. Acquired	Meas. Included
Control	4	7	14	70	52
Stressed	4	7	14	70	40
Total:		14	28	140	92

All fluorescence decays were background-corrected for ambient light prior to analysis. Because the travel time of light through the fiber-optic probe can change the temporal alignment between the delivered laser pulse and the detected fluorescence, certain IRF measurements required temporal shifting with respect to the fluorescence decay to produce a good fit to the data. Therefore, we iteratively shifted the IRF and performed the Levenberg-Marquardt least-squares fitting algorithm (MATLAB R2013b) for all measurements on each mouse, for each IRF measurement. The IRF measurement and temporal shift that produced the smallest χ^2 value, after applying the three inclusion criteria above, was used as the best-fit IRF for that mouse.

To quantitatively assess the viability of the constructs, we calculated the optical parameter A_1/A_2 for each measurement after fitting the fluorescence decay profiles according to **Eq. 1**. This parameter is the ratio of contribution of the short-lifetime term to the long-lifetime term and has been previously shown to correlate to cell metabolism [53,54].

4.2.8 Statistical Analysis

We were interested in the relationship between the pre-implantation construct health and the post-implantation optically measured parameter A_1/A_2 . Given the hierarchical grouping of the measurements (stand-offs within sites, sites within constructs, constructs within patients), we fit the data using a linear mixed-effects model [55]. Mixed-effects models consist of fixed-effects terms that contain the conventional linear regression part, and random-effects terms that contain the common random effects within grouping levels. In our model, the response variable is the post-implantation optically measured parameter A_1/A_2 . The primary independent variable is the pre-implantation construct health, quantified as the concentration of secreted cytokines, IL-8, hBD-1, or VEGF. Patients and constructs are each included as random intercepts, accounting for correlations from sites sampled within constructs and constructs sampled within patients. Five levels of stand-offs are also included as dummy variables; only standoff of 2mm shows significantly higher A_1/A_2 levels from those of the other stand-off levels (0 mm, 0.5 mm, 1 mm, 1.5 mm).

The linear mixed-effects model was fit for the parameter A_1/A_2 versus each of the three cytokines, for each cohort (1-week and 3-week) separately. Significance was determined at $\alpha < 0.05$. Analysis was performed using the Statistics Toolbox (v. 8.3) in MATLAB (R2013b).

4.3 Results

4.3.1 Characterization of In Vivo Fluorescence Lifetime Spectroscopy Measurements

Fig. 4.4A shows representative fluorescence decays, acquired from one mouse, from the construct (On Site), adjacent exposed muscle tissue (Off Site), and neighboring bare skin, for the purpose of visualizing characterization of the fluorescence lifetime spectroscopy (FLS) system. All measurements shown were taken at the same stand-off distance (0.5 mm). Fluorescence intensities are normalized to the maximum intensity of all depicted measurements. Raw signal

intensity of control measurements acquired from muscle tissue off site of the construct was less than 30% of that from on site of the construct. Raw signal intensity acquired from neighboring bare skin was less than 6% of the intensity from the construct.

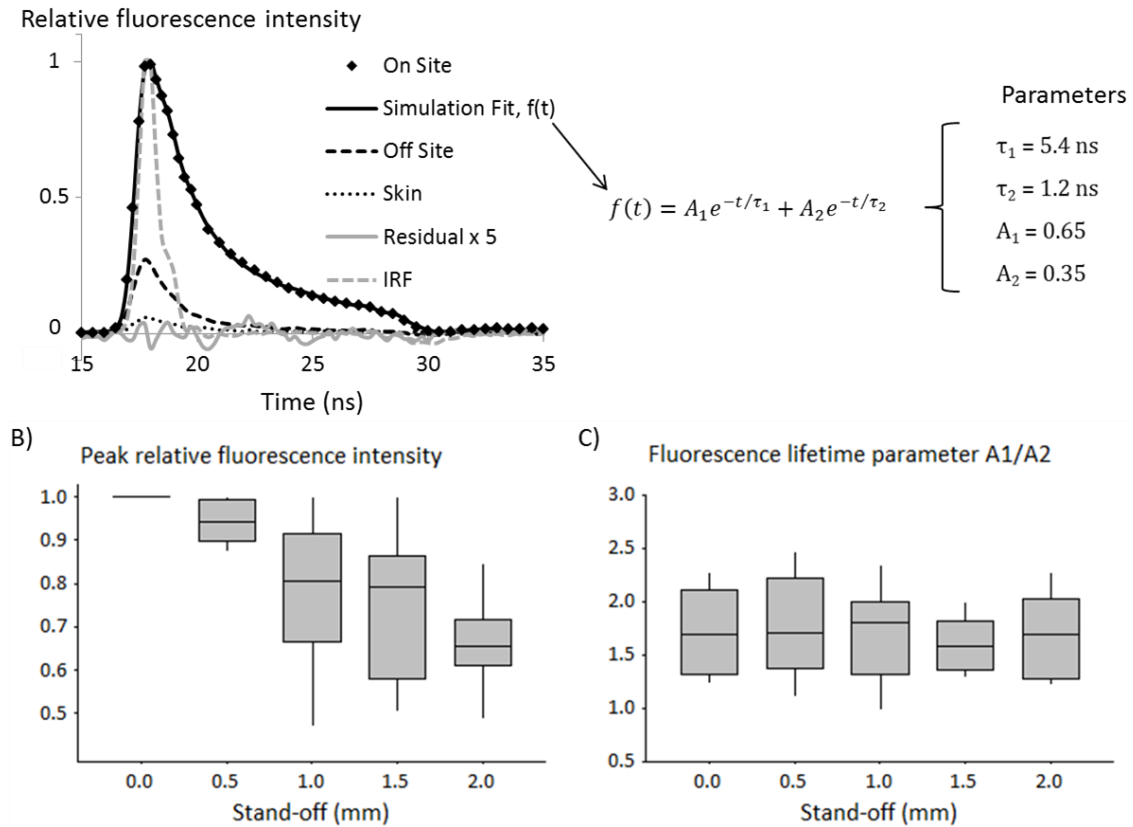


Fig. 4.4. Fluorescence lifetime spectroscopy (FLS) data analysis. A) Representative time-resolved fluorescence decays acquired from one mouse, at one stand-off. Fluorescence data acquired from the construct (On Site, diamonds) were fit to a bi-exponential decay (Simulation Fit, solid line), for extraction of fluorescence lifetime parameters τ_1 , τ_2 , A_1 , and A_2 . The residual difference between the data and the simulation fit is no more than 2% (gray line). Signals acquired from muscle tissue adjacent to the construct (Off Site, dashed line) and neighboring skin (dotted line) are significantly lower than signal from the construct. B) Box plots of peak fluorescence intensity, categorized by stand-off distance of probe from tissue sample. Peak fluorescence intensity from the constructs decreased consistently as the stand-off distance increased. C) However, the extracted fluorescence lifetime parameter A_1/A_2 was consistent for all stand-off distances. Therefore, the fluorescence lifetime parameters from all stand-offs per construct may be combined for data analysis. Data for box plots is for week 1 control measurements (N = 9, 12, 12, 8, 7 for stand-offs 0.0 – 2.0 mm, respectively).

The solid curve represents the simulation fit resulting from the least-squares iterative reconvolution algorithm. The goodness of fit can be visualized from the residual gray curve, which has been multiplied 5-fold to be visible on the plot. For this representative decay, the residual difference between the measured data and the simulation fit is less than 2%. The average reduced chi-squared for all included measurements in the study was 0.05, indicating that this double-exponential model provides an excellent fit to the data, and ensuring confidence in the extracted fluorescence lifetime parameters A_1 , A_2 , τ_1 and τ_2 .

Fig. 4.4B shows a box plot that categorizes fluorescence intensities measured from the implanted constructs by stand-off distance of the probe from the tissue sample. The data shown here is for the control group of the 1-week cohort. Each measurement is normalized to the intensity at the stand-off distance that has the strongest raw signal intensity within that site. As shown in the box plot, the strongest fluorescence intensity was always at a stand-off distance of 0.0 mm, when the probe is in contact with the tissue surface. The fluorescence intensity consistently decreased as the stand-off distance increased. However, as shown in **Fig. 4.4C**, the variability and range of the extracted fluorescence lifetime parameter A_1/A_2 does not depend on stand-off distance. This result indicates that the parameter A_1/A_2 is insensitive to stand-off distance, and therefore measurements from all stand-off distances taken per site may be combined for analysis.

4.3.2 *Correlation between In Vivo Optical Parameters and In Vitro Cytokine Secretion*

Since the optical parameter A_1/A_2 is insensitive to stand-off distance, A_1/A_2 measured for each construct (in other words, each mouse) was averaged. The scatter plots in **Fig. 4.5** show the relationship between A_1/A_2 and each of the three pre-implantation cytokine secretion levels, for the 1-week cohort mice only. *In vivo* fluorescence sensing found that A_1/A_2 values vary across the 1-week implantation study population. This ratio correlated negatively with pre-implantation cytokine secretion levels. Constructs that exhibited high cytokine secretion levels prior to

implantation yielded smaller A_1/A_2 values after 1-week of tissue integration. The linear regression coefficients are -0.030 ($p = 0.012$), -0.009 ($p = 0.000$), and -0.006 ($p = 0.001$) for IL-8, hBD-1, and VEGF, respectively, indicating a significant correlation between A_1/A_2 values and cytokine concentration for all three proteins.

By contrast, although A_1/A_2 values also varied across the 3-week population with similar range and variability as the 1-week population, the data did not indicate any correlation with respect to pre-implantation cytokine concentrations (scatter plots not shown). The linear regression coefficients are -0.018 ($p = 0.122$), 0.001 ($p = 0.335$), and 0.000 ($p = 0.819$) for IL-8, hBD-1, and VEGF, respectively, indicating no significant correlation between A_1/A_2 values and cytokine concentration for all three proteins for the 3-week cohort.

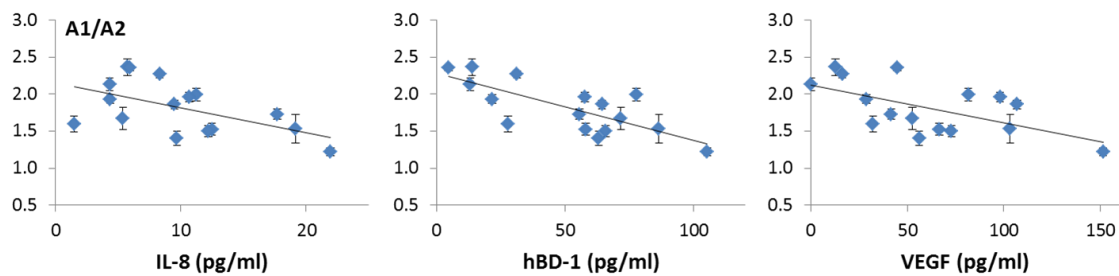


Fig. 4.5. Noninvasive optical sensing of implanted constructs. The fluorescence lifetime parameter A_1/A_2 varied across the 1-week implantation study population. This ratio correlated negatively with pre-implantation protein concentration levels for all three constitutively secreted proteins (linear mixed effects model, $p < 0.05$ for all three). Each data point represents the average value per construct, with standard error.

4.4 Discussion

Our results suggest that optical parameters measured from implanted tissue engineered constructs by fluorescence lifetime spectroscopy can noninvasively assess the integration of engineered tissue with native tissue. We showed that the optical parameter A_1/A_2 , measured 1 week after implantation in mice, tended to be lower for constructs that secreted higher levels of IL-8, hBD-1, and VEGF prior to implantation. These three cytokines are direct indicators of the cellular viability and

function of the constructs and promote integration, and post-implantation histology confirmed that control constructs (which have high cytokine secretion levels) had thicker living cell layers than stressed constructs at this time point. A_1/A_2 did not correlate with pre-implantation cytokine secretion after the constructs had been implanted in mice for 3 weeks. Histology showed that native mouse cells had infiltrated most of these constructs, regardless of their pre-implantation health state. This is expected, as even the implantation of bare dermal equivalent aids re-epithelialization and revascularization by providing a substrate [5]. The infiltration of mouse cells may explain the lack of correlation of A_1/A_2 with cytokine secretion.

FLS technology was employed for its ability to assess biochemical changes that can characterize cellular metabolism. This was motivated by our recently published finding that fluorescence lifetime-based sensing differentiates between control and stressed constructs *in vitro* [27]. In that study, we found that the percent contribution of the long-lived fluorophore is significantly lower for control constructs than stressed constructs. Therefore, our *in vivo* results for the 1-week implantation cohort are consistent with our previously *in vitro* results. Furthermore, Wu *et al.* used depth-resolved fluorescence lifetime spectroscopy to find that the percent contribution of the short-lived fluorophore was greater in the epithelial cell layer of excised oral mucosa than in the dermal layer [53]. They attributed the difference to the presence of NADH in the cell layer, which has a shorter fluorescence lifetime than the collagen in the dermal layer. Similarly, we found that implanted constructs with high pre-implantation cytokine secretion levels, and therefore more viable cells, had lower A_1/A_2 values, indicating greater contribution from short-lived fluorophores (A_2).

Characterization of the instrument demonstrates some advantages of employing FLS for this application. The optical fluorescence lifetime parameter is insensitive to stand-off distance from the probe to the tissue surface. This is further evidenced by the small standard errors shown on the scatter plots of **Fig. 4.5**, where all stand-offs from each construct are averaged. This is beneficial for the challenging

clinical environment, where the clinician may not be able to easily and precisely handle the probe while accessing small confines, such as inside a patient's mouth. Fluorescence lifetime methods are also less sensitive to local tissue absorption and scattering properties that can affect the collected spectral lineshape in unpredictable ways. Further, the acquisition time per measurement is less than 500 milliseconds, which allows for rapid real-time assessment, and overcomes patient-related motion artifacts.

One of the drawbacks of bulk tissue sensing, such as in this demonstration, is that the instrument has limited spatial resolution. In the example of our model tissue construct, EVPOME, even healthy constructs will have living cell layers ~ 30 μm thick, whereas the underlying dermal equivalent could be ~ 500 μm thick. Therefore, even the healthiest constructs with the thickest cell layers will detect a larger fluorescence contribution from the underlying dermal equivalent rather than the living cells. This effect is apparent in our results, as A_1/A_2 is always greater than 1, indicating that the long-lived fluorescence contribution from the dermal layer overwhelms the short-lived fluorescence contribution from the cell layer. Our recently published *in vitro* study [27] was based on multiphoton microscopy (MPM) technology, which has inherent optical sectioning properties to enhance spatial targeting of the epithelial cell layer, as well as increased tissue penetration depth. However, the large size of multiphoton laser sources creates a barrier to clinical translation. Therefore in this implementation we have used single-photon fluorescence spectroscopy. Cheng *et al.* have recently demonstrated a handheld fluorescence lifetime imaging system for oral cancer imaging *in vivo* based on single-photon excitation, demonstrating promise that our system could be used in human applications [56].

We demonstrated a methodology to rapidly and noninvasively assess engineered tissue constructs *in situ* by measuring endogenous optical signals using fluorescence lifetime spectroscopy. This is the first demonstration of post-implantation assessment of the cellular metabolic activity of engineered epithelial

tissues *in situ*, to our knowledge. Since optical parameters measured *in vivo* correlated with pre-implantation cytokine concentrations, which indicate cell viability and functionality and predict healthy construct integration [12], FLS can be a promising tool for assessing tissue integration and graft success.

References

1. Fisher, M.B., and Mauck, R.L. Tissue engineering and regenerative medicine: recent innovations and the transition to translation. *Tissue engineering.Part B, Reviews* **19**, 1, 2013.
2. Hellman, K.B. Tissue Engineering: Translating Science to Product. In: Ashammakhi, N., Reis, R. and Chiellini, F., eds. *Topics in Tissue Engineering. E-Book.* : http://www.oulu.fi/spareparts/ebook_topics_in_t_e_vol4/, 2008, pp. 1-28.
3. Bertram, T.A., Tentoff, E., Johnson, P.C., Tawil, B., Van Dyke, M., and Hellman, K.B. Hurdles in tissue engineering/regenerative medicine product commercialization: a pilot survey of governmental funding agencies and the financial industry. *Tissue engineering.Part A* **18**, 2187, 2012.
4. Lee, M.H., Arcidiacono, J.A., Bilek, A.M., Wille, J.J., Hamill, C.A., Wonnacott, K.M., Wells, M.A., and Oh, S.S. Considerations for tissue-engineered and regenerative medicine product development prior to clinical trials in the United States. *Tissue engineering.Part B, Reviews* **16**, 41, 2010.
5. Berthiaume, F., Maguire, T.J., and Yarmush, M.L. Tissue engineering and regenerative medicine: history, progress, and challenges. *Annual review of chemical and biomolecular engineering* **2**, 403, 2011.
6. MacNeil, S. Progress and opportunities for tissue-engineered skin. *Nature* **445**, 874, 2007.
7. Moharamzadeh, K., Colley, H., Murdoch, C., Hearnden, V., Chai, W.L., Brook, I.M., Thornhill, M.H., and Macneil, S. Tissue-engineered oral mucosa. *Journal of dental research* **91**, 642, 2012.
8. Barrientos, S., Stojadinovic, O., Golinko, M.S., Brem, H., and Tomic-Canic, M. Growth factors and cytokines in wound healing. *Wound repair and regeneration : official publication of the Wound Healing Society [and] the European Tissue Repair Society* **16**, 585, 2008.
9. Werner, S., and Grose, R. Regulation of wound healing by growth factors and cytokines. *Physiological Reviews* **83**, 835, 2003.
10. Shakespeare, P.G. The role of skin substitutes in the treatment of burn injuries. *Clinics in dermatology* **23**, 413, 2005.
11. Xu, Q., Izumi, K., Tobita, T., Nakanishi, Y., and Feinberg, S.E. Constitutive release of cytokines by human oral keratinocytes in an organotypic culture. *Journal of oral and maxillofacial surgery : official journal of the American Association of Oral and Maxillofacial Surgeons* **67**, 1256, 2009.

12. Kuo, S., Zhou, Y., Kim, H.M., Kim, R.Y., Marcelo, C.L., Kennedy, R., and Feinberg, S.E. Growth factors and chemokines as indicators of implantation success of tissue-engineered oral mucosa. (In preparation).
13. Ashjian, P., Elbarbary, A., Zuk, P., DeUgarte, D.A., Benhaim, P., Marcu, L., and Hedrick, M.H. Noninvasive *in situ* evaluation of osteogenic differentiation by time-resolved laser-induced fluorescence spectroscopy. *Tissue engineering* **10**, 411, 2004.
14. Kutsuna, T., Sato, M., Ishihara, M., Furukawa, K.S., Nagai, T., Kikuchi, M., Ushida, T., and Mochida, J. Noninvasive evaluation of tissue-engineered cartilage with time-resolved laser-induced fluorescence spectroscopy. *Tissue engineering, Part C, Methods* **16**, 365, 2010.
15. Sun, Y., Responde, D., Xie, H., Liu, J., Fatakdawala, H., Hu, J., Athanasiou, K.A., and Marcu, L. Nondestructive evaluation of tissue engineered articular cartilage using time-resolved fluorescence spectroscopy and ultrasound backscatter microscopy. *Tissue engineering, Part C, Methods* **18**, 215, 2012.
16. Tan, W., Sendemir-Urkmez, A., Fahrner, L.J., Jamison, R., Leckband, D., and Boppart, S.A. Structural and functional optical imaging of three-dimensional engineered tissue development. *Tissue engineering* **10**, 1747, 2004.
17. Tan, W., Oldenburg, A.L., Norman, J.J., Desai, T.A., and Boppart, S.A. Optical coherence tomography of cell dynamics in three-dimensional tissue models. *Optics express* **14**, 7159, 2006.
18. White, S.M., Hingorani, R., Arora, R.P., Hughes, C.C., George, S.C., and Choi, B. Longitudinal *in vivo* imaging to assess blood flow and oxygenation in implantable engineered tissues. *Tissue engineering, Part C, Methods* **18**, 697, 2012.
19. Khmaladze, A., Ganguly, A., Kuo, S., Raghavan, M., Kainkaryam, R., Cole, J.H., Izumi, K., Marcelo, C.L., Feinberg, S.E., and Morris, M.D. Tissue-engineered constructs of human oral mucosa examined by Raman spectroscopy. *Tissue engineering, Part C, Methods* **19**, 299, 2013.
20. Pancrazio, J.J., Wang, F., and Kelley, C.A. Enabling tools for tissue engineering. *Biosensors & bioelectronics* **22**, 2803, 2007.
21. Georgakoudi, I., Rice, W.L., Hronik-Tupaj, M., and Kaplan, D.L. Optical spectroscopy and imaging for the noninvasive evaluation of engineered tissues. *Tissue engineering, Part B, Reviews* **14**, 321, 2008.
22. Lloyd, W.R., Chen, L.-., and Mycek, M.-. Fluorescence Spectroscopy. In: Morgan, S.P., Rose, F.R.A.J. and Mather, S.J., eds. *Optical Techniques in Regenerative Medicine*. : CRC Press, 2014, pp. 171-203.
23. Mycek, M.-., and Pogue, B.W. *Handbook of Biomedical Fluorescence*. New York: Marcel Dekker, Inc., 2003.
24. Lakowicz, J.R. *Principles of Fluorescence Spectroscopy*. New York: Springer, 2006.
25. Berezin, M.Y., and Achilefu, S. Fluorescence lifetime measurements and biological imaging. *Chemical reviews* **110**, 2641, 2010.
26. Marcu, L. Fluorescence lifetime techniques in medical applications. *Annals of Biomedical Engineering* **40**, 304, 2012.

27. Chen, L.-, Lloyd, W.R., Kuo, S., Kim, H.M., Marcelo, C.L., Feinberg, S.E., and Mycek, M.-. Label-free nonlinear optical molecular microscopy non-invasively characterizes viability of engineered human tissue constructs. *Biomaterials*, 2014. (Accepted)
28. Glanzmann, T., Ballini, J., van den Bergh, H., and Wagnieres, G. Time-resolved spectrofluorometer for clinical tissue characterization during endoscopy. *Review of scientific instruments* **70**, 4067, 1999.
29. Fang, Q., Papaioannou, T., Jo, J.A., Vaitha, R., Shastry, K., and Marcu, L. Time-domain laser-induced fluorescence spectroscopy apparatus for clinical diagnostics. *Review of Scientific Instruments* **75**, 151, 2003.
30. Pfefer, T.J., Paithankar, D.Y., Ponerros, J.M., Schomacker, K.T., and Nishioka, N.S. Temporally and spectrally resolved fluorescence spectroscopy for the detection of high grade dysplasia in Barrett's esophagus. *Lasers in surgery and medicine* **32**, 10, 2003.
31. Coda, S., Thompson, A.J., Kennedy, G.T., Roche, K.L., Ayaru, L., Bansi, D.S., Stamp, G.W., Thillainayagam, A.V., French, P.M., and Dunsby, C. Fluorescence lifetime spectroscopy of tissue autofluorescence in normal and diseased colon measured *ex vivo* using a fiber-optic probe. *Biomedical optics express* **5**, 515, 2014.
32. Pitts, J.D., and Mycek, M.-. Design and development of a rapid acquisition laser-based fluorometer with simultaneous spectral and temporal resolution. *Review of Scientific Instruments* **72**, 3061, 2001.
33. Vishwanath, K., Pogue, B., and Mycek, M.A. Quantitative fluorescence lifetime spectroscopy in turbid media: comparison of theoretical, experimental and computational methods. *Physics in Medicine and Biology* **47**, 3387, 2002.
34. Chandra, M., Vishwanath, K., Fichter, G.D., Liao, E., Hollister, S.J., and Mycek, M.A. Quantitative molecular sensing in biological tissues: an approach to non-invasive optical characterization. *Optics express* **14**, 6157, 2006.
35. Izumi, K., Takacs, G., Terashi, H., and Feinberg, S.E. *Ex vivo* development of a composite human oral mucosal equivalent. *Journal of oral and maxillofacial surgery : official journal of the American Association of Oral and Maxillofacial Surgeons* **57**, 571, 1999.
36. Izumi, K., Terashi, H., Marcelo, C.L., and Feinberg, S.E. Development and characterization of a tissue-engineered human oral mucosa equivalent produced in a serum-free culture system. *Journal of dental research* **79**, 798, 2000.
37. Izumi, K., Feinberg, S.E., Terashi, H., and Marcelo, C.L. Evaluation of transplanted tissue-engineered oral mucosa equivalents in severe combined immunodeficient mice. *Tissue engineering* **9**, 163, 2003.
38. Izumi, K., Feinberg, S.E., Iida, A., and Yoshizawa, M. Intraoral grafting of an *ex vivo* produced oral mucosa equivalent: a preliminary report. *International journal of oral and maxillofacial surgery* **32**, 188, 2003.
39. Izumi, K., Song, J., and Feinberg, S.E. Development of a tissue-engineered human oral mucosa: from the bench to the bed side. *Cells, tissues, organs* **176**, 134, 2004.
40. Yoshizawa, M., Koyama, T., Kojima, T., Kato, H., Ono, Y., and Saito, C. Keratinocytes of tissue-engineered human oral mucosa promote re-

- epithelialization after intraoral grafting in athymic mice. *Journal of oral and maxillofacial surgery : official journal of the American Association of Oral and Maxillofacial Surgeons* **70**, 1199, 2012.
41. Izumi, K., Neiva, R.F., and Feinberg, S.E. Intraoral grafting of tissue-engineered human oral mucosa. *The International journal of oral & maxillofacial implants* **28**, e295, 2013.
 42. Rennekampff, H.O., Hansbrough, J.F., Kiessig, V., Dore, C., Sticherling, M., and Schroder, J.M. Bioactive interleukin-8 is expressed in wounds and enhances wound healing. *The Journal of surgical research* **93**, 41, 2000.
 43. Michel, G., Kemeny, L., Peter, R.U., Beetz, A., Ried, C., Arenberger, P., and Ruzicka, T. Interleukin-8 receptor-mediated chemotaxis of normal human epidermal cells. *FEBS letters* **305**, 241, 1992.
 44. Tuschil, A., Lam, C., Haslberger, A., and Lindley, I. Interleukin-8 stimulates calcium transients and promotes epidermal cell proliferation. *The Journal of investigative dermatology* **99**, 294, 1992.
 45. Prado-Montes de Oca, E. Human beta-defensin 1: a restless warrior against allergies, infections and cancer. *The international journal of biochemistry & cell biology* **42**, 800, 2010.
 46. Sayama, K., Komatsuzawa, H., Yamasaki, K., Shirakata, Y., Hanakawa, Y., Ouhara, K., Tokumaru, S., Dai, X., Tohyama, M., Ten Dijke, P., Sugai, M., Ichijo, H., and Hashimoto, K. New mechanisms of skin innate immunity: ASK1-mediated keratinocyte differentiation regulates the expression of beta-defensins, LL37, and TLR2. *European journal of immunology* **35**, 1886, 2005.
 47. Frye, M., Bargon, J., and Gropp, R. Expression of human beta-defensin-1 promotes differentiation of keratinocytes. *Journal of Molecular Medicine (Berlin, Germany)* **79**, 275, 2001.
 48. Nakanishi, Y., Izumi, K., Yoshizawa, M., Saito, C., Kawano, Y., and Maeda, T. The expression and production of vascular endothelial growth factor in oral mucosa equivalents. *International journal of oral and maxillofacial surgery* **36**, 928, 2007.
 49. Wu, Y., and Qu, J.Y. Autofluorescence spectroscopy of epithelial tissues. *Journal of Biomedical Optics* **11**, 054023, 2006.
 50. Pfefer, T.J., Schomacker, K.T., Ediger, M.N., and Nishioka, N.S. Multiple-fiber probe design for fluorescence spectroscopy in tissue. *Applied Optics* **41**, 4712, 2002.
 51. Pfefer, T.J., Matchette, L.S., Ross, A.M., and Ediger, M.N. Selective detection of fluorophore layers in turbid media: the role of fiber-optic probe design. *Optics Letters* **28**, 120, 2003.
 52. Zhu, C., Liu, Q., and Ramanujam, N. Effect of fiber optic probe geometry on depth-resolved fluorescence measurements from epithelial tissues: a Monte Carlo simulation. *Journal of Biomedical Optics* **8**, 237, 2003.
 53. Wu, Y., and Qu, J.Y. Combined depth- and time-resolved autofluorescence spectroscopy of epithelial tissue. *Optics Letters* **31**, 1833, 2006.
 54. Wu, Y., Zheng, W., and Qu, J.Y. Sensing cell metabolism by time-resolved autofluorescence. *Optics Letters* **31**, 3122, 2006.

55. Fitzmaurice, G.M., Laird, N.M., and Ware, J.H. Applied Longitudinal Analysis. : John Wiley & Sons, 2012.
56. Cheng, S., Cuenca, R.M., Liu, B., Malik, B.H., Jabbour, J.M., Maitland, K.C., Wright, J., Cheng, Y.S., and Jo, J.A. Handheld multispectral fluorescence lifetime imaging system for *in vivo* applications. Biomedical optics express **5**, 921, 2014.

Chapter 5.

Design and Construction of an Intravital Depth-Resolved Fluorescence Lifetime Spectrometer

5.1 Introduction

The fluorescence lifetime spectroscopy (FLS) system reported in Chapter 4 is a bulk fluorescence sensing technology. Advantages of bulk fluorescence sensing based on fiber-optic probes include fairly simple and portable instrumentation, fast data acquisition, and straightforward data analysis methods that can be implemented in real time [1]. However, these methods have low spatial resolution. Detected fluorescence photons originate within the volume of overlapping illumination and collection areas. In a typical fiber-optic probe this volume can extend about 1 mm deep into the tissue [2]. Utzinger and Richards-Kortum have published a comprehensive review of fiber-optic probe geometries that can be employed to control this interrogation volume [3]. Lloyd *et al.* review some recent applications of bulk fluorescence sensing in tissue engineering [4].

Nonetheless, Wu *et al.* found that keratin, which comprises the top layer of our healthy epithelial tissue constructs, produces a strong fluorescence signal at 349 nm excitation, and that its spectral characteristics are similar to that of collagen [5]. This creates a serious challenge in interpreting bulk fluorescence spectra measured using conventional fiber-optic probe methods. The fluorescence from collagen in the dermal layer and from keratin in the top layer can interfere with the fluorescence of interest originating from the NADH in the thin living cell layer. Confocal spectroscopy is a depth-resolved technique that effectively suppresses the strong keratin and collagen fluorescence and extracts the epithelial fluorescence. See Chapter 1 for a brief theoretical description of confocal optical sectioning.

In this chapter, we describe the design and construction of an instrument capable of finer resolution depth-sectioning than the FLS system presented in Chapter 4. This confocal fluorescence lifetime spectroscopy (CFLS) system is based on a configuration demonstrated by several groups that utilizes the core of a multimode fiber as a confocal aperture to reject light from out-of-focus planes [6-8]. We engineered a portable, clinically-compatible CFLS system that could be used for assessing tissue engineered construct viability in living mice. We demonstrated depth resolution of tens of microns. We discuss the pitfalls we encountered in the construction of the system, and make recommendations for future work to fully translate this instrument for *in vivo* use.

5.2 Methods

5.2.1 Overall Design Concept

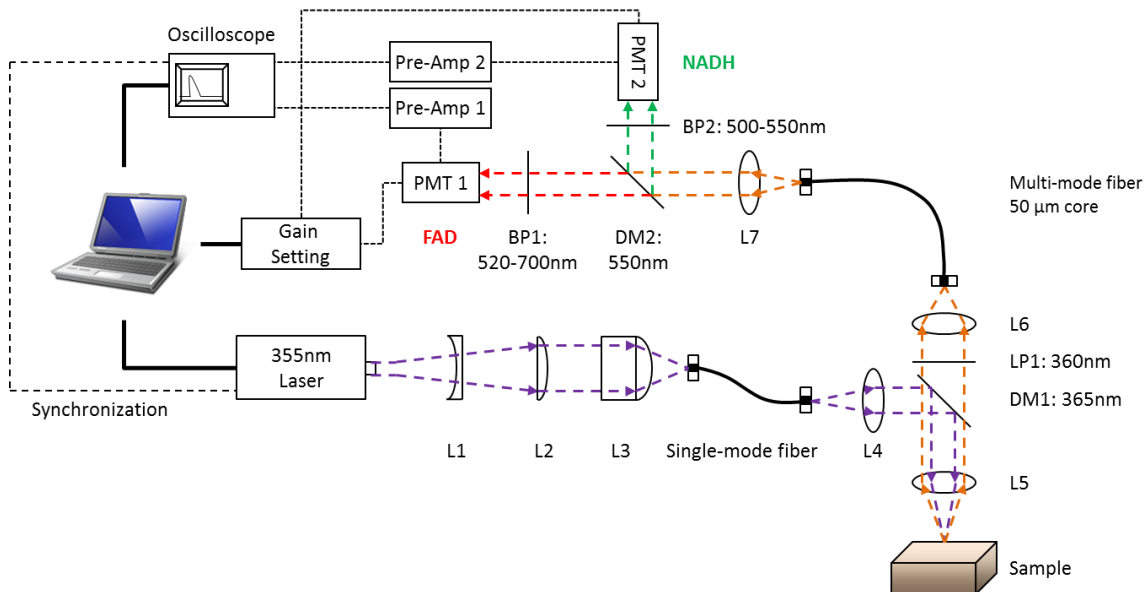


Fig. 5.1. Schematic of confocal fluorescence lifetime spectroscopy (CFLS) system components. Excitation is coupled to a single mode fiber for coherent delivery to the sample arm of the system. Emitted fluorescence signal from the sample is coupled to a multimode fiber, which acts as a confocal pinhole, for delivery to the detection arm of the system. FAD and NADH signals are separated and detected on two channels by photomultiplier tubes and a digitizing oscilloscope. L1-L7: Lenses. DM1 and DM2: Dichroic beamsplitters. LP1: Long pass filter. BP1 and BP2: Band pass filters.

A schematic of the CFLS system is shown in **Fig. 5.1**. The excitation source is a diode pumped solid state laser (CryLas, FTSS 355-Q2, Berlin) that produces emission centered at 355 nm with a repetition rate of 10 kHz and a pulse width of <1.1 ns. An excitation wavelength of 355 nm has been shown to provide the greatest contrast in spectral characteristics between epithelial and stromal layers of tissue, and to strongly excite endogenous NADH fluorescence in the cell layer [9]. The excitation is coupled to a single mode fiber (ThorLabs, P1-305A-FC, Newton, New Jersey) to coherently transmit the excitation to the “sample arm” of the instrument, which can be placed over the animal for intravital assessment. Coupling of the laser source to the single mode fiber by lenses L1, L2, and L3 is described in the next section.

At the sample arm, a UV fused silica lens (L4, ThorLabs, LA4917-UV) collimates the divergent laser light emitting from the single mode fiber. A UV fused silica aspheric lens (L5, Edmund Optics, 49-587, Barrington, New Jersey) with NA = 0.50 and focal length = 15 mm focuses the excitation beam into the sample and collects the backscattered fluorescence signals. The excitation and emission are separated by a 365 nm dichroic beamsplitter (DM1, Semrock, FF365-Di01, Rochester, New York). A 360 nm edge wavelength long pass filter (LP1, Semrock, LP02-355RS-25) further blocks stray excitation light. Lens L6 (ThorLabs, LA1131-A) couples the emission spectra to a 50 μm core diameter multimode fiber (ThorLabs, SFS50/125Y). The core of the fiber is used as a pinhole to collect the confocal fluorescence and conducts the signal to the “detection arm” of the system, which consists of the filtering optics, detection sensors and electronics, and data acquisition equipment.

At the detection arm, to enable cell metabolism sensing, we employed two detection channels. Channel 1 is preferential to FAD and Channel 2 is preferential to NADH. The divergent fluorescence signal emitting from the multimode fiber was collimated by an aspheric lens (L7, Asphericon, 12-20 FPX-S, $f = 20$ mm, NA = 0.29, Jena, Germany). FAD and NADH fluorescence signal were preferentially separated

by the filtering optics DM2, BP1, and BP2 as described in Section 5.2.4 below. The fluorescence signals of each channel were detected by separate identical photomultiplier tubes (PMT 1 and PMT 2, Hamamatsu, H10721, Tokyo). The time-resolved fluorescence intensity detected by the PMTs was digitized on a 1 GHz oscilloscope (TDS-680C Tektronix, Wilsonville, OR) after pre-amplification (Pre-Amp 1 and Pre-Amp 2, XP Power, ECL30UT03-S, Sunnyvale, California). The oscilloscope data acquisition was electronically triggered by a TTL signal from the laser pulse for synchronization with the excitation. The laser and data acquisition were controlled using software provided by CryLas and Tektronix, respectively.

The sample arm was mounted on a motorized three-axis linear translation stage. This stage allows precise control of the of the interrogation volume on the sample. An automated control program was written in Matlab for axial scanning of the focal point through the sample and data acquisition. The sample arm is positioned over a tilting stage that can be equipped with a heating pad and anesthesia equipment for intravital assessment of living mice.

All equipment was mounted on optical breadboards that were secured to a portable cart, including a surge protector for power supply, for transportation to animal facilities and clinics.

5.2.2 Galilean Beam Expander for Single Mode Fiber Coupling

To achieve confocal optical sectioning using optical fibers, the TEM₀₀ mode of the laser must be preserved so that the excitation can be focused to a diffraction-limited spot [10]. Therefore, the excitation light must be transferred to the sample arm via a single mode fiber, which maintains coherence. To efficiently couple the laser beam to the single mode fiber, we must solve a Gaussian beam optics mode-matching problem to determine the focal length of the coupling lens. **Fig. 5.2** below describes the problem.

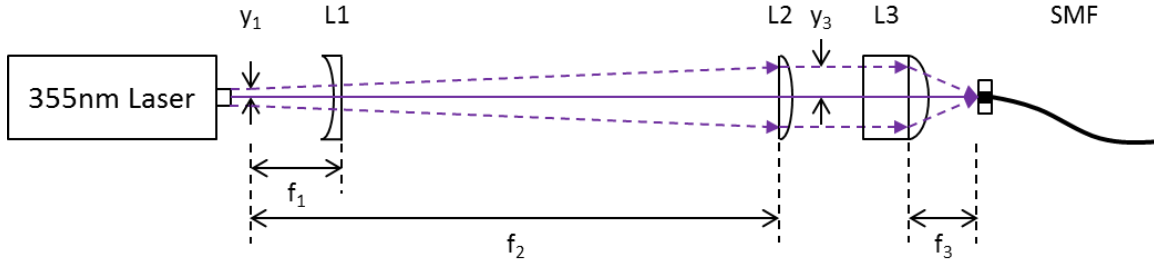


Fig. 5.2. Coupling of laser excitation source to single mode fiber. A Galilean beam expander constructed by lenses L1 and L2 magnifies the laser beam, which has radius y_1 , to fill the back aperture y_3 of the focusing objective L3. The focal length f_3 of the objective lens must be determined to match the Gaussian mode of the fiber.

The focal length f_3 of the focusing objective L3 must be determined to focus the beam to a spot size that matches the mode field diameter of the fiber, MFD . This can be calculated using **Eq. 5.1**, as a function of MFD , the collimated $1/e^2$ laser beam diameter d , and the excitation wavelength λ

$$f_3 = d (\pi MFD) / (4\lambda) \quad \text{Eq. 5.1}$$

To achieve the smallest spot size of the focused laser beam, the beam must be expanded and collimated to completely fill the back aperture of the focusing objective L3. This is achieved by the Galilean beam expander constructed by the plano-concave lens L1 and plano-convex lens L2. This telescope system magnifies the laser beam of radius y_1 by a magnification factor M , to expand the beam radius to y_3 .

$$M = y_3 / y_1 = 2d / y_1 = -f_2 / f_1 \quad \text{Eq. 5.2}$$

Note that the term d in **Eq. 5.1** equals twice the term y_3 in **Eq. 5.2**. We are given the laser beam radius $y_1 = 0.115$ mm and $\lambda = 355$ nm from the laser specifications and $MFD = 2.28$ μm from the fiber specifications. First, we used **Eq. 5.2** to expand the laser beam to a diameter near the entrance aperture of typical focusing objectives, about 10 mm. We therefore used UV-fused silica lenses L1 (ThorLabs LC4210-UV) and L2 (ThorLabs LA4663-UV) with $f_1 = -25$ mm and $f_2 = 1000$ mm to achieve $M = 40$ and expand the beam diameter D to 9.2 mm. We then

used this d in **Eq. 5.1** to determine that the focusing objective should have $f_3 = 46.4$ mm.

Additional requirements of the focusing objective lens L3 are: 1) that the NA matches the NA of the single mode fiber, 0.13, and 2) that the material efficiently transmits UV light with little autofluorescence. We selected the ThorLabs LMU-5X-NUV high-power UV focusing objective lens to meet these requirements. This lens has a focal length of 40 mm, the closest match available to the calculated $f_3 = 46.4$ mm. The NA of 0.13 matches that of the fiber. The theoretical focal spot size is only 3 μm . All of the lens elements within the objective are made from excimer grade UV fused silica and CaF_2 , and have an anti-reflection coating for the 325-500 nm spectral range.

5.2.3 Theoretical Calculation of Axial Resolution

We can control three parameters to affect the axial resolution of the system [11]: 1) the numerical aperture of the focusing lens (L5) that illuminates the sample and collects signal, 2) the magnification determined by the collecting lens (L6) that focuses the emission signal into the multimode fiber, and 3) the pinhole diameter, i.e. the multimode fiber core diameter. To optimize the system design for the smallest axial resolution, we simulated the axial point spread function of the system for varying numerical apertures, magnifications, and pinhole diameters.

T. Wilson described the point spread function in both radial (v) and axial (u) dimensions when sectioning with a finite-sized circular detector, such as the core of the multimode fiber, in our case. The spatial intensity of detected fluorescence signal is:

$$I(v, u) = |h(v)|^2 \left[2\pi \int_0^{v_p-v} |h(t)|^2 t dt + 2 \int_{v_p-v}^{v+v_p} |h(t)|^2 \times \cos^{-1} \left(\frac{t^2 + v^2 - v_p^2}{2tv} \right)^2 t dt \right], \quad v < v_p \quad \text{Eq. 5.3a}$$

$$I(v, u) = 2|h(v)|^2 \int_{v-v_p}^{v+v_p} |h(t)|^2 \cos^{-1} \left(\frac{t^2 + v^2 - v_p^2}{2tv} \right) t dt, \quad v > v_p. \quad \text{Eq. 5.3b}$$

where the radial dimension v is related to the real radial distance r by $v = \frac{2\pi}{\lambda} r(NA)$ and the axial dimension u is related to the real axial distance z by $u = \frac{8\pi}{\lambda} z(NA^2)$. h is the point spread function and v_p is the pinhole radius in optical units [12].

We solved **Eq. 5.3a** and **b** using MATLAB R2013a for an 81x81x81 pixel detection volume (optical units) centered at the focal point of the focusing lens L5. This was repeated for varying pinhole radii from 0 to 120 optical units in increments of 2 optical units. This range was selected because 120 optical units is the equivalent of approximately a 50 μm diameter pinhole, which is the core diameter of our multimode fiber. Representative lateral point spread functions are shown at varying axial depths (in real z axial units) in **Fig. 5.3**. An axial depth of $z = 0 \mu\text{m}$ is defined as the focal point of L5. Transformations from optical to real units were calculated by the equations defined above.

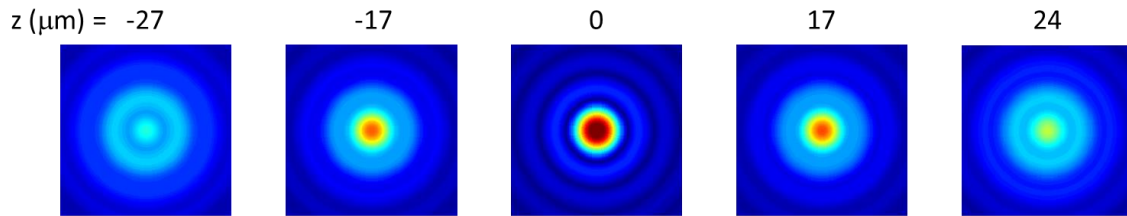


Fig. 5.3. Representative lateral point spread function at varying axial depths. This simulation of the spatial intensity of the detected fluorescence for varying pinhole diameters was used to optimize the numerical aperture and magnification of the optical system.

After completing the simulations for all pinhole diameters from 0 to 50 μm , the axial point spread function full width at half maximum (FWHM) was plotted against the pinhole radius. The results in optical units were transformed to real spatial units for varying numerical apertures and magnifications. **Fig. 5.4a** shows the relationship when magnification is fixed at 3 and NA is varied from 0.1 to 0.7. **Fig. 5.4b** shows the relationship when NA is fixed at 0.4 and magnification is varied from 1 to 20. From these plots, we can see that axial resolution improves for increasing NA and increasing magnification.

From **Fig. 5.4a**, it is apparent that for magnification of 3 and NA of 0.4 and greater, the axial resolution of the system reaches a plateau, no matter the radius of the pinhole. This can guide our selection of lenses L5 and L6. Since we are using a multimode fiber of 50 μm core diameter (the maximum radius shown on the plot), a NA of at least 0.4 is necessary for small axial resolution. According to **Fig. 5.4b**, at NA = 0.4, the magnification must be at least 10 to achieve axial resolution of 10 μm . This would result in using a lens L6 of very long focal length, which would make physical construction of the sample arm difficult. However, as can be seen in **Fig. 5.4a**, using NA = 0.5 would achieve axial resolution of $\sim 12 \mu\text{m}$ with a magnification of 3. Therefore, we selected an aspheric lens with NA = 0.50 and $f = 15 \text{ mm}$ for L5. We selected a lens with $f = 57 \text{ mm}$ for L6, for a magnification of 3.8, and NA of 0.22 to match that of the multimode fiber.

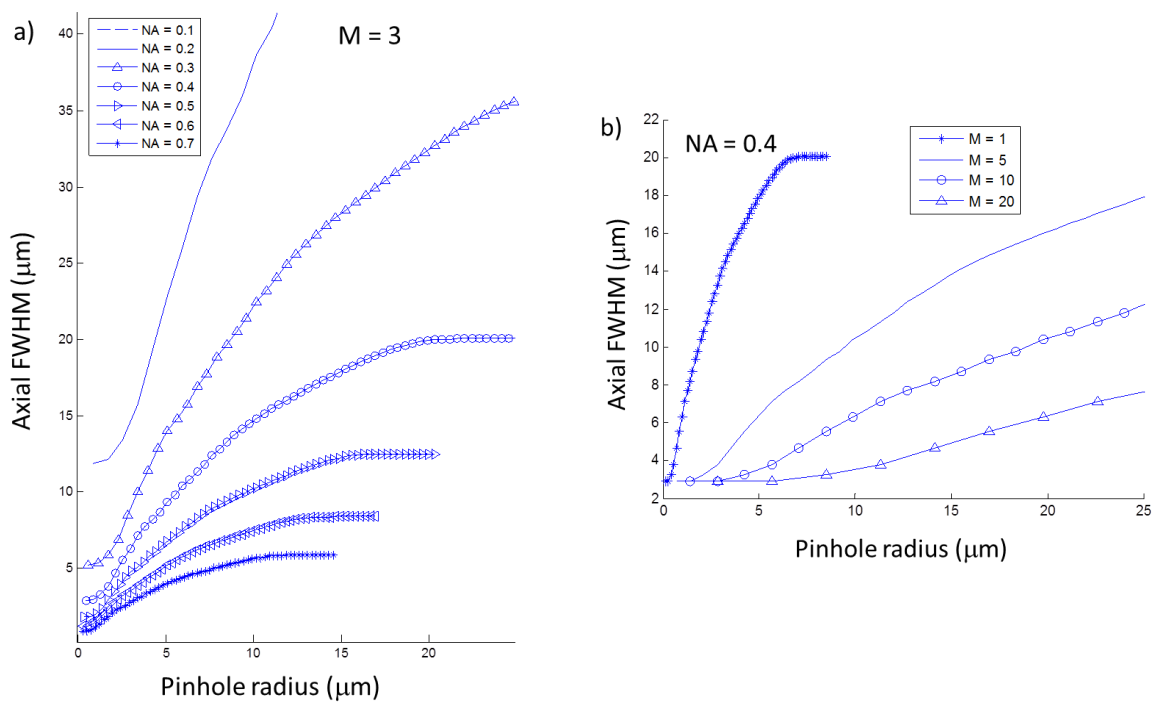


Fig. 5.4. Relationship of axial point spread function to pinhole radius. a) When magnification is fixed at 3, the axial resolution improves with increasing NA. Beyond an NA of 0.4, the axial resolution reaches a plateau even for very large pinhole radii. b) When NA is fixed at 0.4, the axial resolution improved with increasing magnification.

5.2.4 Theoretical Temporal Resolution and Sensitivity

The theoretical temporal characteristics can be estimated following the calculations described by Urayama *et al.* [13]. The fluorescence intensity as a function of time is detected by the PMTs and digitized on a 1 GHz (5 GS/s) oscilloscope (TDS-680C Tektronix, Wilsonville, OR). The PMTs have a system response FWHM of 1.1 ns (SR_{APD}). For each transient decay, 500 data points are acquired, with 200 ps intervals between each data point. The laser pulse duration has a FWHM of 1.1 ns. Using $SR_{exPMT^2} = \sqrt{(SR_{ex}^2 + SR_{PMT}^2)}$ from ref. [13], the overall system response is calculated to be 1.6 ns.

The combined noise (Shot, readout, and thermal) was measured on the PMT by taking the average and standard deviation of the first 30 data points of the data acquisition. The relative standard deviation (RSD) of the noise was 3.6% and a mean voltage of 10 mV. Reasonable signal-to-noise ratios (SNR) for biological studies would ideally be no less than 25 [14]. This corresponds to a PMT output voltage of 257 mV. Fluorescein concentration of 1 μ M yielded a maximum voltage of 1.46 V. Assuming a linear relationship of dye concentration to fluorescence signal, the instrument is theoretically sensitive to detect concentration level as low as 180 nM.

5.2.5 Filters and Dichroic Mirrors

Fig. 5.5 shows the spectral positions of the band-pass filters and dichroic mirrors relative to the normalized fluorescence emission spectra of NADH, FAD, and collagen. The emission spectra at 355 nm excitation were measured by our group previously [15]. The transmission data for the filters and mirrors were downloaded from the manufacturer's website as ASCII files. The first dichroic mirror, DM1, with edge wavelength 365 nm, separates the excitation light from all emission spectra at the sample arm of the instrument. At the detection arm, a second dichroic mirror, DM2, with edge wavelength 550 nm, transmits mostly FAD signal towards Channel 1, and reflects both NADH and collagen signal towards Channel 2. BP1, with

transmission band 520-700 nm, aids in rejecting additional NADH and collagen signal that may have transmitted through DM2, increasing the relative FAD signal collected on Channel 1. BP2, with transmission band 500-550 nm, increases signal collection in the spectral region that is dominated by NADH signal over collagen.

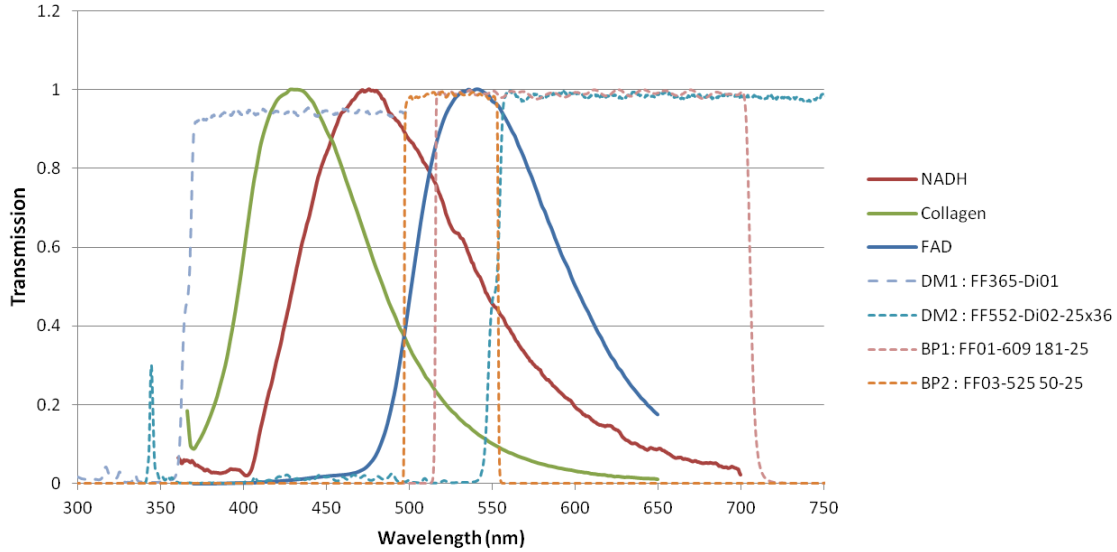


Fig. 5.5. Filtering design to preferentially detect NADH and FAD signal in CFLS. Solid lines show normalized emission spectra of NADH, FAD, and collagen. Dashed lines show transmission spectra of dichroic mirrors and band-pass filters. DM2 separates FAD signal from NADH and collagen signal. BP1 further rejects leaked collagen and NADH signal transmitted towards Channel 1 to preferentially detect FAD. BP2 selects the spectral region dominated by NADH signal over collagen.

5.2.6 Automated Motorized Control and Data Acquisition

Since the lateral and axial resolution of the instrument is on the order of microns, precise spatial localization of the optical interrogation volume is critical. The sample arm was mounted on a computer-controlled, motorized three-axis linear translation stage. The DC servo driven linear actuators (Newport, LTA-HS, Irvine, CA) have sub-micron resolution. The actuators are computer-controlled by a motor control driver (Newport, ESP300). Home-built software in MATLAB controlled axial scanning of the focal volume through the sample, synchronized with data acquisition from the oscilloscope. The axial step size and scanning depth could be set within the program.

5.3 Results

5.3.1 Single Mode Fiber Coupling

The Galilean beam expander was built for coupling the laser excitation to the single mode fiber, pictured in **Fig. 5.6**. The energy per pulse at the source was measured to be 4.1 μJ . The energy at the proximal face of the single mode fiber, after the light has passed through the Galilean beam expander, was 3.6 μJ (12% loss through the optics). The energy at the distal end of the fiber was 3.54 μJ (98% coupling efficiency). However, as the spot size is only $\sim 3 \mu\text{m}$, the energy density is extremely high and the single mode fiber quickly becomes thermally damaged and unusable. Therefore, it is important to always place a neutral density filter (ND) with optical density (OD) no less than 0.3 to prevent burning of the fiber. When using a ND filter with OD = 0.3, 0.77 μJ /pulse is transmitted to the distal end of the fiber.

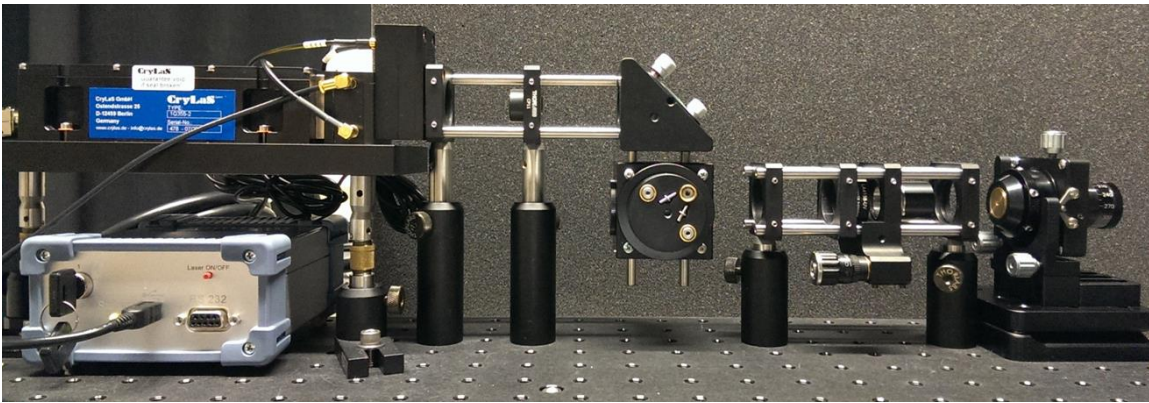


Fig. 5.6. Constructed Galilean beam expander for coupling laser excitation to single mode fiber. The maximum measured coupling efficiency was 98%. However, at this high energy density the fiber would become damaged. A neutral density filter of optical density at least 0.3 is necessary to prevent thermal damage of the fiber.

5.3.2 Construction of portable CFLS system

All components of the CFLS have been constructed and secured to a portable cart, pictured in **Fig. 5.7**.

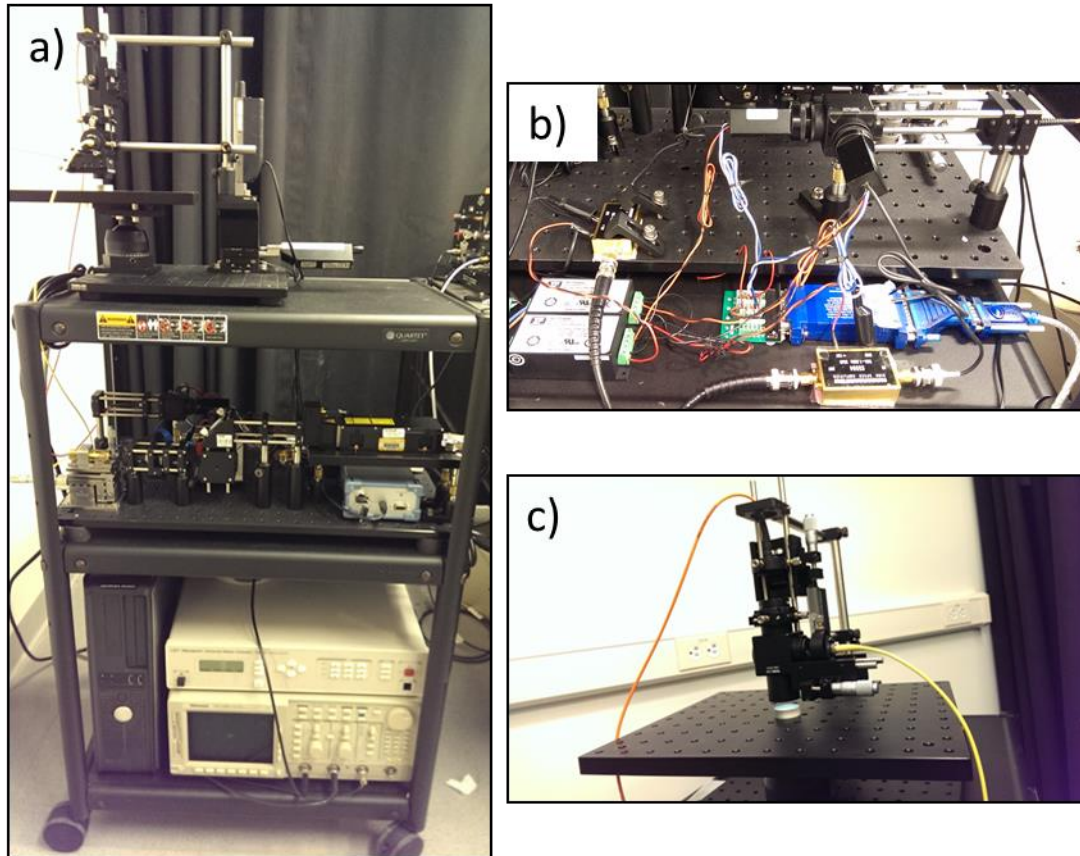


Fig. 5.7. Portable CFLS system. a) The whole system is mounted on a portable cart for clinical use. The lower shelf contains the CPU, oscilloscope, and motor control driver. The middle shelf contains the illumination optics, detection optics and electronics. The top shelf contains the sample arm and the animal stage for intravital assessment. b) The detection electronics are secured to the middle shelf. c) The sample arm is positioned over a tilting stage that can hold the animal. The yellow fiber is the illumination single mode fiber. The orange fiber is the emission multimode fiber.

5.3.3 Reflectance Axial Resolution Testing

The axial resolution of the CFLS was measured by converting the system to a reflectance configuration and translating a reflective mirror axially across the focal volume. The dichroic mirror in the sample arm was replaced with a 50/50 beamsplitter, and the 360 nm long pass filter and 500-550 nm band-pass filter were removed for reflectance assessment. A UV-reflective mirror was placed as the sample. The axial position of the mirror was translated in 10 μm steps, 100 μm on both sides of the focal point, and the reflected laser pulse was acquired at each step. **Fig. 5.8** shows the peak reflectance intensity at each axial step. The axial resolution of the CFLS, estimated from the FWHM of this peak, is 78 μm .

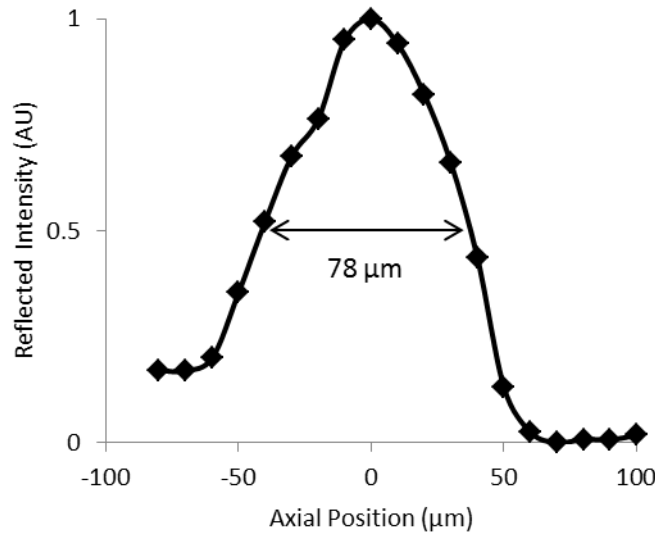


Fig. 5.8. Axial resolution knife edge experiment results. The reflected laser pulse intensity measured from a mirror translated axially across the focal volume has a FWHM of 78 μm , serving as an estimate of the axial resolution of the CFLS.

5.4 Discussion

In this chapter we have reported the design and construction of the CFLS for depth-resolved fluorescence lifetime spectroscopy. We have completed the optical design of the system, including the design of highly efficient single mode fiber coupling, theoretical optical simulation to achieve confocal axial resolution, and

spectral filtering to preferentially detect endogenous NADH and FAD in samples for cellular metabolism assessment. We have constructed the whole system and packaged it on a portable cart for future intravital experiments. The system includes several features to facilitate live animal imaging. These include a tilting stage that can be equipped with a heating pad and anesthesia equipment, and computer-controlled high-resolution linear actuators for precisely localized and automated axial scanning of the tissue. The system is equipped with highly sensitive photomultiplier tubes for rapid data acquisition, which is critical for overcoming motion artifacts introduced by the animal.

The CFLS only achieved an axial resolution of 78 μm , over six-fold greater than the theoretical calculation, which is less than 12 μm . This is likely due to misalignment of the focal point of the collecting lens L5 to the conjugate focal point of the objective lens L6. To achieve confocal optical sectioning, the illumination and detection focal volumes must exactly spatially coincide, and the resolution will be smallest when this coincident point is at the focal point of the objective lens. The method for aligning the multimode fiber (pinhole) to the collecting lens focal point has been to carefully translate the fiber until the detected signal from the sample is maximal. However, if the position of the sample is not at the true focal point of the objective lens, the pinhole is not in fact aligned with the conjugate focal point. The best way to find the true conjugate point will be to iteratively translate the sample at very small axial steps, align the multimode fiber, and collect the axial response at each increment. The axial step that produces the smallest FWHM of the response is the true focal point of the system, and the optical mounts should be locked at this position.

Another challenge in aligning the multimode fiber in this manner is the use of the reflective mirror to conduct the knife edge experiment instead of a fluorescent sample. Switching the configuration of the system from reflectance to the fluorescence mode affects the alignment of the optics, and therefore the resolution achieved in reflectance mode is likely lost. The fluorescent samples we have

attempted to test in the lab were either too thick (spin coated fluorescent tissue phantoms, fluorescent detection cards, evaporated fluorescent dyes), or too photo-unstable (papers, highlighters) to be used for this experiment. Fluorescent beads, which serve very well for confocal microscopy experiments, have been too difficult to locate with the CFLS, with the lack of imaging capability. The development of a fluorescent sample for conducting the knife edge experiment is the most important next step for the progress of this project.

After the optimization of the CFLS axial resolution is completed, the instrument should be tested on fluorescent tissue phantoms. These phantoms should consist of very sharp axial transitions between two spectrally distinct fluorophore layers. Most fluorescent tissue phantoms are separated by a thin plastic wrap (such as Saran® Wrap) to prevent diffusion of fluorophores across the interface. However, for high-resolution instruments such as the CFLS, the thickness of the wrap will affect the assessment. Furthermore, the fluorescence properties of the wrap itself are usually unknown.

The CFLS will be an excellent instrument for assessing cellular metabolism of tissue engineered constructs in living mice. Unlike the FLS presented in Chapter 4, the CFLS will be capable of extracting fluorescence signal from the thin epithelial cell layers while suppressing background fluorescence from the keratin and dermal layer. Furthermore, unlike the FLS, the CFLS is capable of detecting NADH and FAD fluorescence separately, enabling quantitative assessment of cell redox ratio [15]. Finally, unlike the Ti:Sapphire high-energy, ultra-fast pulse width lasers used for multiphoton microscopy, the CFLS uses a small, light-weight excitation source that can be easily transported into the clinic.

References

1. Georgakoudi, I., Rice, W.L., Hronik-Tupaj, M., and Kaplan, D.L. Optical spectroscopy and imaging for the noninvasive evaluation of engineered tissues. *Tissue engineering. Part B, Reviews* 14, 321, 2008.

2. Zhu, C., Liu, Q., and Ramanujam, N. Effect of fiber optic probe geometry on depth-resolved fluorescence measurements from epithelial tissues: a Monte Carlo simulation. *Journal of Biomedical Optics* 8, 237, 2003.
3. Utzinger, U., and Richards-Kortum, R.R. Fiber optic probes for biomedical optical spectroscopy. *Journal of Biomedical Optics* 8, 121, 2003.
4. Lloyd, W.R., Chen, L.-, and Mycek, M.-. Fluorescence Spectroscopy. In: Morgan, S.P., Rose, F.R.A.J. and Mather, S.J., eds. *Optical Techniques in Regenerative Medicine*. : CRC Press, 2014, pp. 171-203.
5. Wu, Y., Xi, P., Qu, J., Cheung, T.H., and Yu, M.Y. Depth-resolved fluorescence spectroscopy reveals layered structure of tissue. *Optics express* 12, 3218, 2004.
6. Richards-Kortum, R.R., Durkin, A., and Zeng, J. Description and Performance of a Fiber-Optic Confocal Fluorescence Spectrometer. *Applied Spectroscopy* 48, 350, 1994.
7. Bigelow, C.E., Conover, D.L., and Foster, T.H. Confocal fluorescence spectroscopy and anisotropy imaging system. *Optics Letters* 28, 695, 2003.
8. Wu, Y., and Qu, J.Y. Combined depth- and time-resolved autofluorescence spectroscopy of epithelial tissue. *Optics Letters* 31, 1833, 2006.
9. Wu, Y., and Qu, J.Y. Autofluorescence spectroscopy of epithelial tissues. *Journal of Biomedical Optics* 11, 054023, 2006.
10. Delaney, P.M., and Harris, M.R. Fiberoptics in Confocal Microscopy. In: Pawley, J., ed. : Springer US, 1995, pp. 515-523.
11. Dabbs, T., and Glass, M. Fiber-optic confocal microscope: FOCON. *Applied Optics* 31, 3030, 1992.
12. Wilson, T. Optical sectioning in confocal fluorescent microscopes. *Journal of microscopy* 154, 143, 1989.
13. Urayama, P., Zhong, W., Beamish, J.A., Minn, F.K., Sloboda, R.D., Dragnev, K.H., Dmitrovsky, E., Mycek, M.-A., A UV-Visible-NIR fluorescence lifetime imaging microscope for laser-based biological sensing with picosecond resolution. *Appl Phys B* 76, 483-496, 2003.
14. Pitts, J.D., Mycek, M.-A., Design and development of a rapid acquisition laser-based fluorometer with simultaneous spectral and temporal resolution. *Review of Scientific Instruments*, 72(7), 3061-3072, 2001.
15. Wilson, R.H., Chandra, M., Scheiman, J., Simeone, D., McKenna, B., Purdy, J., and Mycek, M.A. Optical spectroscopy detects histological hallmarks of pancreatic cancer. *Optics express* 17, 17502, 2009.

Chapter 6. Conclusions and Future Directions

6.1 Major contributions of this dissertation

The major contributions of this dissertation can be summarized as follows:

Chapter 2

- We developed and experimentally validated an optical model to predict the output light intensity when coupling a LED light source with a large divergence angle to a small diameter fiber-optic bundle.

- We used this model to improve system design parameters to maximize light throughput, allowing for use of smaller caliber optical bundles with more output power. We achieved a distal fiber output power of 1.7 mW through a fiber bundle of outer diameter 950 μm , the highest power throughput achieved using an LED-based microendoscopy system of this outer diameter, to our knowledge.

- We characterized the microendoscope performance using standard resolution targets and by comparison to bench-top epifluorescence microscopy of plated cells. Target-to-background ratio was consistent between the microendoscope and the epifluorescence microscope.

- We developed a microendoscope with outer diameter 680 μm and lateral resolution 4 μm that can enter the cannula of a 19G needle and pass harmlessly into the peritoneum of an anesthetized mouse for high resolution fluorescence microendoscopy of deep tissues. We demonstrated repetitive imaging for up to 4 weeks, a longer time span that ever previously demonstrated, to our knowledge.

Chapter 3

- We developed a microendoscope with outer diameter 680 μm and lateral resolution 4 μm that can pass through the instrument channel of a wide-field small animal endoscope. This methodology can be used to administer targeted imaging agents to the colon, provide insufflation to the colon for intravital imaging, localize colonic adenomas, and image the epithelial cells of the colonic mucosa in real time for “optical biopsy”.
- We demonstrated the ability for this microendoscope to acquire sub-cellular images in living mice, in real time, allowing for the study of molecular expression patterns of pre-malignant epithelial cells *in vivo*, using each animal as its own control.
- We validated *in vivo* images collected with the microendoscope with *ex vivo* images of freshly excised colonic mucosa tissues using a bench-top confocal microscope. The binding pattern of the target peptide to single epithelial cells was similar between *in vivo* microendoscopy and *ex vivo* confocal microscopy.
- We validated quantitative imaging of targeted molecular probe using the microendoscope. Target-to-background ratios measured by the microendoscope were consistent with those measured by wide-field fluorescence endoscopy.

Chapter 4

- We employed a hand-held fluorescence lifetime spectroscopy (FLS) probe and instrumentation for label-free, noninvasive, and real-time assessment of *ex vivo* tissue engineered constructs implanted in living mice, to assess integration with native tissue.
- We developed quantitative data analysis methods to assess the health of the implanted constructs *in vivo*.
- We correlated optical parameters measured *in vivo* 1 week after implantation to *in vitro* measures of cellular viability, measured prior to implantation. We found that

this correlation was not present at 3 weeks after implantation when most constructs had re-epithelialized. Histological analysis qualitatively confirmed the findings.

Chapter 5

- We engineered a depth-resolved fluorescence lifetime spectroscopy system for label-free, noninvasive, and real-time assessment of *ex vivo* tissue engineered constructs implanted in living mice. Confocal axial sectioning is intended to extract fluorescence preferentially from the thin epithelial cell layer and suppress background fluorescence from the dermal and keratin layers.
- We engineered a beam expander and constructed a focusing setup to couple the laser excitation source to a single mode fiber with 98% efficiency.
- We developed a mathematical simulation for the axial point spread function of the optical system as a function of numerical aperture, magnification, and multimode fiber core diameter to optimize system parameters and achieve good axial sectioning ability.
- We engineered dual-channel detection with band-pass filtering and highly-sensitive photomultiplier tubes to enable preferential high-speed acquisition of NADH and FAD. These endogenous fluorophores can report on cellular metabolism.
- We engineered automated axial scanning using motorized linear actuators and synchronized axial scanning with data acquisition. This enables fast data acquisition through the depth of the depth of the construct, from the keratin layer to the dermal layer.
- We adapted the system to be suitable for intravital assessments of living mice, including constructing the whole system on a portable cart, and configuring a tilting animal stage that can be equipped with a heating pad and anesthesia equipment.

6.2 Future Directions

6.2.1 *In Vivo Monitoring of Ovarian Cancer Cell Apoptosis Using a Dual-Color Flexible Fiber Microendoscope*

Having established the ability to conduct longitudinal studies in living mice with single cell resolution, the next step of this project is to use this instrument to assess tumor burden and response to therapy. Two advancements to the instrument would allow this capability:

- 1) Add dual-color imaging capability to the instrument. LEDs are now available in many colors. A green LED could be added to the system to excite red fluorescent protein (RFP), and a filter wheel that switches between long pass filters that pass green or red light. GFP and RFP can then be simultaneously imaged.
- 2) Engineer a genetic reporter that expresses RFP in the ovarian cancer cells when the cell is undergoing apoptosis. These cells will constitutively-express GFP, as before, and express RFP only while undergoing apoptosis.

After adding these two capabilities to the system, the methodology for longitudinal imaging can be carried out as in Chapter 2. During the course of the study, chemotherapeutics can be administered to the mice. Effectiveness of treatment can be monitored and quantified as the ratio of cells undergoing apoptosis (cells expressing RFP and GFP) to the cells not undergoing apoptosis (cells expressing only GFP). This study would enable the study of heterogeneity of response to therapy of individual cells in ovarian cancer, and could aid in the screening of novel chemotherapeutic agents.

6.2.2 *Confocal Fiber Bundle Based Microendoscopy*

The lack of optical sectioning ability is a major limitation of the HRME demonstrated in Chapters 2 and 3. Though the epithelial targets were on the surface of the colonic mucosa, assessment could greatly benefit from more clear, high-resolution imaging, allowing the visualization of the cellular morphology. Assessment of the molecular

targets in the crypts of the mucosa, which are not visible with the current instrumentation, could lead to earlier detection of cancer.

The instrument channel of the small animal does not allow passage of any fiber of larger caliber than the 680 μm fiber we demonstrated here. Confocal sectioning could be implemented using a small GRIN lens cemented at the distal tip of the bundle to increase magnification, increase the resolution of the instrument beyond the pixel-to-pixel core-spacing. The laser beam would require scanning across the proximal face of the fiber at high speed. This study would enable earlier and more accurate detection of colorectal cancer by “optical biopsy”.

6.2.3 Phantom for Simulating Epithelial Tissue Fluorescence

For both the fiber-optic FLS demonstrated in Chapter 4, and depth-resolved CFLS engineered in Chapter 5, there is a need for standardized phantoms—engineered devices that simulate properties of living tissues—for characterizing and validating the instruments. The optical instruments must be sufficiently sensitive and well-resolved to acquire signal from the thin, microscopic target cell layer that is sandwiched between a scattering and absorbing keratin layer and a strongly fluorescent dermal layer. For testing of optical instruments, there is a need for multi-layered optical phantoms that simulate scattering, absorption, and fluorescence properties of epithelial tissues. These can be used to quantitatively test the sensitivity and depth-resolution of optical instrumentation.

6.2.4 Characterization of Depth-Resolved Fluorescence Lifetime Spectrometer

As described in Chapter 5, the axial resolution of the depth-resolved fluorescence lifetime spectrometer is not yet optimized. Future work must solve this problem, following suggestions and ideas outlined in Section 5.4. After axial resolution is demonstrated near the theoretical calculation of $\sim 10\ \mu\text{m}$, the system should be fully characterized for fluorescence sensitivity, fluorescence lifetime resolution, and the ability to spectrally separate NADH and FAD fluorescence. Finally, the system should be used for *in vivo* assessments of EVPOME and other epithelial tissues.